

Acta Technologica Agriculturae 4
Nitra, Slovaca Universitas Agriculturae Nitriae, 2019, pp. 104–108

TOTAL SOLID CONTENT AND COMPOUND PROPERTIES FROM DIFFERENT COLLECTION TIME OF *HEVEA BRASILIENSIS* LATEX

JUNAIDI*, Andi WIJAYA, Arief RACHMAWAN, Mochlisin ANDRIYANTO

Sungei Putih Research Centre, Indonesian Rubber Research Institute, Medan, Indonesia

This study compared the total solid content and compound properties of *Hevea* rubber latex produced from material collected during different periods. Samples were collected from five trees, with the collection replicated three times with tapping task as replication. Observed parameters included total solid content, vulcanization characteristics, technical and physical properties. The results exhibited that the longer latex flowed, the more total solid content tended to decrease. Results indicate that compound of latex collected 20 minutes (C_{20}), 60 minutes (C_{60}), and 300 minutes (C_{300}) after tapping qualified for SIR 20. Other parameters did not show a significant difference among the three tested compounds. Considering the products requiring high dry rubber content, it is suggested not to blend the late collection with main collected latex.

Keywords: natural rubber; properties; tapping; vulcanization

Rubber tree (*Hevea brasiliensis* Muell Arg.) is the most economical species among latex production plants (Priyadarshan, 2011; Venkatachalam et al., 2013). Natural rubber is biosynthesized through the mevalonate (MVA) and 2-C-methyl-D-erythritol 4-phosphate (MEP) pathways in the laticifer tissues (Chow et al., 2012; Ramos et al., 2019). In addition to the rubber particles, latex contains proteins and phospholipids (Ramos et al., 2019). *Hevea* rubber is mainly cultivated in the tropical region of South and Southeast Asia, South America, and Africa. Indonesia is one of the largest natural rubber producers along with Thailand, India, China, Malaysia, and Vietnam.

Latex is harvested by slicing the bark and subsequent collecting of the dripping latex in a cup. Although *Hevea* can be tapped anytime, with the recommended time to tap before dawn when there is a high turgor pressure in cells (An et al., 2014). In such manner, latex will immediately flow with maximum velocity after tapping, which will gradually decrease, until it ceases to flow (Yeang, 2005; Bauer et al., 2014). The main latex collection is usually carried out before noon. However, after this main collection, some trees (not all) still release latex at lower flow rate, especially after ethylene stimulation (Shi et al., 2015; An et al., 2016). Some farmers blend this late latex collection with main latex collection, while others leave it in the cup allowing natural coagulation.

Rubber research has been dedicated to optimizing latex yield including rubber breeding and biotechnology (Da Costa et al., 2000; Tang et al., 2016), tapping method (Lacote et al., 2013; Sainoi et al., 2017), and stimulant application (Zhu and Zhang, 2009; Putranto et al., 2015; Dian et al., 2016). Nonetheless, the effect of environment and agronomical practices on rubber product properties is still not sufficiently comprehended. Moreno et al. (2005)

noticed that technical properties varied among rubber clones. Another study by Giraldo-Vásquez and Velásquez-Restrepo (2017) showed that seasonal variation influenced rubber technical properties. Janoško et al. (2013) suggested that the composition of rubber compound determined the final product quality.

This study compares the latex total solid content (TSC, %) and compound properties of latex samples collected at different collection periods. Since particular products require certain minimum values of the observed phenomena, study results could be contributive to latex collection management, as well as rubber processing for obtaining of quality products.

Material and methods

Sample collection

An observational study was carried out at Sungei Putih Research Centre, Indonesian Rubber Research Institute, Deli Serdang, Indonesia in September – November 2017 using 12 years old PB 260 rubber clone. Latex was collected from five trees, with the collection replicated three times with tapping task as replication. Tapping activity was executed at 08:00 AM (local time). Latex was collected at 20 minutes after tapping (L_{20}), 60 minutes after tapping (L_{60}), and 300 minutes after tapping (L_{300}). The total solid content was measured in accordance with the standard ASTM-D 1076-02 (ASTM International, 2002).

Compound establishment

Rubber compounds were processed using open mill and formula shown in Table 1. Mastication was performed in five

Contact address: Junaidi, Sungei Putih Research Centre, Indonesian Rubber Research Institute, P.O. Box 1415 Medan 20001, Indonesia, e-mail: junaidi.sp5@gmail.com

minutes and zinc oxide and stearic acid were added after that. Subsequently, n-cyclohexyl-2-benzothiazole sulphonamide (CBS) and sulphur were mixed into homogenous material, following a 30-minute milling process. Compounds were stored overnight at room temperature prior to the assessment. The C_{20} denotes compound from L_{20r} , while C_{60} was from L_{60} and C_{300} was from L_{300r} respectively.

Table 1 The formula for compound establishment

Material	Amount (phr)*
Rubber	100.0
Zinc oxide (ZnO)	6.0
Stearic acid	0.5
CBS	0.5
Sulphur	3.5

* phr – parts per hundred rubber

Compound assessment

The compound assessment was carried out at PT. Industri Karet Deli laboratory, Medan. Technical properties observed included Wallace initial plasticity (P_0 , %), plasticity retention index (PRI, %), and Mooney viscosity (V_R) (ML(1 + 4) 100 °C). Wallace initial plasticity is the average plastimeter reading for the unaged rubber. Plasticity retention index is a measure of the resistance of raw natural rubber to thermal oxidation; a high resistance is shown as a high index value. Mooney viscosity is the viscosity reached after the rotor rotates for a specific duration. Technical properties were assessed according to SNI 1903-2011 (The National Standardization Agency of Indonesia, 2011).

Compound maturation was measured using Moving Die Rheometer 2000 (Alpha Technologies, Washington – USA) at 180 °C with compound thickness 2 ± 0.2 mm. Vulcanization characteristics observed included maximum, minimum and delta torque modulus, scorch time, and optimum cure time. Physical properties assessed included hardness, tensile strength, elongation at break, modulus 200, and tear strength. The hardness indicates the compound resistance to permanent indentation. The tensile strength is the maximum stress that the sample can withstand while being stretched or pulled before breaking. The elongation at break is the extent to which a rubber material can be strained before it breaks. The modulus 200 expresses the stress needed to strain the sample for 200%. Tear strength shows the force necessary for ripping the sample and making the crack continue until it fails.

Statistical analysis

Statistical analysis was performed using R Statistic Software version 3.4.2 (R Development Core Team) in R Studio Interface version 1.1.383 (R Studio Inc.). Beta regression, a statistical analysis for percentage and proportion data (Mangiafico, 2016), was applied for observation of total solid content, Wallace initial plasticity (P_0), plasticity retention index (PRI), and elongation at break. Mooney viscosity, maximum torque modulus, minimum torque modulus, delta torque modulus, scorch time, optimum cure time, hardness, tensile strength, tear strength, and modulus 200

were analysed with one-way ANOVA. Estimated marginal means were compared on the basis of Tukey comparison method at $\alpha = 0.05$.

Results and discussion

Total solid content

Total solid content (TSC) indicates the percentage of solid particles contained in the latex. Our results showed that the total solid content tended to decrease with an increase in latex flowing time. The average TSC of L_{20} was $26.60 \pm 0.25\%$, while L_{60} and L_{300} were $25.40 \pm 0.14\%$ and $24.92 \pm 0.08\%$, respectively. At the beginning of tapping, the latex TSC was high due to a local increment of rubber particles near the tapping cut driven by accelerated rubber biosynthesis (An et al., 2016). Sainoi et al. (2017) suggested that low-frequency tapping did not affect the total solid content, since the gap between two tapping activities was sufficient for rubber regeneration. However, when tapping was combined with ethylene stimulation, a declining trend was noticed (Dian et al., 2016).

Specific products, such as centrifuged latex (Yup and Cacioli, 2002; Maspanger, 2007) and ribbed smoked sheet (RSS), require a certain minimum dry rubber content (DRC, %) of latex (Morshed et al., 2018). Due to this reason, latex collection management has to take into account the decrease in latex DRC for meeting the factories' processing requirements. Furthermore, anticoagulant needs to be applied wisely, since it affects latex quality as reported by Santipanusopon and Riyajan (2009). For products requiring high DRC, it is recommended not to blend late latex collection with main latex collection. Late latex collection may be stored and processed separately for crumb rubber production, which does not require such high DRC.

Technical properties

Wallace initial plasticity (P_0) shows compound's compression ability, while plasticity retention index (PRI) indicates compound oxidation resistance, and Mooney viscosity (V_R) denotes the length of rubber molecules (Zheleva, 2013). The results showed that the latex flowing time significantly affected only the PRI; the P_0 and V_R did not differ significantly in individual treatments. The PRI, along with latex flowing time, indicated an increase; the PRI value of C_{300} was higher than value of C_{20r} , yet it was not significantly different from C_{60r} . The PRI values of C_{20r} , C_{60r} , and C_{300} were $27.00 \pm 1.73\%$, $27.00 \pm 10.54\%$, and $41.67 \pm 12.66\%$, respectively (Table 2). The high PRI value suggested that the compound was resistant to high temperatures. Our results were partially in line with Vachlepi and Purbaya (2018), who reported that low rubber content in latex, similar condition to C_{300r} , did not affect P_0 and PRI values.

Compound quality including PRI was influenced by the type of anticoagulant (Handayani, 2014) and maturation condition (Intapun et al., 2009). Indonesian National Standard (SNI) set a minimum P_0 of 30% and PRI of 40% for SIR 20 (SIR – Standard Indonesian Rubber), the common type of crumb rubber produced in Indonesia with regard to the ISO standard, whilst V_R value is not specified for SIR 20, but it is required for SIR 20 CV, a variant of SIR 20 (The National

Table 2 Technical properties of the compounds from different latex collection

Compound	Wallace initial plasticity (P_0) (%)	Plasticity retention index (PRI) (%)	Mooney viscosity (V_R) (ML (1 + 4) 100 °C)
C ₂₀	52.33 ±12.50 a	27.00 ±1.73 a	91.70 ±1.15 a
C ₆₀	54.00 ±7.94 a	27.00 ±10.54 ab	93.00 ±2.95 a
C ₃₀₀	51.33 ±6.39 a	41.67 ±12.66 b	90.20 ±3.80 a
	$p = 0.9396$	$p = 0.0289$	$p = 0.5232$

Different letters in the same column indicate significant difference based on Tukey's comparison ($\alpha = 0.05$); \pm indicate standard deviation

C₂₀ – Compound from latex collected 20 minutes after tapping; C₆₀ – Compound from latex collected 60 minutes after tapping; C₃₀₀ – Compound from latex collected 300 minutes after tapping (late collection)

Table 3 Physical characteristics of the vulcanizes

Compounds	Maximum torque modulus S_{max} (N·mm ⁻²)	Minimum torque modulus S_{min} (N·mm ⁻²)	Delta $S_{max} - S_{min}$ (N·mm ⁻²)	Scorch time t_{s2} (minutes)	Optimum cure time t_{90} (minutes)
C ₂₀	6.42	0.92	5.50	0.52	1.35
C ₆₀	7.09	0.82	6.27	0.48	1.37
C ₃₀₀	6.39	0.74	5.65	0.51	1.40

Table 4 Technical properties of the compounds from different latex collection

Compound	Hardness (Shore A)	Tensile strength (N·mm ⁻²)	Tear strength (N·mm ⁻²)	Modulus 200 (N·mm ⁻²)	Elongation at break (%)
C ₂₀	43.00 ±3.00 a	8.49 ±7.67 a	33.34 ±2.66 a	1.35 ±0.29 a	495.00 ±226.43 a
C ₆₀	42.00 ±2.00 ab	14.45 ±7.88 a	36.71 ±6.68 a	1.27 ±0.15 a	574.17 ±212.23 a
C ₃₀₀	35.67 ±3.21 b	11.95 ±4.14 a	30.07 ±3.47 a	1.04 ±0.06 a	658.33 ±73.16 a
	$p = 0.036$	$p = 0.649$	$p = 0.285$	$p = 0.205$	$p = 0.583$

Different letters in the same column indicate significant difference based on Tukey's comparison ($\alpha = 0.05$); + indicate standard deviation

Standardization Agency of Indonesia, 2011). Observed results showed that C₃₀₀ qualifies for SIR 20; nonetheless, the PRI values of C₂₀ and C₆₀ do not qualify for it.

Vulcanization characteristics

Vulcanization characteristic testing describes the compound vulcanization extent (Cifriadi and Falaah, 2013). Our assessment indicated that three compounds (C₂₀, C₆₀, and C₃₀₀) had relatively similar vulcanization characteristics (Table 3). Torque modulus describes the crosslink density formed during vulcanization, the lower value of $S_{max} - S_{min}$ indicates fewer crosslinks between rubber particles with vulcanizing material (Ramadhan and Fathurrohman, 2013). Scorch time (t_{s2}) of C₂₀, C₆₀, and C₃₀₀ in this study showed a relatively same value, i.e. 0.52, 0.48, and 0.51 minutes, respectively. The optimum cure time (t_{90} , minutes) of C₃₀₀ was slightly higher (1.40 minutes) than that of C₂₀ (1.35 minutes) and C₆₀ (1.37 minutes). Vulcanization time is an important parameter related to time and energy efficiency especially in large scale production (Vachlepi and Suwardin, 2015). Research by Utomo et al. (2010) showed that the energy cost of low-grade rubber production was higher than that of the high grade one.

Physical properties

The hardness determines the appearance and durability of rubber products (Syabani et al., 2018). Result showed that the hardness of C₃₀₀ (35.76 Shore A) was lower than that of

C₂₀ (43.00 Shore A) and C₆₀ (42.00 Shore A) (Table 4). However, all samples tested in this study exhibited a normal value for natural rubber around 40 shore A. The average tensile strength of C₂₀ was 8.49 N·mm⁻², C₆₀ 14.45 N·mm⁻², and C₃₀₀ 14.45 N·mm⁻², while tear strength of each compound was 33.34 N·mm⁻², 36.71 N·mm⁻², and 30.07 N·mm⁻², respectively. Elongation at break values tended to increase with collection time; vice versa, modulus 200 tended to decrease. The average of elongation at break of C₂₀, C₆₀, and C₃₀₀ was 495.00%, 574.17%, and 658.33%, respectively, while the modulus 200 was 1.35%, 1.27%, and 1.04%, respectively.

All physical parameters did not show any significant difference between samples except the hardness. Results indicate that collection time did not affect compounds' physical properties. This study used latex from the same trees and exploited identical preparation procedures; therefore, it is suggested that all samples have a similar rubber structure. Multiple conducted studies (Hidayoko and Wulandra, 2014; Purbaya and Suwardin, 2017) suggest that the coagulating process and reinforcement materials (Al-Nesrawy et al., 2014) play determinative role in final compound properties.

Conclusion

The total solid content of latex tended to decline along with the collection time period. Therefore, for products requiring high dry rubber content, it is recommended to separate late latex collection from the main latex collection. Latex

collection period did not affect the technical and physical compound properties. It is suggested that not the collection time, but rather other factors, such as coagulating process and reinforcement material, determine the compound quality.

Acknowledgment

The authors would like to thank PT. Industri Karet Deli, Medan for laboratory equipment supports and technical assistance during this study.

References

- AL-NESRAWY, S. H. – AL-MAAMORI, M. – HASSANI, A. S. – JAAFAR, H. I. 2014. Effect of mixture of reclaimed tire and carbon black percent on the mechanical properties of SBR/NR blends. In *International Journal of Advanced Research*, vol. 2, no. 1, pp. 234–243.
- AN, F. – CAHILL, D. – ROOKES, J. – LIN, W. – KONG, L. 2014. Real-time measurement of phloem turgor pressure in *Hevea brasiliensis* with a modified cell pressure probe. In *Botanical Studies*, vol. 55, no. 1, pp. 1–11.
- AN, F. – ROOKES, J. – XIE, G. – CAHILL, D. – CAI, X. – ZOU, Z. – KONG, L. 2016. Ethephon increases rubber tree latex yield by regulating aquaporins and alleviating the tapping-induced local increase in latex total solid content. In *Journal of Plant Growth Regulation*, vol. 35, no. 3, pp. 701–709.
- ASTM International. 2000. Standard Specification for Rubber – Concentrated, Ammonia Preserved, Creamed, and Centrifuged Natural Latex, D1076–02 ed., vol. 09. Pennsylvania: ASTM International.
- BAUER, G. – FRIEDRICH, C. – GILLIG, C. – VOLLRATH, F. – SPECK, T. – HOLLAND, C. 2014. Investigating the rheological properties of native plant latex. In *Journal of the Royal Society Interface*, vol. 11, article no. 20130847.
- CHOW, K. S. – MAT-ISA, M. N. – BAHARI, A. – GHAZALI, A. K. – ALIAS, H. – MOHD-ZAINUDDIN, Z. – HOH, C. C. – WAN, K. L. 2012. Metabolic routes affecting rubber biosynthesis in *Hevea brasiliensis* latex. In *Journal of Experimental Botany*, vol. 63, no. 5, pp. 1863–1871.
- CIFRIADI, A. – FALAAH, A. F. 2013. Kinetics study of sulfur vulcanization on unfilled natural rubber compound. In *Jurnal Penelitian Karet*, vol. 31, no. 2, pp. 159–167. (In Indonesian: Studi kinetika vulkanisasi belerang pada kompon karet alam tanpa bahan pengisi).
- DA COSTA, R. B. – DE RESENDE, M. D. V. – DE ARAUJO, A. J. – GONÇALVES, P. DE S. – SILVA, M. DE A. 2000. Maximization of genetic gain in rubber tree (*Hevea*) breeding with effective size restriction. In *Genetics and Molecular Biology*, vol. 23, no. 2, pp. 457–462.
- DIAN, K. – OKOMA, M. K. – GNAGNE, M. Y. – GABLA, R. O. – OBOUYEBA, S. 2016. Impact of intensive stimulation with Ethephon in downward tapping on the potential of production in upward tapping in GT 1 clone of *Hevea brasiliensis*. In *International Journal of Current Science*, vol. 19, no. 3, pp. E 11–23.
- GIRALDO-VÁSQUEZ, D. H. – VELÁSQUEZ-RESTREPO, S. M. 2017. Variation of technological properties of field natural rubber lattices from *Hevea brasiliensis* clones and natural rubber-based compounds. In *Revista DYNA*, vol. 84, no. 203, pp. 80–87.
- HANDAYANI, H. 2014. Effect of various type of solid coagulants on the quality of coagulum and vulcanized natural rubber. In *Jurnal Penelitian Karet*, vol. 32, no. 1, pp. 74–80. (In Indonesian: Pengaruh berbagai jenis penggumpal padat terhadap mutu koagulum dan vulkanisat karet alam).
- HIDAYOKO, G. – WULANDRA, O. 2014. Effect of the latex coagulant used to quality of SIR 20. In *Agritepa*, vol. 1, no. 1, pp. 119–130. (In Indonesian: Pengaruh penggunaan jenis bahan penggumpal lateks terhadap mutu SIR 20).
- INTAPUN, J. – SAINTE-BEUVE, J. – BONFILS, F. – TANRATTANAKUL, V. – DUBREUCQ, E. – VAYSSE, L. 2009. Characterisation of natural rubber cup coagula maturation conditions and consequences on dry rubber properties. In *Journal of Rubber Research*, vol. 12, no. 4, pp. 171–184.
- JANOŠKO, I. – POLONEC, T. – CHRASTINA, J. 2013. Comparison of summer and winter tyres on a dry and snowy surface. In *Acta Technologica Agriculturae*, vol. 16, no. 1, pp. 5–9.
- LACOTE, R. – DOUMBIA, A. – OBOUYEBA, S. – GOHET, E. 2013. Tapping panel diagnosis, decision support tool for more sustainable rubber tapping system. In *IRRDB–MRPPA International Workshop on the Development of Smallholder Rubber Industry in Myanmar*. <https://doi.org/10.13140/RG.2.1.3148.7527>.
- MANGIAFICO, S. S. 2016. R Handbook: Beta Regression for Percent and Proportion Data. Retrieved June 26, 2019 from http://rcompanion.org/handbook/J_02.html
- MASPANGER, D. R. 2007. Preparation of creamed latex by low speed centrifugation process and the quality of its rubber product. In *Agritech*, vol. 27, no. 3, pp. 124–129. (In Indonesian: Pembuatan lateks dadih dengan proses sentrifugasi putaran rendah dan kualitas barang jadi karetnya).
- MORENO, R. M. B. – MARISELMA, F. – GONÇALVES, P. D. S. – MATTOSO, L. H. C. 2005. Technical properties of latex and natural rubber of *Hevea brasiliensis* clones. In *Scientia Agricola*, vol. 62, no. 2, pp. 122–126.
- MORSHED, A. J. M. – HELALI, O. H. M. – MOSTAFA, M. – BAKAR, M. A. – DAS, S. K. 2018. A review-production of ribbed smoked sheet in Chattogram Hill Tracts of Bangladesh and assessment of heavy metals in itself. In *Journal of Applied Chemistry*, vol. 11, no. 1, pp. 10–14.
- PRIYADARSHAN, P. M. 2011. *Biology of Hevea Rubber*. Oxfordshire: CAB International, 234 pp. ISBN 9781845936662.
- PURBAYA, M. – SUWARDIN, D. 2017. Qualitative analysis of coagulant type in the raw rubber material. In *Jurnal Penelitian Karet*, vol. 35, no. 1, pp. 103–114. (In Indonesian: Pengujian kualitatif terhadap jenis koagulan dalam bahan olah karet).
- PUTRANTO, R. – HERLINAWATI, E. – RIO, M. – LECLERCQ, J. – PIYATRAKUL, P. – GOHET, E. – SANIER, C. – OKTAVIA, F. – PIRRELLO, J. – KUSWANHADI-MONTORO, P. 2015. Involvement of ethylene in the latex metabolism and tapping panel dryness of *Hevea brasiliensis*. In *International Journal of Molecular Sciences*, vol. 16, pp. 17885–17908.
- RAMADHAN, A. – FATHURROHMAN, M. I. 2013. The effect of stearic acid on curing characteristic, mechanical properties and swelling of organoclay filled natural rubber vulcanizates. In *Jurnal Sains Materi Indonesia*, vol. 14, no. 2, pp. 108–113. (In Indonesian: Pengaruh asam stearat terhadap karakteristik pematangan, sifat mekanik dan swelling vulkanisat karet alam dengan bahan pengisi organoclay).
- RAMOS, M. V. – DEMARCO, D. – DA COSTA SOUZA, I. C. – DE FREITAS, C. D. T. 2019. Laticifers, latex, and their role in plant defense. In *Trends in Plant Science*, vol. 24, no. 6, pp. 553–567.
- SAINOI, T. – SDOODEE, S. – LACOTE, R. – GOHET, E. 2017. Low frequency tapping systems applied to young-tapped trees of *Hevea brasiliensis* (Willd. ex A. Juss.) Müll. Arg. in Southern Thailand. In *Agriculture and Natural Resources*, vol. 51, no. 4, pp. 268–272.
- SANTIPANUSOPON, S. – RIYAJAN, S. A. 2009. Effect of field natural rubber latex with different ammonia contents and storage period on physical properties of latex concentrate, stability of skim latex and dipped film. In *Physics Procedia*, vol. 2, pp. 127–134.
- SHI, M. J. – CAI, F. G. – TIAN, W. M. 2015. Ethrel-stimulated prolongation of latex flow in the rubber tree (*Hevea brasiliensis*

- Muell. Arg.): an Hev b 7-like protein acts as a universal antagonist of rubber particle aggregating factors from luteoids and C-serum. In *Journal of Biochemistry*, vol. 159, no. 2, pp. 209–216.
- SYABANI, M. W. – FAUZIYAH, F. I. – MUTIARA, T. 2018. Effect of the addition of rubber reclaim from side product of outsole on fisis and thermal properties boot outsole product (study case at CV. Carita Niaga)). In *Jurnal Sains Dan Teknologi Lingkungan*, vol. 10, no. 1, pp. 26–40. (In Indonesian: Pengaruh penambahan karet reclaim dari limbah outsole terhadap sifat fisis dan sifat thermal produk outsole sepatu (studi kasus di CV. Carita Niaga).
- TANG, C. – YANG, M. – FANG, Y. – LUO, Y. – GAO, S. – XIAO, X. – AN, Z. – ZHOU, B. – ZHANG, B. – TAN, X. – YEANG, H. – QIN, Y. – YANG, J. – LIN, Q. – MEI, H. – MONTORO, P. – LONG, X. – QI, J. – HUA, Y. – HE, Z. – SUN, M. – LI, W. – ZENG, X. – CHENG, H. – LIU, Y. – YANG, J. – TIAN, W. – ZHUANG, N. – ZENG, R. – LI, D. – HE, P. – LI, Z. – ZOU, Z. – LI, S. – LI, C. – WANG, J. – WEI, D. – LAI, C. – LUO, W. – YU, J. – HU, S. – HUANG, H. 2016. The rubber tree genome reveals new insights into rubber production and species adaptation. In *Nature Plants*, vol. 2, pp. 1–10.
- The National Standardization Agency of Indonesia. 2011. SNI 1903–2011: Rubber Technical Specification. Jakarta: The National Standardization Agency of Indonesia. 13 pp.
- UTOMO, T. P. – HASANUDIN, U. – SUROSO, E. 2010. Comparative study of low and high-grade crumb rubber processing energy. In *Proceeding of The World Congress on Engineering 2010*. London, vol. 3, pp. 2449–2453. ISBN 9789881821089.
- VACHLEPI, A. – PURBAYA, M. 2018. Effect of latex dilution on characteristics and technical qualities of natural rubber. In *Prosiding Seminar Nasional Hasil Litbangyasa Industri 2018*, pp. 106–117. AGUSTINI, S. – SUSANTO, T. (Eds.). Palembang: Balai Riset dan Standardisasi Industri Palembang. (In Indonesian: Pengaruh pengenceran lateks terhadap karakteristik dan mutu teknis karet alam).
- VACHLEPI, A. – SUWARDIN, D. 2015. Study of the natural rubber compound making from coal briquette ash and palm shell charcoal fillers. In *Jurnal Dinamika Penelitian Industri*, vol. 26, no. 1, pp. 1–19. (In Indonesian: Kajian pembuatan kompon karet alam dari bahan pengisi abu briket batubara dan arang cangkang sawit).
- VENKATACHALAM, P. – GEETHA, N. – SANGEETHA, P. – THULASEEDHARAN, A. 2013. Natural rubber producing plants: an overview. In *African Journal of Biotechnology*, vol. 12, no. 12, pp. 1297–1310.
- YEANG, H. 2005. The kinetics of latex flow from the rubber tree in relation to latex vessel plugging and turgor pressure. In *Journal of Rubber Research*, vol. 8, no. 3, pp. 160–181.
- YUP, E. – CACIOLI. 2002. The manufacture of gloves from natural rubber latex. In *Journal of Allergy and Clinical Immunology*, vol. 110, no. 2, pp. S3–S14.
- ZHELEVA, D. 2013. An attempt for correlation between Mooney viscosity and rheological properties of filled rubber compounds. In *Journal of Chemical Technology and Metallurgy*, vol. 48, no. 3, pp. 241–246.
- ZHU, J. – ZHANG, Z. 2009. Ethylene stimulation of latex production in *Hevea brasiliensis*. In *Plant Signaling and Behavior*, vol. 4, no. 11, pp. 1072–1074.



Acta Technologica Agriculturae 4
Nitra, Slovaca Universitas Agriculturae Nitriae, 2019, pp. 109–114

APPLICATION AND EVALUATION OF PERFORMANCE QUALITY OF HOSE-REEL IRRIGATION MACHINE

Ján JOBBÁGY*, Norbert MICHLIAN, Peter DAČANIN, Ivan RIGÓ

Slovak University of Agriculture in Nitra, Slovak Republic

Considering the global tendency in water saving, this research is focused on practical measurements of even distribution of water. The performance quality is determined by values of coefficients of distribution uniformity and non-uniformity given in percentages. Objects of investigation were belt irrigators with varying input conditions (seven pieces). Testing of hose-reel irrigators took place in Southern and Western Slovakia. Tests were carried out during irrigation of selected agricultural crops (potatoes, vegetables); in these areas, rainwater vessels were distributed at a spacing of 1 or 2 m, perpendicular to the direction of movement of the bracket or tripod with a gun sprinkler. The input conditions, such as machine specifications and weather conditions, were monitored and evaluated for all variants. The data were also analysed along with the linear model through statistical analysis software – one-way analysis of variance ANOVA. Considering the results, it is possible to conclude that there were recorded statistically significant differences for uniformity coefficients, depending not only on the site but also on the specific evaluation methodology ($P > 0.05$). If the input conditions (site, type of irrigator, sprinkler) were changed, the effect of dependence was demonstrated to a much greater extent ($P < 0.05$, $F = 7.08 > F_{crit}$). The results of the non-uniformity coefficients confirmed the statistically significant differences not only in the sample sets of coefficients but also in the selection sets of conditions.

Keywords: performance quality; irrigation uniformity; ANOVA; hose-reel irrigation machine; level of non-uniformity; variation coefficient

Agricultural crops can only be grown in areas with suitable climatic conditions, both in terms of temperature and water. Unsatisfactory climatic conditions result in low harvest and in cases of particularly poor climatic conditions, crops can be completely destroyed. The need for irrigation in individual areas and regions of the Slovak Republic is determined primarily by the deficit of water precipitation and the annual distribution of rainfall, but also by other climatic factors, e.g. air temperature and saturation supplement (Hennyeyová and Palková, 2006; Jobbágy et al., 2008). In order to achieve the most even and sufficient harvest of irrigated crops, the performance quality of irrigators needs to be at a high level. This can only be achieved by regular maintenance and inspection of nozzles and sprayers (Jobbágy, 2011; Dechmi et al., 2003a). On the other hand, irrigation uniformity guarantees appropriate moisture conditions for the crop (Látečka, 2000). Several indicators are used to assess the performance quality, ranging from visual inspection to evaluation through methodologies and standards (Jobbágy et al., 2013; Topak et al., 2005). In case of application of any of the methodologies utilized in this paper, irrigation dose was obtained from precipitation vessels (Topak et al., 2005; Jobbágy et al., 2013). According to Tomášik and Jobbágy (2013), Christiansen's spray uniformity coefficient below 84% of the set value indicates a low quality performance. Numerous authors suggest that wind velocity is one of the main influencing factors in terms of the quality of irrigation techniques (Dechmi

et al., 2003a). Solomon (1979) stated that the uniformity coefficient depends on the structure system variables (irrigator brand, nozzle size and type, nozzle pressure and spacing) and the major uncontrollable variable – wind speed (Temizel, 2016). The uniformity of application of the irrigation rate also affects the variability of soil moisture (Abbaspour-Gilandeh et al., 2018).

In addition to the uniformity of the moisture distribution, the resulting quality of the irrigation technique also affects the crop yield (Li and Rao, 2000; Dechmi et al., 2003b; Jobbágy et al., 2013). Standard of performance quality assessed by the spray uniformity coefficient should exceed 90%. Considering the performance quality assessment utilizing a non-uniformity coefficient, the value should be less than 10% (Jobbágy and Krištof, 2018; ASAE, 1998).

Generally, literature makes it clear that several methods of assessing the quality of irrigation machines are used in practice, e.g. uniformity coefficient, non-uniformity coefficient, degree of uniformity, and coefficient of variation (De Menezes et al., 2015). Results thus differ in values depending on the equation used to assess spray uniformity in the same studied areas. Sprinkler irrigation is becoming a preferred method if the available water for irrigation becomes scarce (Uddin et al., 2013).

The aim of the study is to compare selected coefficients of uniformity under several field conditions and to point out the possibilities of application of the studied types of result assessment on selected hose-reel irrigation machines.

Contact address: Ján Jobbágy, Slovak University of Agriculture in Nitra, Faculty of Engineering, Department of Machines and Production Biosystems, Tr. Andreja Hlinku 2, 949 76 Nitra, Slovak Republic, e-mail: jan.jobbagy@uniag.sk

Material and methods

Given the global climate change and water-saving issue, this paper evaluates the quality of irrigation techniques and compares different methods of evaluating the performance quality. In recent years in Slovakia, irrigation of agricultural crops has been representing one of the most important stages in the harvest production. The irrigation dose was applied over several irrigation seasons and years, with crops being predominantly potatoes and vegetables (carrots). Depending on the location of field experiments, there were various soil types – sandy loams and loamy sands. Fig. 1 shows the locations where experimental measurements were performed. The agricultural enterprise Agrocoop a.s. Imeľ is situated in the southwest of Slovakia in the district of Komárno (from F1 to F4 experimental fields). Terrain of agricultural enterprise is plane with the slope from 0 to 2°. The



Fig. 1 Locations under investigation in western region of Slovakia

first explored field is classified by BPEJ 04003 – the muck; medium soil depth; pH 7.78; strongly alkaline. The second agricultural enterprise was Paulis, Záhradkárske služby (F5 – experimental field). The main focus of the company

is purchase and sale of vegetables and fruits, as well as import of southern fruit and supply of retail outlets. The third agricultural enterprise was PD Kukučínov (F6 and F7 experimental fields) where irrigation technology is

Table 1 Irrigation machine technical data and selected parameters

Experimental field	Irrigation machine technical data						Weather conditions	
	type	L (m)	D _H (mm)	Type of sprinkler	K	M _d (mm)	v _w (m·s ⁻¹)	T (°C)
F1	BauerRainstar 85Tx	300	90	Gun Komet TWIN 140	70	15.19	0.5	29
F2	BauerRainstar 85Tx	300	90	Gun Komet TWIN 140	61	23.77	1	28
F3	BauerRainstar 85Tx	300	90	Gun Komet TWIN 140	30	24.18	1.5	30
F4	BauerRainstar 85Tx	300	90	Gun Komet TWIN 140	30	31.6	1.5	29
F5	Cipa 600 GX	300	110	boom	59	18.27	1	28
F6	Cipa 600GX	300	110	Gun Komet TWIN 140	34	25.79	1.2	25
F7	Cipa 600GX	300	110	Gun Komet TWIN 140	30	26.48	1.5	27

D_H – hose diameter; L – hose length; K – number of cups; M_d – irrigation rate; v_w – maximum wind speed; T – temperature, °C



Fig. 2 Example of irrigation uniformity test using rain gauge for measuring uniformity coefficient

used only if necessary. Average annual rainfall ranges from 500 to 550 mm.

Used irrigators

Fields were irrigated with hose-reel irrigation machines equipped with new or reconditioned distributors of irrigation water (Fig. 2). In the majority of cases, the source of water was groundwater or lake. The main irrigation system consisted of a stationary or mobile pump that was adapted to a tractor. The technical parameters of the input irrigators and the weather conditions for specific measurements are given in Table 1.

Performance quality

Performance quality assessment – the test of uniformity – was conducted by means of precipitation gauges to assess the spray uniformity. The rain gauge vessels had a diameter of 115 mm and total height of 100 mm. Vessels were placed on a tripod with a gun sprinkler or a bracket.

Irrigation assessment was performed in accordance with several methods proposed by Látečka (2000); Maroufpoor et al. (2010); Jobbágy (2011); Topak et al. (2005). Staebner (1931) started to evaluate the spray uniformity and based his assessments on the rule that the maximum spray intensity should not be more than twice the minimum, except for the marginal zone. On the basis of the measurement of precipitation heights in rain gauge vessels, he constructed isograms (lines with the same rainfall) and assessed the uniformity visually as very good, good, satisfactory, and bad.

Oehler (1932) assessed the uniformity of water distribution by the degree of non-uniformity U as a proportion of maximum and minimum intensity. In another work, Oehler (1933) used the value of average deviation A , which can be calculated as the average error of individual precipitation rate from their arithmetic mean. The value of non-uniformity is calculated as follows (for comparison with other results given in percentage):

$$a = \frac{A}{N_m} \cdot 100 \quad (\%) \quad (1)$$

where:

N_m – average value (mm)
 A – average deviation (mm)

To compare this value with uniformity coefficients, it is suggested to introduce the spray uniformity value a_r , calculated according to the following equation:

$$a_r = 100 \left(1 - \frac{A}{N_m} \right) \quad (\%) \quad (2)$$

For all tested irrigators, Oehler's method (1933) was used as the first.

The following assessments of the performance quality of hose-reel irrigators were carried out according to Heermann and Hein (in ASAE, 1998), Christiansen (in Zdražil and Spitz, 1966), Wilcox and Swailes (1947) and Voight (1962). Calculation of the uniformity coefficient of the CUH spray according to the method by Heermann and Hein is given by:

$$CUH = 100 \left[1 - \frac{\sum_{i=m}^n \{S_i |V_i - \bar{V}|\}}{\sum_{i=m}^n V_i \cdot S_i} \right] \quad (\%) \quad (3)$$

$$\bar{V} = \frac{\sum_{i=m}^n V_i \cdot S_i}{\sum_{i=m}^n S_i} \quad (\text{mm}) \quad (4)$$

where:

- n – number of rain gauge vessels
- i – number necessary to identify a specific rain gauge vessel beginning with $i = 1$ for the vessel closest to the pivot and ending with $i = n$ for a rain gauge vessel located furthest from the pivot
- V_i – irrigation dose in the i -th rain gauge vessel, mm
- S_i – distance of the i -th rain gauge vessel from the pivot (m)
- \bar{V} – average irrigation dose (mm)
- $|V_i - \bar{V}|$ – the absolute value of deviations from an average dose (mm)

The most widespread method for assessing the belt irrigators is spray uniformity evaluation by the uniformity coefficient CU according to Christiansen (in Zdražil and Spitz, 1966):

$$CU = 100 \left[1 - \frac{\sum_{i=1}^n |V_i - \bar{V}|}{n \cdot \bar{V}} \right] \quad (\%) \quad (5)$$

where:

- V_i – irrigation dose in the i -th rain gauge vessel (mm)
- \bar{V} – average irrigation dose (mm)
- n – number of rain gauge vessels, i.e. the number of elementary areas to which the surface is divided

Wilcox and Swailes (1947) suggested a uniformity coefficient C_{ws} as follows:

$$C_{ws} = 100 \left[1 - \frac{\sigma}{\bar{V}} \right] \quad (\%) \quad (6)$$

where:

- σ – standard deviation (mm)
- \bar{V} – average irrigation dose (mm)

In 1954, Stefanelli (in Lipták, 1971) suggested the usage of the variation coefficient C_v dependent on standard deviation σ and the average precipitation rate h_m (in accordance with our findings, the value is related to the spray uniformity coefficient value according to Wilcox and Swailes (1947); for the purposes of comparison, the value was converted to %):

$$C_v = \frac{\sigma}{h_m} \quad (\%) \quad (7)$$

Furthermore, evaluation of the performance quality by the coefficient of variation is also supported by the ASAE

standard (1998). In 1961, Hofmeister applied the degree of irregularity of E_f to evaluate the spray uniformity (the value is related to the uniformity coefficient value CU according to Christiansen, for the purposes of comparison, the value was converted to %):

$$E_f = \frac{\sum_{i=1}^n |h_i - \bar{h}|}{n \cdot \bar{h}} \cdot 100 \quad (\%) \quad (8)$$

where:

- E_f – degree of irregularity (%)
- average rainfall in the area being examined (mm)
- h_i – rate of rainfall at elementary surfaces (mm)
- n – number of elementary surfaces

Voight (1962) evaluates the spray uniformity by the degree of non-uniformity γ , taking into account the distance of the measured points from the sprayer r_i (for the purposes of comparison, the value was converted to %):

$$\gamma = \frac{\sum_{i=0}^n r_i |h_m - h_i|}{h_m \sum_{i=0}^n r_i} \cdot 100 \quad (\%) \quad (9)$$

where:

- γ – degree of non-uniformity (%)
- h_m – average rainfall in the area being examined (mm)
- h_i – rate of rainfall at elementary surfaces (mm)
- r_i – distance of the measured points from the sprayer (m)

Considering the possibility of result assessment by utilizing also the uniformity coefficient, it is possible to introduce the coefficient γ_r , which can be calculated as follows:

$$\gamma_r = 100 \left(1 - \frac{\sum_{i=0}^n r_i |h_m - h_i|}{h_m \sum_{i=0}^n r_i} \right) \quad (10)$$

- γ_r – degree of uniformity (%)

Evaluation of results

On the basis of the aforementioned, researchers exploit various methods to evaluate the quality of irrigation techniques, namely the spray uniformity coefficient, degree of non-uniformity and variation coefficient. This means that applied equations can lead to different results in terms of the uniformity of distributed water over the same elemental surfaces. The main aim of the paper is to evaluate the different coefficients proposed by individuals and to examine them in terms of the results acquired under field conditions. Finally, the results were evaluated by Duncan's test with a 95% confidence level. Thereby, single-factor analysis ANOVA (SAS, 2003) was used to evaluate and compare the results of different spray uniformity coefficients:

$$y_{ij} = \mu + C_i + e_{ij} \quad (\text{mm}) \quad (11)$$

where:

- y_{ij} – measured value
- μ – overall mean
- C_i – effect of uniformity coefficient
- e_{ij} – random error with mean 0 and variance σ^2

Results and discussion

Different coefficients determining the quality of the irrigation technique were used to assess the performance quality of hose-reel irrigators. Based on the established methodology, there were seven different input conditions, one of which included a combination of a sprinkler with a console. In other practical measurements, hose-reel irrigators with a tripod and a gun sprinkler were used. The most common evaluation of the irrigation performance quality of hose-reel irrigators is the one by Christiansen. In addition to this method, it was also decided to use four other spray uniformity coefficients CUH , C_{wsr} , a_r and γ_r .

Utilization of performance quality evaluation by the non-uniformity coefficient is not frequent. That is why it was decided to evaluate the results in such a manner as well. For this reason, the coefficient of uniformity a_r was introduced within the application of non-uniformity a (Eq. 1) so that the results obtained can be comparable. Graphical representation of the results of the irrigation uniformity coefficients for seven different input conditions is shown in Fig. 3. They show different results with respect to input values and methods of determination, except for a_r and CU ($P = 1$, $F = 0 < F_{crit}$), indicating no significant difference between the values. Changes in the uniformity spray coefficient CUH by Heermann and Hein are a result of another calculation method taking into account the distance between a particular vessel and sprayer. However, when evaluating the results gained by combining the a_r , CU and CUH coefficients through the ANOVA, there is already a significant difference between the individual assessment methods ($P < 0.05$, $F = 6.41 > F_{crit}$). When evaluating all the coefficients, it was also observed that there was a significant alteration between the different assessment methods ($P < 0.05$, $F = 4.23 > F_{crit}$).

Considering the evaluation of the results on the basis of assessing the existence of rate dependence from field conditions, it was observed that there was also a significant difference ($P < 0.05$, $F = 7.08 > F_{crit}$). Therefore, research results indicate that, when using a statistical model in which different spray uniformity coefficients or different field conditions were determined as sample sets, they are both dependent. It is possible to clearly state that the impact of changes in field conditions, e.g. changes in specific irrigators, shows a stronger dependence in contrast to the assessment method (applied coefficient).

Furthermore, the set irrigation rate had also a clear impact on the resulting performance quality in terms of evaluating the hose-reel irrigators. The greatest variability of the results was showed by CUH and C_{ws} values in comparison to other results and thus these are not recommended for performance quality assessment of hose-reel irrigators. On the other hand, since the results did not show any significant difference between the values ($P > 0.05$, $F = 1.13 < F_{crit}$),

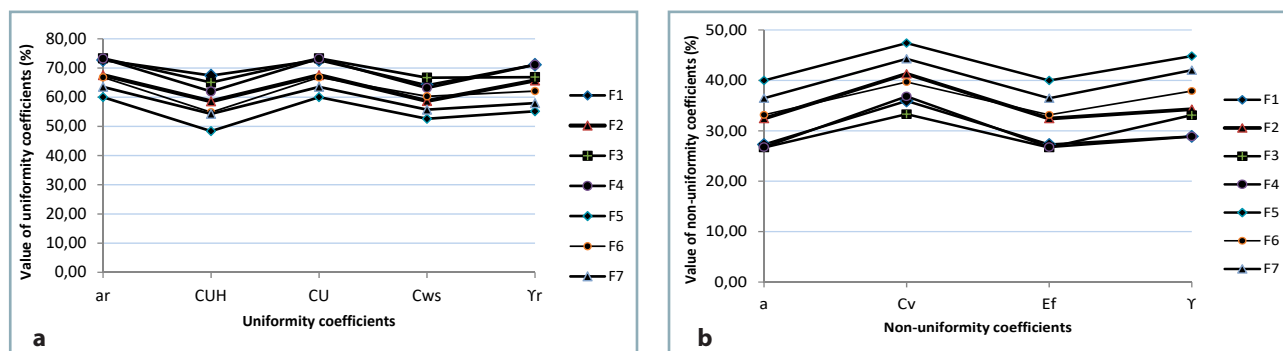


Fig. 3 Results of different uniformity (a) and non-uniformity (b) coefficients for all experimental fields
 a_r – uniformity coefficient according to Oehler; CUH – uniformity coefficient according to Heerman and Hein; CU – non-uniformity coefficient according to Christiansen; C_{ws} – unevenness coefficient according to Wilcox and Swailes; γ_r – Voight uniformity coefficient; a – non-uniformity coefficient according to Oehler; Cv – coefficient of variation; E_f – degree of non-uniformity according to Hofmeister; γ – Voight coefficient of non-uniformity

Voight coefficient γ_r together with CU and spray uniformity value a_r are highly recommendable for use. In one case, the spray uniformity value did not exceed 80%, while, according to the minimum standard set, neither machine meets the required performance quality.

However, it is possible to evaluate the performance quality by means of non-uniformity and thus it was decided to apply four possible ways of evaluation and following methods were selected as guidelines: the performance quality results according to Oehler (1933); the variation coefficient and the degree of non-uniformity according to Hofmeister (1961), and the non-uniformity coefficient according to Voight (1962).

Considering the assessment of both uniformity and non-uniformity, it was opted for utilization of the non-uniformity coefficients on one hand and field conditions combined with a particular hose-reel irrigator on the other hand. In both cases, the results showed a statistical dependence, in which the achieved P -value reached $P = 0.031$ ($P < 0.05$) with $F = 3.48$ ($F > F_{crit}$) for non-uniformity coefficients and the values reached the level of $P = 0.00035$ ($P < 0.05$) with $F = 6.97$ ($F > F_{crit}$) for different input conditions (different irrigators).

For various irrigation systems, several coefficients for examination of performance quality and irrigation dose distribution uniformity have been developed over the last few decades. In case presented, as well as in case of other researchers (e.g. province in Kurdistan), the results confirmed that it is not possible to use a single achieved result as a guide for a variety of conditions, since the results depend on field conditions (Maroufpoor et al., 2010; Jobbágy and Krištof, 2018; Berbe and Mateos, 2014). Traditionally, spray uniformity evaluation method according to Christiansen is the most frequently utilized (Li et al., 2015; Lovarelli et al., 2016) for assessment of performance quality of hose-reel irrigators. Due to the application of supplemental irrigation in fields with crops with higher need of irrigation, farmers must consider the irrigation rate, which also includes drainage losses. Application of irrigation dose often results in the highest performance quality (Castellanos et al., 2016). By applying a more efficient irrigation machine, a higher performance quality can be achieved; therefore, manufacturers using less efficient systems with a given

amount of water should implement more efficient systems with higher performance quality and lower overall water consumption (Jobbágy, 2011).

The performance quality was observed in the solid set sprinkler system, in which the operating pressures were changed. Output included not only performance quality in terms of spray uniformity evaluation but also barley yield. For each input setting, the coefficient of uniformity (CU), distribution uniformity (DU), and coefficient of variation (CV) parameters were determined. The results showed higher CU values in all cases, increased by higher operating pressure (El-Wahed et al., 2016). Numerous authors (González Perea et al., 2014; Tomášik and Jobbágy, 2013) have also developed programs for assessing the quality of irrigation techniques resulting in spray uniformity coefficients after providing input values. The additional irrigation dose represents a significant energy cost in case of unforeseen phenomena. However, a detailed analysis of water distribution and irrigation systems at fields is necessary before the introduction of measures.

Conclusion

In order to evaluate the performance quality of seven selected irrigation machines, it was decided to analyse the situations on the basis of the spray uniformity and non-uniformity coefficients. The results were evaluated utilizing ANOVA statistical apparatus with a significance value ($p = 0.05$). To evaluate the spray uniformity coefficients, it was concluded that there is a statistically significant difference between the individual calculation methods with a value of $F = 6.41$ ($F > F_{crit}$). The same result was shown in the evaluation of the results depending on field conditions $F = 7.08$ ($F > F_{crit}$). On the basis of comparison of the results obtained in terms of dependence on field conditions (for non-uniformity), it was observed that the results were statistically significant with $F = 6.97$ ($F > F_{crit}$). When estimating the results based on the evaluation of dependence on calculation methodology, it was found that they show a statistically significant dependence with $F = 3.48$ ($F > F_{crit}$). Finally, study results showed that coefficients should be selected with caution according to the proposed methodologies, recommendations and standards in order to assess the performance quality.

References

- ABBASPOUR-GILANDEH, Y. – HASANKHANI-GHAVAM, F. – SHAHGOLI, G. – RASOOLI SHARABIANI, V. – ABBASPOUR-GILANDEH, M. 2018. Investigation of the effect of soil moisture content, contact surface material and soil texture on soil friction and soil adhesion coefficients. In *Acta Technologica Agriculturae*, vol. 21, no. 2, pp. 44–50.
- EL-WAHED, M. A. – MEDICI, M. – LORENZINI, G. 2016. Sprinkler irrigation uniformity: Impact on the crop yield and water use efficiency. In *Journal of Engineering Thermophysics*, vol. 25, no. 1, pp. 117–125.
- ASAE S436.1. 1998. Test procedure for determining the uniformity of water distribution of center pivot and lateral move irrigation machines equipped with spray or sprinkler nozzles.
- BERBEL, J. – MATEOS, L. 2014. Does investment in irrigation technology necessarily generate rebound effects? A simulation analysis based on an agro-economic model. In *Agricultural Systems*, vol. 128, pp. 25–34.
- CASTELLANOS, M. T. – CARTAGENA, M. C. – REQUEJO, M. I. – ARCE, A. – CABELLO, M. J. – RIBAS, F. – TARQUIS, A. M. 2016. Agronomic concepts in water footprint assessment: A case of study in a fertirrigated melon crop under semiarid conditions. In *Agricultural Water Management*, vol. 170, no. C, pp. 81–90.
- DECHMI, F. – PLAYÁN, E. – FACI, J. M. – TEJERO, M. 2003a. Analysis of an irrigation district in northeastern Spain I. Characterisation and water use assessment. In *Agricultural Water Management*, vol. 61, no. 2, pp. 75–92.
- DECHMI, F. – PLAYÁN, E. – FACI, J. M. – TEJERO, M. – BERCERO, A. 2003b. Analysis of an irrigation district in northeastern Spain II. Irrigation evaluation, simulation and scheduling. In *Agricultural Water Management*, vol. 61, no. 2, pp. 93–109.
- DE MENEZES, P. L. – AZEVEDO, C. A. V. – EYNG, E. – NETO, J. D. – LIMA, V. L. A. 2015. Artificial neural network model for simulation of water distribution in sprinkle irrigation. In *Revista Brasileira de Engenharia Agrícola e Ambiental*, vol. 19, no. 9, pp. 817–822.
- GONZÁLEZ PEREA, R. – CAMACHO POYATO, E. – MONTESINOS, P. – RODRÍGUEZ DÍAZ, J. A. 2014. Critical points: Interactions between on-farm irrigation systems and water distribution network. In *Irrigation Science*, vol. 32, no. 4, pp. 255–265.
- HENNYEYOVÁ, K. – PALKOVÁ, Z. 2006. Use of Information Technologies and Simulation Models in Irrigation Economy. Nitra : SPU Nitra, 108 pp. ISBN 8080697159 (In Slovak: Využitie informačných technológií a simulačných modelov v závlahovom hospodárstve)
- HOFMEISTER, B. 1961. Nature and manifestation of transhumance. In *Erdkunde*, vol. 2, pp. 121–135. (In German: Wesen und Erscheinungsform der Transhumance).
- JOBBÁGY, J. 2011. Evaluation of Irrigation Machinery Regarding to Uniformity of Irrigation. Nitra : SPU Nitra, 123 pp. (In Slovak: Hodnotenie závlahovej techniky z hľadiska rovnomernosti závlahy postrekom)
- JOBBÁGY, J. – HOLBAY, A. – TOMÁŠIK, L. 2013. Design and testing of device for measuring the longitudinal uniformity of reel hose irrigation machine. In *Journal of Central European Agriculture*, vol. 14, no. 4, pp. 1334–1342.
- JOBBÁGY, J. – KRÍŠTOF, K. 2018. Evaluation of the coefficient of uniformity and non-uniformity of irrigation for wide-range irrigators in various field conditions. In *Research in Agricultural Engineering*, vol. 64, no. 2, pp. 55–62.
- JOBBÁGY, J. – SIMONÍK, J. – FINDURA, P. – ÁRVAY, J. 2008. Determination of soil moisture by two methods to create maps of soil moisture. In *Acta Technologica Agriculturae*, vol. 11, no. 4, pp. 93–97.
- LÁTEČKA, M. 2000. Uniformity of Irrigation in Irrigation Systems Using Rotary Irrigation Machinery. Nitra : SPU Nitra, 58 pp. (In Slovak: Rovnomernosť postreku pri závlaha otáčavými postrekovačmi).
- LI, Y. – BAI, B. – YAN, H. 2015. Development and validation of a modified model to simulate the sprinkler water distribution. In *Computers and Electronics in Agriculture*, vol. 111, pp. 38–47.
- LI, J. – RAO, M. 2000. Sprinkler water distributions as affected by winter wheat canopy. In *Irrigation Science*, vol. 20, no. 1, pp. 29–35.
- LIPTÁK, F. 1971. Evaluation of the spray distribution uniformity for irrigation machine. In *Hidrológiai Közlöny*, no. 8–9, pp. 385–393. (In Hungarian: Az esőszerű öntözés permeteloszlásának értékelése).
- LOVARELLI, D. – BACENETTI, J. – FIALA, M. 2016. Water footprint of crop productions: A review. In *Science of the Total Environment*, vol. 548–549, pp. 236–251.
- MAROUFPOOR, E. – FARYABI, A. – GHAMARNIA, H. – MOSHREFI, G. Y. 2010. Evaluation of uniformity coefficients for sprinkler irrigation systems under different field conditions in Kurdistan Province (northwest of Iran). In *Soil and Water Research*, vol. 5, no. 4, pp. 139–145.
- OEHLER, T. 1932. The water distribution in natural and artificial rain. In *BKTL-Schriften "Die Feldberegnung"*, Heft 30. (In German: Die Wasserverteilung bei natürlichen und künstlicher Regen)
- OEHLER, T. 1933. The uniformity of the water distribution through rotary jet sprinkler. The field irrigation. In *BKTL-Schriften*, Heft 38. (In German: Die Gleichmässigkeit der Wasserverteilung durch Drehstrahlregner. Die Feld. Beregnung)
- SOLOMON, K. 1979. Variability of sprinkler coefficient of uniformity test results. In *Transactions of the ASAE*, vol. 22, no. 5, pp. 1078–1086.
- STATISTICAL ANALYSIS SYSTEM (SAS). 2003. SAS User's Guide: Statistics. Version 8.02, SAS Institute, Inc., Cary.
- STAEBNER, F. E. 1931. Test of Spray Irrigation Equipment. Washington: United States Department of Agriculture, pp. 1–29.
- Temizel, K. E. 2016. Mapping of some soil properties due to precision irrigation in agriculture. In *Agronomy Research*, vol. 14, no. 3, pp. 959–966.
- TOMÁŠIK, L. – JOBBÁGY, J. 2013. Optimization of irrigation spray distribution in the term of its uniformity. In *AGRI on-line Papers in Economics and Informatics*, vol. 5, no. 2, pp. 103–109.
- TOPAK, R. – SUHERI, S. – CIFTCI, N. – ACAR, B. 2005. Performance evaluation of sprinkler irrigation in a semi-arid area. In *Pakistan Journal of Biological Sciences*, vol. 8, pp. 97–103.
- UDDIN, J. – HANCOCK, N. H. – SMITH, R. J. – FOLEY, J. P. 2013. Measurement of evapotranspiration during sprinkler irrigation using a precision energy budget (Bowen ratio, eddy covariance) methodology. In *Agricultural Water Management*, vol. 116, pp. 89–100.
- VOIGHT, D. 1962. The assessment of water distribution in rotary irrigator. In *Deutsche Agrartechnik*, vol. 12, pp. 264–266. (In German: Die Beurteilung der Wasserverteilung bei Drehstrahlregnern).
- WILCOX, J. C. – SWAILES, G. E. 1947. Uniformity of water distribution by some under tree orchard sprinkler. In *Journal of Scientific Agriculture*, vol. 27, pp. 565–583.
- ZDRAŽIL, K. – SPITZ, P. 1966. Determination of optimum rainfall curves in rotary sprayers. In *Vodné Hospodárstvo*, no. 5, pp. 203–204. (In Czech: Stanovení optimálních dešťomerných křivek u otočných postřikovačů).



Acta Technologica Agriculturae 4
Nitra, Slovaca Universitas Agriculturae Nitriae, 2019, pp. 115–121

THE EFFECT OF TRACTOR DRIVING SYSTEM TYPE ON ITS SLIP AND ROLLING RESISTANCE AND ITS MODELLING USING ANFIS

Abdolmajid MOINAR, Gholamhossein SHAHGHOLI*

University of Mohaghegh Ardabili, Iran

Pulling force required for operations such as tillage is a result of the interaction between the tractor's wheel drive and soil surface limited by various factors, such as the rolling resistance and slip of the wheel drive. In this research, the traction performance of tractors with different driving systems (four-wheel drive, rear wheel drive, and front wheel drive) was investigated. Test parameters included different tractor forward speeds (1.26, 3.96, and 6.78 km·h⁻¹), tire inflation pressures (170, 200, and 230 kPa), ballast weights (0, 150, and 300 kg), and aforementioned driving systems, as well as required drafts (2, 6, and 10 kN). For each experiment, two indices of slip and rolling resistance were measured. The results of this study showed that the four-wheel-driving system indicated a low slip at similar pulling forces. In order to achieve a low slip, the four-wheel driving system did not necessarily need to add the ballast weight or to reduce the inflation pressure. The four-wheel driving system showed lower rolling resistance than the other two systems. Slip and rolling resistance of wheels were predicted using an adaptive neuro-fuzzy inference system (ANFIS). It was found that ANFIS had a high potential for predicting the slip ($R^2 = 0.997$) and rolling resistance ($R^2 = 0.9893$).

Keywords: motion system; ballast weight; tractor performance; inflation pressure

The optimum criterion for evaluating the tractor performance is calculation of the tractor traction performance during ploughing operations on soft soils (Battiato and Diserens, 2017). The pulling force required for operations such as tillage is a result of the interaction between the tractor's wheel drive and soil surface, which converts the power generated by the engine to the pulling force. Majority of studies have shown that 20 to 55% of tractor power is lost in the process of interaction between tire and soil surface due to the drive wheel slip, tractor's rolling resistance, and tire and soil deformation (Damanauskas and Janulevicius, 2015). The tractive performance is affected by the tractor design parameters, attaching tools, and soil conditions (Moinar and Shahgholi, 2018).

If the wheel drive slip exceeds 15%, it will result in severe soil compaction and reduced performance (Moitzi et al., 2013). Slipping less than 7% during agricultural operations can be achieved by deployment of very heavy tractors. However, in this case, carrying excessive weights leads to increased fuel consumption and soil compaction, which are considered undesirable (Janulevicius et al., 2018).

Main factors affecting the rolling resistance of a pneumatic tire in deformable soils are soil displacement, tire flexibility, and soil friction and adhesion; several other subfactors are wheel diameter, inflation pressure, and axle load. Research shows that the wheel diameter has an indirect relationship, the axle load has a direct relationship, and the inflation pressure has an inverse relationship with the rolling resistance (Elwaleed et al., 2006). When the soil is hard, its cohesion is high, leading to less slipping and lower

rolling resistance (Moitzi et al., 2013), while in plastic state, soil cohesion decreases and adhesion to tire increases. This causes higher tire sinking, making the wheels slip, and high rolling resistance, resulting in greater loss of power and reduced tractor efficiency (Battiato et al., 2013).

Considering the tillage operation, it has been reported that, depending on the amount of ballast weight and its location, the draft can be increased up to 15% (Muhsin, 2010). However, this method has an adverse effect on soil and causes soil compaction in a depth that is usually deeper than that of conventional tillage operations (Barbosa and Magalhaes, 2015). The excess ballast weight also increases fuel consumption due to increased rolling resistance and higher tire sinkage in the soil. On the other hand, when the ballast weight is lower than optimal value, tractor will waste fuel due to excessive slipping (Lacour et al., 2014). Another way to reduce the slip is to increase the contact surface between the drive wheel and soil surface. By reducing the tire pressure, contact surface can be increased (Battiato and Diserens, 2013) or it can be used with double wheels (Damanauskas et al., 2015), both of which increase the area of the wheel contact with the soil.

In recent years, artificial intelligence techniques have been developed to model complex and uncertain systems. An efficient example of these techniques is the integration of artificial neural network (ANN) and fuzzy inference system. Fuzzy logic performs the inference mechanism with uncertainty in recognition while the ANN also has the ability to learn, adapt, and process in parallel. The hybrid system is called Adaptive Neuro-Fuzzy Interference System

Contact address: Gholamhossein Shahgholi, University of Mohaghegh Ardabili, Faculty of Agriculture and Natural Resources, Department of Biosystem Engineering, Ardabil, Iran, e-mail: gshahgholi@yahoo.com

(ANFIS) (Buckley and Hayashi, 1994). This method can solve complex issues relying on learning capabilities and parallel processing capabilities in ANNs. In terms of fuzzy systems, an approximate decision-making process is based on individual or group human experience. In these systems, the quantitative modelling is performed qualitatively and intuitively (instead of using quantitative values) and thus it is necessary to deal with indeterminants (Wang, 1997). Nevertheless, these systems do not have the ability to learn and, in confrontation with the complex systems, the regulation of membership functions and required rules are time-consuming and difficult. Although the ability of fuzzy systems has been approved in solving of complex problems related to modelling and prediction, control, and artificial intelligence (Wang, 1997), given the complementary (rather competitive) capabilities of these two solutions, it is possible to simultaneously use their advantages by combining them. In a research conducted by Taghavifar and Mardani (2014), authors predicted energy efficiency indicators using ANFIS. Input parameters included wheel load, speed, and slip, each of them at three levels. The results of this study showed a high prediction accuracy ($MSE = 0.0166$ and $R^2 = 0.98$). Ghadernejad et al. (2018) conducted a study to predict soil compaction under tractor wheels, utilizing the ANFIS model with four inputs: manure, number of passes, moisture, and depth. The results of this study showed a higher accuracy in predicting soil density than the regression model.

The objective of this study is to evaluate the tractor performance indices (slip and rolling resistance) in front-wheel-drive, rear-wheel-drive, and four-wheel-drive modes. Furthermore, ANFIS models were designed to predict tractor slip and rolling resistance in different tractor configurations, taking into account ballast weights, tire inflation pressure, various travel speeds of the tractor, and different required drafts.

Material and methods

Field tests were conducted at the Research Farm of Ardabil Agricultural Research Center (38° 12' 46.6" N, 48° 17' 42.2" E, and 1,350 m above sea level). The field was flat and had common barley (*Hordeum vulgare* Linnaeus) stubble residues from the previous season. Soil texture was loamy clay. Moisture and other soil properties were measured in 30 randomly selected points within the whole field at two depths: 0–25 and 25–50 cm. Results are presented in Table 1. Observed parameters included different levels of tractor forward speed (1.26, 3.96, and 6.78 km·h⁻¹), tire inflation pressure (170, 200, and 230 kPa), ballast weights (0, 150, and 300 kg), tractor motion systems (front-wheel-drive, rear-wheel-drive, and four-wheel-drive), and pulling force (2, 6, and 10 kN) for each experiment, on the basis of which two indices of slip and rolling resistance were measured. Type of motion system is not a numerical property, yet the modelling requires numerical values. In this regard, the tractor-implement system slip can represent an appropriate index of driving system type. In order to incorporate the effect of the driving system to the modelling process, the tractor slip value in different motion systems was used.

Table 1 Physical properties of the field soil

Property	Value
Sand (%)	40
Silt (%)	28
Clay (%)	32
Organic matter (g·100 g ⁻¹)	0.29
Plastic limit	25.76
Liquid limit	39.81
Plasticity index	14.05
(%) Field capacity based on dry weight	10.13
Dry bulk density (0–25 cm) (g·cm ⁻³)	1.35
Dry bulk density (25–50 cm) (g·cm ⁻³)	1.46
Moisture content based on dry weight (%) (0–25 cm)	9.3
Moisture content based on dry weight (%) (25–50 cm)	10.4

Technical characteristics of the Goldoni 240 tractor (4WD) used for testing are presented in Table 2. The front and rear tractor differentials related to the driving system were alternately disabled for the experiments, so the tractor could operate either as having front or rear wheel drive system. A subsoiler was used to create draft. Variation in the draft was obtained by changing the depth of subsoiler operation. Drafts of 2, 6 and 10 kN were obtained using a subsoiler tine at a depth of 30 cm, two subsoiler tines at a depth of 30 cm and two subsoiler tines at a depth of 50 cm, respectively. To measure the rolling resistance, the Goldoni 240 tractor in unloaded mode was towed by another tractor and the force required to move the Goldoni 240 tractor was measured using load cell installed between the two tractors. The draft applied to the tractor was measured using a three-point connecting dynamometer (Abbaspour-Gilandeh and Haghghat-Shishvan, 2011). The variation in the measured draft was in the range of ± 0.05 N.

Table 2 Tractor characteristics

Specifications	Unit	Value
Type of tractor engine	–	Diesel (3 Cylinders)
Engine power	(kW)	30.8
Static weight on front tires	(kg)	705
Static weight on rear tires	(kg)	360

The tractor wheel speed was measured utilizing an inductive proximity sensor mounted in line with the outer edge of a 34-tooth sprocket fixed inside the rear wheel (Fig. 1). Inductive proximity sensor is a non-contact device that is set up on a radio frequency field with an oscillator and a coil. Presence of a metal object (tooth) changes the field and the sensor detects the change. The resolution is 0.0003 m·s⁻¹. The sensor detected passing of each tooth during the wheel rotation so that with each full rotation of the gear or rear wheel, digital display of pulse meter attached to a magnetic sensor displayed the number of gear teeth. This number was divided by 34 to calculate the wheel rotation.



Fig. 1 Wheel speed transducer for measuring of tire rotation

Distance travelled was calculated by having a perimeter of the rear wheel. Dynamic rolling radius was determined and considered in computing rear wheel perimeter. The actual speed of the tractor was easily computed by measuring the time required to travel this distance using a stopwatch. The following Eq. (1) was used to calculate the slip:

$$Slip(\%) = 1 - \frac{v_a}{v_t} \cdot 100 \tag{1}$$

where:

- v_a – actual velocity ($m \cdot s^{-1}$)
- v_t – theoretical velocity ($m \cdot s^{-1}$)

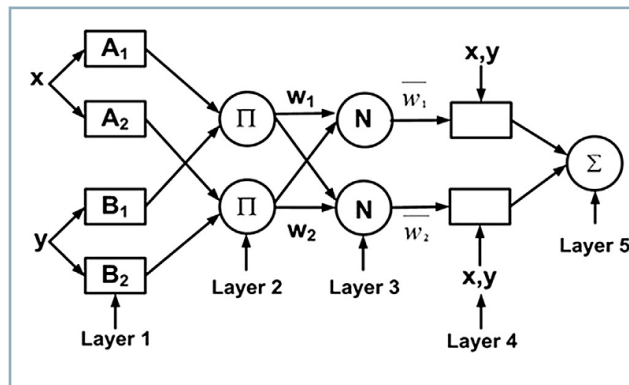


Fig. 2 Basic structure of the Adaptive Neuro-Fuzzy Inference System (ANFIS)

Adaptive neuro-fuzzy inference system

ANFIS is a multi-layer adaptive network consisting of main elements and functions of fuzzy logic systems. In general, the ANFIS system consists of a 5-layer structure with a number of input variables, each of which has two or more membership functions. Fig. 2 shows the ANFIS network architecture with two inputs, one output, and two rules.

In this study, two models for predicting slip and rolling resistance were developed in ANFIS. The first model is based on 5 input factors including inflation pressure, ballast weight, pulling force, tractor driving system, and forward speed. The second model is based on four input factors including inflation pressure, ballast weight, tractor driving system, and forward speed. Grid partition structure was used to create the network. Four common types of triangular, trapezoidal,

Table 3 Selected rules in the slip prediction model

Rules	Input variables					Linear output function (% slip)
	D	MS	IP	BW	S	
1	L	L	L	L	L	Slip = 1.28D + 1.477MS + 0.02369IP + 0.006237BW + 0.4499S - 2.768
5	L	L	H	L	L	Slip = -0.02834D + 0.1137MS + 0.02552IP - 0.0121BW - 0.271S + 2.046
17	H	L	L	L	L	Slip = 0.4836D + 2.121MS + 0.03794IP + 0.04143BW + 0.4147S + 0.7349
21	H	L	H	L	L	Slip = -1.277D + 4.096MS + 0.1376IP - 0.01722BW + 0.2468S - 0.5424
25	H	H	L	L	L	Slip = 0.03331D - 2.112MS + 0.2052IP + 0.06992BW + 0.3297S - 0.1642
32	H	H	H	H	H	Slip = -0.4357D - 2.77MS + 0.1043IP + 0.03969BW - 0.1946S + 0.0002872

D – draft; MS – motion system; BW – ballast weight; IP – inflation pressure; S – speed

Table 4 Selected rules in the motion resistance prediction model

Rules	Input variables				Linear output function (rolling resistance)
	MS	IP	BW	S	
1	L	L	L	L	MR = 0.3103MS + 0.002011IP + 0.00459BW + 0.01378S - 0.005265
2	L	L	L	H	MR = 0.2182MS + 0.00149IP + 0.003894BW + 0.02285S + 0.006151
5	L	H	L	L	MR = 0.1141MS + 0.003541IP - 0.0004052BW - 0.02053S + 0.003915
10	H	L	L	H	MR = -0.1223MS + 0.006777IP + 0.003032BW + 0.04878S + 0.0007311
14	H	H	L	H	MR = -0.119MS + 0.008611IP + 0.003029BW - 0.02972S - 0.0004734
16	H	H	H	H	MR = -0.08654MS + 0.003808IP + 0.004001BW + 0.02254S + 2.343e-05

D – draft; MS – motion system; BW – ballast weight; IP – inflation pressure; S – speed

Gaussian, and generalized-bell membership functions were considered for representing inputs. The number of membership functions for each input was considered to be the minimum possible value of 2 to prevent the creation of high rules and excessive system complexity. The input membership function used in this network is the linear type. The hybrid optimization method was used for network learning. The number of rules created by the network for slip and rolling resistance models is 32 and 16, respectively. Since the number of rules created is so high, there are presented only a few of them for a better understanding of ANFIS modelling (Tables 3 and 4). These rules were based on the fuzzy type Takagi-Sugeno-Kang (TSK). In this system, the foreground (if-then) is represented by fuzzy rules, but the resultant part is non-fuzzy and is a linear combination of input variables. The range of all inputs was divided into two parts: the low and the high areas, which were represented by the membership functions L and H, respectively.

According to the weight of each rule, the final output value of the model was calculated by averaging the predicted values by the linear functions of each rule. The weight of each rule was equal to the minimum degree of membership of the inputs of its rule. Finally, the final output of the model was calculated from the following Eq. (2).

$$f = \frac{w_1 f_1 + w_2 f_2}{w_1 + w_2} \tag{2}$$

where:

f_1, f_2 – linear functions related to rules 1 and 2, respectively
 w_1, w_2 – weights corresponding with each rule

To evaluate the ability of developed models, two statistical measures of relative error (ϵ) and coefficient of determination (R^2) were used. These were given by Eqs. (3) and (4) (Carman, 2008):

$$\epsilon = \frac{100}{N} \sum_{i=1}^N \frac{Y_{measured} - Y_{predicted}}{Y_{measured}} \tag{3}$$

$$R^2 = \frac{\sum_{i=1}^N (Y_{measured} - Y_{predicted})^2}{\sum_{i=1}^N (Y_{measured} - Y_{mean})^2} \tag{4}$$

where:

$Y_{measured}, Y_{predicted}$ – measured and predicted values, respectively

Y_{mean} – average value of all measured data

Furthermore, in this research, several multiple linear regression models were prepared in SPSS software to gain more knowledge on the effect of each input variable on the slip and rolling resistance.

Results and discussion

Tables 5 and 6 present the structural parameters of the models and their statistical measures for evaluating their performance. The results (Tables 5 and 6) show the high predictive power ($R^2 \geq 0.99$ and ϵ (%) ≤ 4) of all models. The best model for predicting slip uses triangular-shaped membership function (Trimf) with $R^2 = 0.997$ and $\epsilon = 3.08\%$. The best model for prediction of the rolling resistance is the one that uses the generalized bell-shaped membership function (Gbellmf) with $R^2 = 0.9893$ and $\epsilon = 1.89\%$.

Tables 7 and 8 present the statistical characteristics of the stepwise regression model for predicting slip and rolling resistance, respectively. The statistical models of slip prediction had $R^2 = 0.867$ and ϵ (%) = 19, and the rolling resistance prediction had $R^2 = 0.958$ and ϵ (%) = 5. According to the statistical factors, ANFIS models presented high accuracy in predicting the tractor slip and its rolling resistance. However, in comparison to the ANFIS models,

Table 5 The characteristics of the best structure of developed ANFIS architectures for slip; the bolded values show outperforming models

Model	Type of MF		Number of MF		Optimization method	Test	
	Input	Output	Input	Epoch		ϵ (%)	R^2
Grid Partition	Trimf	Linear	2 2 2 2 2	20	Hybrid	3.08	0.997
Grid Partition	Gaussmf	Linear	2 2 2 2 2	20	Hybrid	3.31	0.997
Grid Partition	Trapmf	Linear	2 2 2 2 2	20	Hybrid	3.24	0.997
Grid Partition	Gbellmf	Linear	2 2 2 2 2	20	Hybrid	3.67	0.996

Table 6 The characteristics of the best structure of developed ANFIS architectures for rolling resistance; the bolded values show outperforming models

Model	Type of MF		Number of MF		Optimization method	Test	
	Input	Output	Input	Epoch		ϵ (%)	R^2
Grid Partition	Trimf	Linear	2 2 2 2	20	Hybrid	2.69	0.9808
Grid Partition	Gaussmf	Linear	2 2 2 2	20	Hybrid	2.16	0.9871
Grid Partition	Trapmf	Linear	2 2 2 2	20	Hybrid	2.26	0.9866
Grid Partition	Gbellmf	Linear	2 2 2 2	20	Hybrid	1.89	0.9893

regression models have invaluable benefits. The regression model directly deals with the impact of each factor and it tries to provide a model, in which the importance and impact of each of the factors is clearly evident. In respect to the

standard coefficients listed in Table 7, draft, tractor driving system, inflation pressure, ballast weight, and travel speed showed the greatest effect on the slip, in the presented order. Moreover, in respect to the standard coefficients

Table 7 Statistical characteristics of stepwise regression model for slip

Model	Unstandardized coefficients		Standardized coefficients		
	B	Std. error	Beta	t	sig
(Constant)	-15.474	1.644		-9.413	0.000
D	1.622	0.056	0.689	29.126	0.000
MS	4.330	0.223	0.460	19.436	0.000
IP	0.083	0.007	0.263	11.129	0.000
BW	-0.016	0.001	-0.257	-10.847	0.000
S	-0.734	0.81	-0.215	-9.089	0.000

Table 8 Statistical characteristics of stepwise regression model for rolling resistance

Model	Unstandardized coefficients		Standardized coefficients		
	B	Std. error	Beta	t	sig
(Constant)	-0.545	0.069		-7.909	0.000
MS	0.327	0.010	0.788	34.338	0.000
BW	0.001	0.000	0.451	19.674	0.000
IP	0.005	0.000	0.358	15.604	0.000
S	-0.014	0.003	-0.090	-3.933	0.000

Constant is y-intercept in a linear function

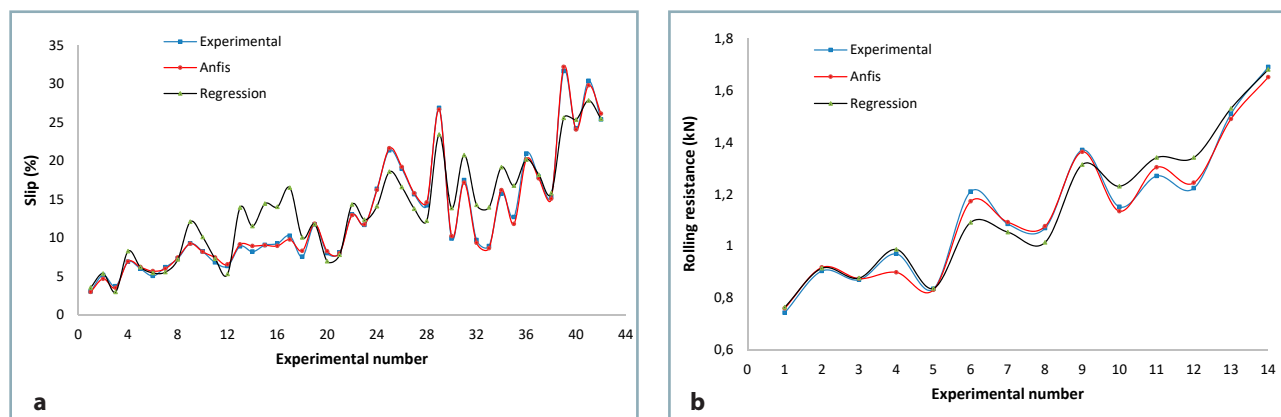


Fig. 3 Comparison of the values predicted by regression and ANFIS models with the observed values for (a) slip, (b) rolling resistance

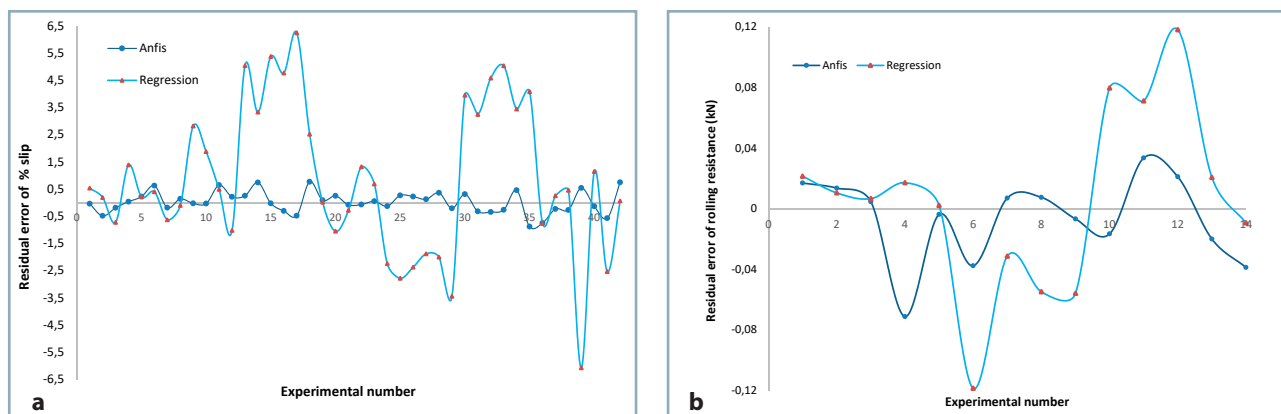


Fig. 4 Variation of the values predicted by regression and ANFIS models from the observed values for (a) slip, (b) rolling resistance

listed in Table 8, the tractor driving system, ballast weights, inflation pressure, and tractor speed had the greatest impact on the rolling resistance, in the presented order.

Figs. 3a and 3b illustrate the mapping between the experimental and predicted values for slip and rolling resistance by the ANFIS and stepwise regression models. Clearly, in contrast to the regression model, the ANFIS model provides a more accurate mapping of the experimental and predicted values. In addition to this, the deviation between the measured values and predicted values of the models were calculated and plotted. Figs. 4a and 4b show that the standard deviation for the predicted values of the ANFIS model for slip (-0.88 to 0.76) and the rolling resistance (-0.033 to 0.071) are much lower than the deviation of the predicted values of the stepwise regression models for slip (-6.08 to 6.24) and rolling resistance (-0.118 to 0.1186).

Investigation of slip and rolling resistance as a result of the application of experimental factors

The 3D surface curves of slip and rolling resistance as two indicators of the drive wheel performance are shown in Figs. 5 and 6, respectively. As it is clear from Fig. 5a, slip increases with increasing draft, but the use of four-wheel-drive mode makes it possible to achieve the maximum draft of 10 kN at a relatively low slip level of 12.4%, while when in the front-

wheel-drive mode, this pulling force was achieved at a high slip level of 25.5%. Many studies have reported that draft was the most important factor in terms of increasing the slip and optimal and economical slipping is recommended in the range of 10–15% (Battiato and Diserens, 2013; Lacour et al., 2014; Battiato and Diserens, 2017). Fig. 5b illustrates the interaction between the ballast weights and tire inflation pressure. It indicates that the slip decreases with decrease in inflation pressure and increase in the ballast weight. Scrutinizing Fig. 5b reveals that the slip decreases with decreasing inflation pressure and increasing ballast weight so that by applying the inflation pressure of 170 kPa and ballast weight of 300 kg, a slip value of less than 10% can be achieved, while applying the inflation pressure of 230 kPa and without ballast weight, the slip level was higher than 20%. Reducing the slip by raising the ballast weight and decreasing the inflation pressure is because both factors increased the wheel-soil contact area and with the improvement of soil and wheel conflict, the tire slip was reduced (Muhsin, 2010; Battiato and Diserens, 2013; Damanuskas and Janulevicius, 2015).

Fig. 6a shows that the increase of ballast weight leads to an increase in the rolling resistance, since the wheel load plays a major role in increasing the wheel's rolling resistance. Such a process has also been reported by other researchers (Taghavifar and Mardani 2013; Taghavifar and Mardani

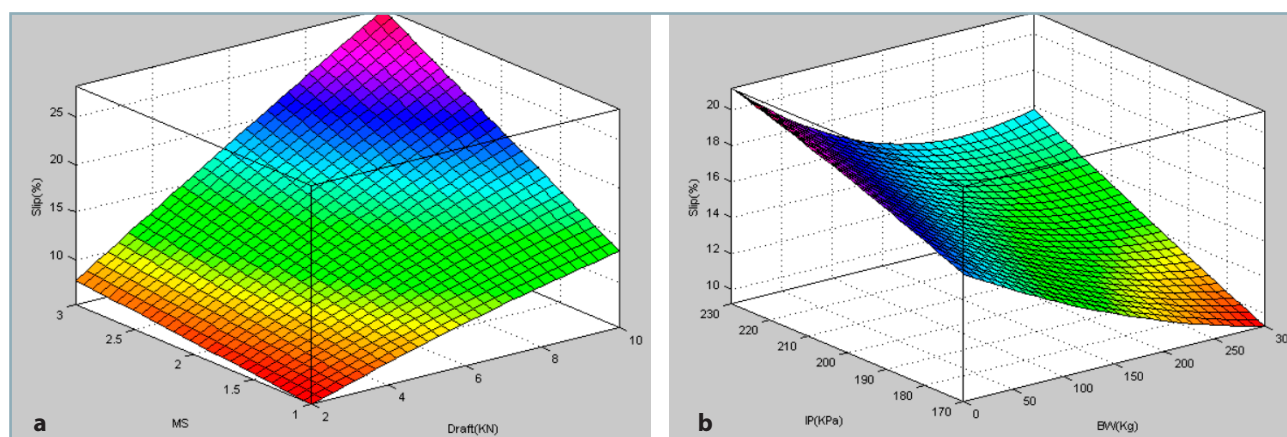


Fig. 5 3D surface curves of slip by interactions of input parameters; (a) interaction between MS and draft, (b) interaction IP and BW

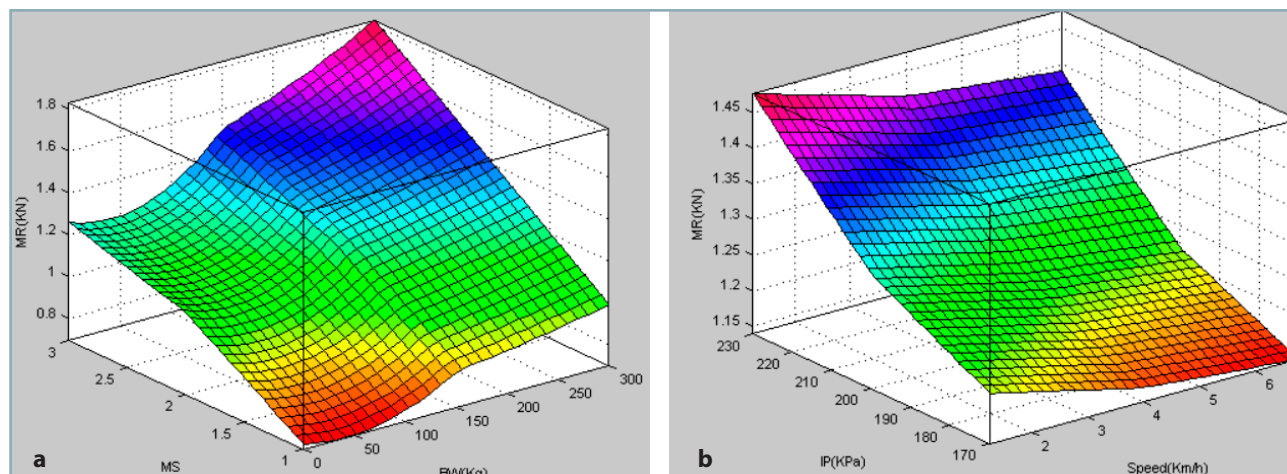


Fig. 6 3D surface curves of MR by interactions of input parameters; (a) interaction between MS and BW, (b) interaction IP and speed

2014). In Fig. 6b, increasing travel speed reduced the rolling resistance, which can be attributed to the fact that, at lower speeds, the wheel loading time on the soil increases, resulting in the increased tire sinkage in soil and soil deformation. The energy used to deform the soil increases rolling resistance, so the movement speed can be increased to prevent energy loss in the soil. The type of tractor driving system has a significant effect on the reduction of rolling resistance. As shown in Fig. 6a, the four-wheel-drive mode had a lower rolling resistance in contrast to two the other observed modes. This result can be explained by the fact that drive wheel contact area in four-wheel-drive mode is doubled in comparison to two other modes, and increase in the contact area of wheels with the soil reduced the rolling resistance. The influence of contact area of the wheel with the soil has been investigated by several researchers who reported similar results (Damauskas et al., 2015). In regards to this, Botta et al. (2012) compared the rolling resistance of a four-wheel drive and two-wheel drive tractor. Although the four-wheel-drive tractor had a higher weight, it had a lower rolling resistance than a two-wheel-drive tractor. As shown in Fig. 6b, reduction of tire inflation pressure reduces the rolling resistance. The influence of inflation pressure on the rolling resistance is explained by the contact area of the tire with the soil.

Conclusion

- In contrast to the stepwise regression model, the ANFIS model showed a higher performance in predicting slip and rolling resistance.
- Applying the four-wheel-drive mode without the use of ballast weights and reduction of the inflation pressure resulted in the lower level of slip and rolling resistance. Therefore, in the four-wheel-drive mode, there is no need for increasing the ballast weights and decreasing the inflation pressure. This solution is superior, since any increase in weight and reduction in pressure cause damage to tires and reduce their lifespan.
- It was found that draft, tractor driving system, inflation pressure, ballast weights, and tractor travel speed have the greatest effect on the slip, in the presented order. Furthermore, the results showed that the tractor driving system, ballast weight, inflation pressure, and tractor travel speed also have a significant impact on the rolling resistance, in the presented order.
- Ballast weight showed both advantages and disadvantages for traction performance, because by increasing the ballast weight, slip decreases and rolling resistance increases. Ballast weight should increase when the tractor slip is high so that the advantages of slip reduction can compensate for the disadvantages of increasing the rolling resistance.

References

- ABBASPOUR-GILANDEH, Y. – HAGHIGHAT-SHISHVAN, S. 2011. Extended octagonal ring transducers for measurement of tractor-implement forces. In *Instruments and Experimental Techniques*, vol. 54, no. 1, pp. 136–140.
- BARBOSA, L. A. P. – MAGALHAES, P. S. G. 2015. Tire tread pattern design trigger on the stress distribution over rigid surfaces and soil compaction. In *Journal of Terramechanics*, vol. 58, pp. 27–38.
- BATTIATO, A. – DISERENS, E. 2013. Influence of tyre inflation pressure and wheel load on the traction performance of a 65kW MFWD tractor on a cohesive soil. In *Journal of Agricultural science*, vol. 5, no. 8, pp. 197–215.
- BATTIATO, A. – DISERENS, E. 2017. Tractor traction performance simulation on differently textured soils and validation: a basic study to make traction and energy requirements accessible to the practice. In *Soil and Tillage Research*, vol. 166, pp. 18–32.
- BATTIATO, A. – DISERENS, E. – LALLOUI, L. – SARTORI, L. 2013. A mechanistic approach to topsoil damage due to slip of tractor tyres. In *Journal of Agricultural Science and Applications*, vol. 2, no. 3, pp. 160–168.
- BOTTA, G. – TOLON-BECERRA, A. – TOURN, M. – LASTRA-BRAVO, X. – RIVERO, D. 2012. Agricultural traffic: Motion resistance and soil compaction in relation to tractor design and different soil conditions. In *Soil and Tillage Research*, vol. 120, pp. 92–98.
- BUCKLEY, J. J. – HAYASHI, Y. 1994. Fuzzy neural networks: A survey. In *Fuzzy Sets and Systems*, vol. 66, no. 1, pp. 1–13.
- CARMAN, K. 2008. Prediction of soil compaction under pneumatic tires using fuzzy logic approach. In *Journal of Terramechanics*, vol. 45, no. 4, pp. 103–105.
- DAMANAUSKAS, V. – JANULEVICIUS, A. 2015. Differences in tractor performance parameters between single-wheel 4WD and dual-wheel 2WD driving systems. In *Journal of Terramechanics*, vol. 60, pp. 63–73.
- DAMANAUSKAS, V. – JANULEVICIUS, A. – PUPINIS, G. 2015. Influence of extra weight and tire pressure on fuel consumption at normal tractor slippage. In *Journal of Agricultural Science*, vol. 7, no. 2, pp. 55–67.
- ELWALEED, A. K. – YAHYA, A. – ZOHADIE, M. – AHMAD, D. – KHEIRALLA, A. F. 2006. Effect of inflation pressure on motion resistance ratio of a high-lug agricultural tyre. In *Journal of Terramechanics*, vol. 43, no. 2, pp. 69–84.
- GHADERNEJAD, K. – SHAHGHOLI, G. – MARDANI, A. – GHAFOURI CHIYANEH, H. 2018. Prediction effect of farmyard manure, multiple passes and moisture content on clay soil compaction using adaptive neuro-fuzzy inference system. In *Journal of Terramechanics*, vol. 77, pp. 49–57.
- JANULEVICIUS, A. – DAMANAUSKAS, V. – PUPINIS, G. 2018. Effect of variations in front wheels driving lead on performance of a farm tractor with mechanical front-wheel-drive. In *Journal of Terramechanics*, vol. 77, pp. 23–30.
- LACOUR, S. – BURGUN, C. – PERILHON, C. – DESCOMBES, G. – DOYEN, V. 2014. A model to assess tractor operational efficiency from bench test data. In *Journal of Terramechanics*, vol. 54, pp. 1–18.
- MOITZI, G. – HAAS, M. – WAGENTRISTL, H. – BOXBERGER, J. – GRONAUER, A. 2013. Energy consumption in cultivating and ploughing with traction improvement system and consideration of the rear furrow wheel-load in ploughing. In *Soil and Tillage Research*, vol. 134, pp. 56–60.
- MOINFAR, A. M. – SHAHGHOLI, G. 2018. Dimensional analysis of the tractor tractive efficiency parameters. In *Acta Technologica Agriculturae*, vol. 21, no. 3, pp. 94–99.
- MUHSIN, S. J. 2010. Studying the power losses of two and four wheel drive tractors (2WD and 4WD) of Massey Ferguson 2680. In *Journal of Basrah Research Sciences*, vol. 36, no. 6, pp. 59–66.
- TAGHAVIFAR, H. – MARDANI, A. 2013. Investigating the effect of velocity, wheel load and inflation pressure on rolling resistance of radial ply tire. In *Journal of Terramechanics*, vol. 50, no. 2, pp. 99–106.
- TAGHAVIFAR, H. – MARDANI, A. 2014. On the modeling of energy efficiency indices of agricultural tractor driving wheels applying adaptive neuro-fuzzy inference system. In *Journal of Terramechanics*, vol. 56, pp. 37–47.
- WANG, L. X. 1997. *A Course in Fuzzy Systems and Control*. Prentice-Hall Inc.

Acta Technologica Agriculturae 4
Nitra, Slovaca Universitas Agriculturae Nitriae, 2019, pp. 122–127

THE INFLUENCE OF SELECTED EXTERNAL FACTORS ON TEMPERATURE OF PHOTOVOLTAIC MODULES

Matúš BILČÍK*, Monika BOŽIKOVÁ, Martin MALÍNEK

Slovak University of Agriculture in Nitra, Slovak Republic

The article deals with the impact of selected external factors on the temperature of photovoltaic module surfaces. Primary aim of this research is creation of temperature model for photovoltaic module, which would be usable under the real climatic conditions in Central Europe region. Fully autonomous measuring system was designed and created for temperature monitoring of different parts of photovoltaic modules. The measuring system consists of 24 temperature sensors, voltage inverter, control unit, transfer modules, receiver modules and temperature measuring module. The experiments were performed on photovoltaic modules installed on the roof of the University of Life Sciences in Prague during summer 2018. The temperature of photovoltaic modules significantly depends on the climatic conditions, which were monitored by the weather station. The temperature and the solar radiation dependencies for polycrystalline and monocrystalline photovoltaic modules were obtained in experiments conducted. The temperature relations were measured for different parts of photovoltaic module – active parts of photovoltaic module, frame, non-active parts of photovoltaic module, as well as ambient temperature. Final mathematical description of polynomial graphical dependencies was obtained after application of fitting procedure and regression analysis.

Keywords: temperature; solar radiation; dependence; measuring system; temperature sensor

Solar energy can be converted into electrical energy by using photovoltaics (Chander et al., 2015). Possibilities of photovoltaic (PV) system application have been described in publications by Čorba et al. (2009) and Miličević et al. (2012). The operating temperature of PV module depends on several factors, such as: solar radiation; ambient temperature; wind speed and direction; module material composition; mounting structure. These relations have been presented by authors Armstrong and Hurley (2010), Malínek et al. (2018), Bilčík and Božiková (2018) and Libra et al. (2017). All aforementioned conditions have a significant influence on PV cell energy production; however, the most crucial factor is temperature. The effects of the PV module operating temperature on the output efficiency have been described by Jones and Underwood (2001), Schott (1985), Servant (1985), Kafui et al. (2018) and their research results have shown that increasing temperature has a negative impact on the amount of power available. On the basis of the presented facts, the paper

at hand deals with the analysis of PV module temperature. Experiments under the real climatic conditions were conducted on the PV system with polycrystalline and monocrystalline PV modules at the Czech University of Life Sciences in Prague (Czech Republic). The temperature of PV module was monitored by fully autonomous measuring system with 24 temperature sensors. The climatic data were obtained from weather station at the same location as the PV system.

Material and methods

In terms of external factors having significant influence on the PV system operating parameters, temperature can be considered the most important. There are multiple different ways for the temperature measurement to be realized under the external conditions. In case of this research, autonomous measuring system was designed and constructed (Fig. 1). This system

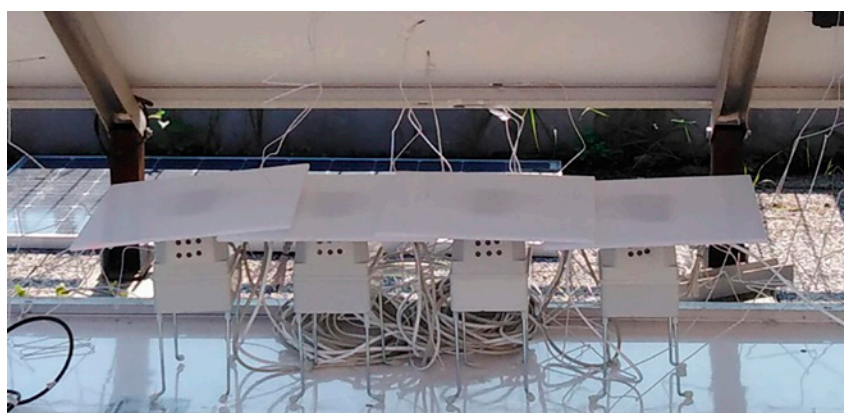


Fig. 1 Measuring system for temperature identification of PV modules

Contact address: Matúš Bilčík, Slovak University of Agriculture in Nitra, Faculty of Engineering, Department of Physics, Tr. Andreja Hlinku 2, 949 76 Nitra, Slovak Republic, e-mail: bilcikmatus@gmail.com

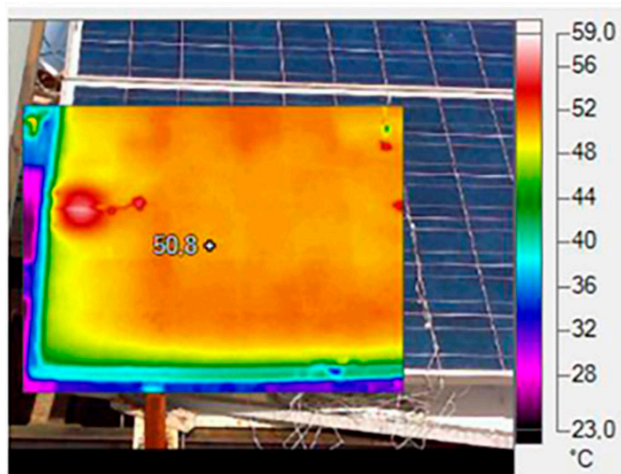


Fig. 2 Identification of temperature changes by thermocamera Fluke TiR1

contains measuring components and controller from producer (B&R, Austria) and it works fully automatically with the software programmed in Automation Studio.

The PV module consists of several components made of different materials; therefore, it is necessary to measure the temperature of the individual components of the PV module, the measuring system thereby has 24 temperature sensors with accuracy $\pm 0.75\%$. For the purpose of comparison of temperature measurements, detection of temperature changes in the PV module surface was also realized utilizing thermocamera Fluke TiR1 (Fluke Corporation, USA). On the basis of thermovision evaluation, it is clear that the different parts of the PV module showed different temperatures (Fig. 2).

Climatic data were monitored by weather station installed at the Czech University of Life Sciences in Prague. The ambient temperature (air temperature), air humidity, air pressure, rainfall, wind velocity, direction of wind and the global solar radiation were measured by a local weather station. The ambient temperature was measured using sensor HMP45C manufactured by Vaisala Inc. (Finland), the measurement accuracy of sensor is ± 0.5 °C. The intensity of global solar radiation was monitored by pyranometer CM11 (Kipp & Zonen, USA). The main experiment was performed on polycrystalline and monocrystalline PV modules. Technical parameters of these PV modules are presented in Table 1. Polycrystalline PV modules tend to have a slightly

lower heat tolerance than monocrystalline solar modules, meaning that they show a slightly worse performance under high temperatures in contrast to monocrystalline modules. Theory (Kafui et al., 2018) and practice have proved that heat can affect the performance of solar modules and shorten their lifespans.

Results and discussion

Relations for temperature, and solar radiation, as well as temperature dependencies, were obtained in these research experiments; research results are presented by graphical dependencies. Experimental measurements included monitoring of temperature of PV modules' active parts; temperature of non-active white parts of PV modules, and temperature of the PV module frames. Firstly, differences between temperatures of upper and lower parts of PV module were identified utilizing thermocamera; following experiments included measurements of the temperatures of these PV module parts. On the basis of measured data, temperature dependencies were produced (Figs. 3 and 4).

The main aim of this research is creating the simplified mathematical model for the temperature and solar radiation during the time range when the solar production of electrical energy by PV system culminates during the day. The modelled mathematical dependencies can be used for prediction of the PV module operational parameters. From the mathematical description point of view, it was necessary to smooth out the extreme parts of the temperature graphical dependencies by applying appropriate procedure.

Appropriate procedure eliminates the extremes of graphical dependencies not corresponding with the assumed trend of the graphical dependencies. This procedure was used for all measured dependencies. After its application, graphs (Figs. 5 and 6) with smooth curves were plotted; these can be described by nonlinear mathematical function. The next step in graphical dependencies processing was regression analysis. It allowed the selection of the most suitable graphical dependence. On the basis of the descriptive characteristics of graphical dependencies (coefficients of regression equation, coefficients of determination etc.), the second-degree polynomial function (Eq. 1) was selected for all cases.

$$T = At^2 + Bt + C \quad (1)$$

Table 1 Technical parameters of PV modules

Type	Polycrystalline	Monocrystalline
Efficiency (%)	14	17
Brand	Yingli Solar	Sun-Earth
Module type	YL230P-29b	125*125-F
Rated maximum power (W)	230	170
Rated voltage (V)	29.5	35.4
Rated current (A)	7.8	4.8
Size (mm)	1590 × 990 × 45	1590 × 808 × 42

where:
 T – temperature of PV module part
 t – time

The coefficients of regression equations and coefficients of determinations are presented in Table 2.

In experiments presented, polynomial function for temperature

relations was obtained. However, various authors (Amstrong and Hurley, 2010; Jones and Underwood, 2001; Schott, 1985; Servant, 1985) presented temperature relations with linear or exponential shape. This difference between the results presented in literature and experimentally obtained results can be caused by a certain ambivalence in meaning in terms of

using the expression “the temperature of PV cell”. Aforementioned authors measured the temperature of PV cell, yet considering the theory, there is a difference between temperature of the PV cell and temperature of the PV cell surface. These experiments monitored the temperature of PV cell surface, because the temperature measurement inside the PV cell is technically difficult to realize under the real operational conditions.

Determination coefficients are relatively high, their values are in the range $R^2 = 0.85 - 0.97$. The polynomial function of the second degree was selected correctly, not only from the mathematical point of view but also from the point of view of physical theory that predicts the polynomial progress of temperature in relation to the culmination of the sun’s intensity.

The second aim of this research was to identify the influence of the ambient temperature on the temperature of different parts of PV module, so there was performed correlation analysis on all graphical dependencies. The results of correlation analysis are presented in Table 2 as coefficients of correlation and degrees of correlation. The correlation coefficients were found in the range from -0.36 to 0.7. The temperature of both PV module frames and ambient temperature correlate to a high degree, with a correlation coefficient 0.7. The temperature of other polycrystalline PV module parts correlates to a lesser degree. The correlation coefficient of -0.36 was found for correlation between the ambient temperature and temperature of the monocrystalline PV cell surface,

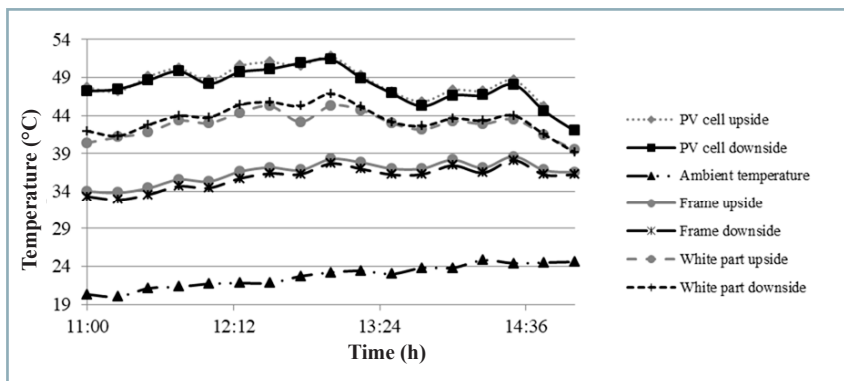


Fig. 3 Real temperature dependencies for different parts of polycrystalline PV module and ambient temperature

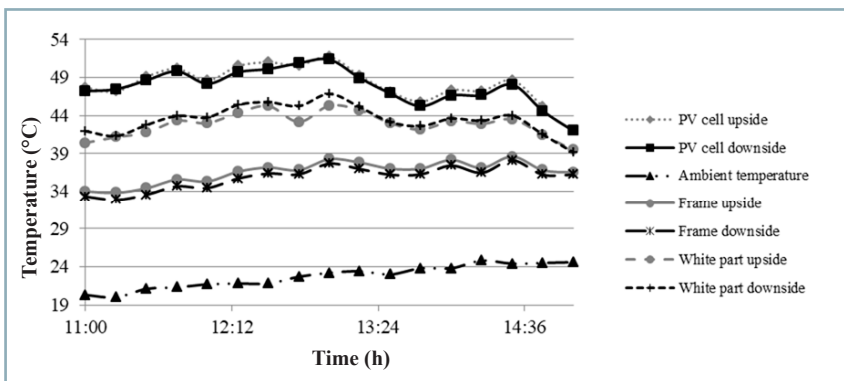


Fig. 4 Real temperature dependencies for different parts of monocrystalline PV module and ambient temperature

Table 2 Regression coefficients and correlation coefficients for temperature relations

Part of PV module	Coefficients of the regression equations			Coefficients of determinations	Coefficient of correlation	Correlation
	A	B	C			
Polycrystalline PV module						
PV cells	-1035.70	1101.40	-240.06	0.97	0.34	mild
Frame	-642.80	699.13	-149.84	0.97	0.70	high
White part	-814.68	865.29	-181.27	0.98	0.32	mild
Monocrystalline PV module						
PV cells	-822.91	874.38	-181.20	0.85	-0.36	any
Frame	-474.47	538.63	-113.84	0.96	0.70	high
White part	-751.88	812.78	-181.20	0.97	0.04	low

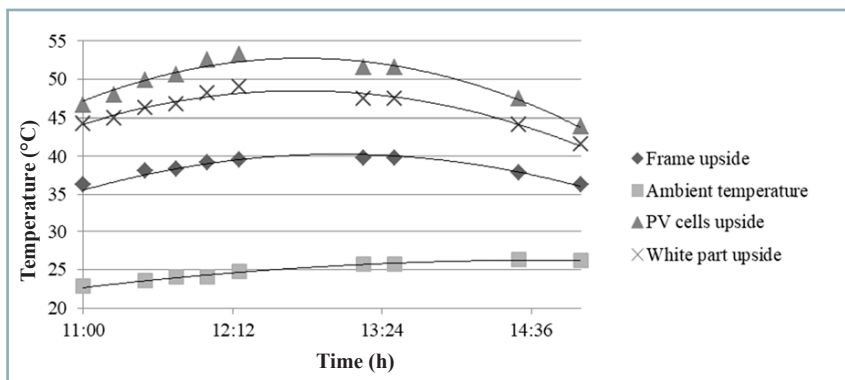


Fig. 5 Temperature dependencies for different parts of polycrystalline PV module and ambient temperature after appropriate procedure application and regression analysis

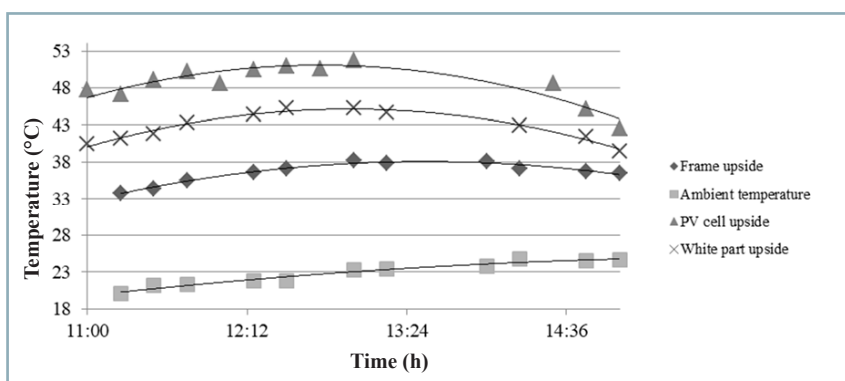


Fig. 6 Temperature dependencies for different parts of monocrystalline PV module and ambient temperature after appropriate procedure application and regression analysis

meaning that there is no correlation and mathematical dependence between the temperature of monocrystalline PV cell surface and ambient temperature. Correlation coefficient 0.039 was observed for the relation between the temperature of white area and the ambient temperature. This correlation coefficient means a low degree of correlation.

Next part presents the temperature and solar radiation dependencies. The fluctuations in the intensity of sunshine due to cloudiness change are shown in Figs. 7 and 8. These solar radiation intensity fluctuations also have influence on PV cell surface temperature. The extremes observed in real dependencies were eliminated by application of the fitting procedure.

After fitting procedure application, graphs with smooth curves (Figs. 9 and 10) were plotted and a polynomial function of a second degree was selected as a model regression equation via regression analysis. The polynomial function of a second degree is appropriate from the theoretical and practical point of view.

These functions are generally represented by a regression equation (Eq. 2).

$$I = Et^2 + Ft + G \quad (2)$$

where:

- I – intensity of solar radiation
- t – time

Table 3 shows the coefficients of regression equation (Eq. 2) and the coefficients of determinations R^2 in the range 0.8 – 0.95.

Correlation coefficients between the temperature of different parts of polycrystalline and monocrystalline PV modules and the solar radiation intensity ranged from 0.69 to 0.9, indicating a high degree of correlation. Measurement results and statistical evaluation confirmed a well-known fact from literature, i.e. that the intensity of solar radiation affects the temperature of the PV module most significantly.

$$T_c = T_a + \alpha G_T (1 + \beta T_a) (1 - \gamma v_w) \quad (3)$$

Eq. 3 presents the temperature model for cell operating temperature T_c by Servant (1985). In this model, T_a is the ambient temperature, G_T is the global solar radiation, η_c represents module electrical efficiency, and v_w is

Table 3 Regression coefficients and correlation coefficients for time-solar radiation relations

Part of PV module	Coefficients of the regression equations			Coefficients of determinations	Coefficient of correlation	Correlation
	A	B	C			
Polycrystalline PV module						
PV cells	-844.75	909.13	-192.33	0.80	0.80	high
Frame	-590.66	645.21	-135.68	0.92	0.89	high
White part	-542.29	577.58	-105.98	0.82	0.69	high
Monocrystalline PV module						
PV cells	-828.61	859.49	-172.08	0.91	0.88	high
Frame	-350.99	359.11	-73.58	0.95	0.39	mild
White part	-630.92	676.84	-137.13	0.95	0.90	high

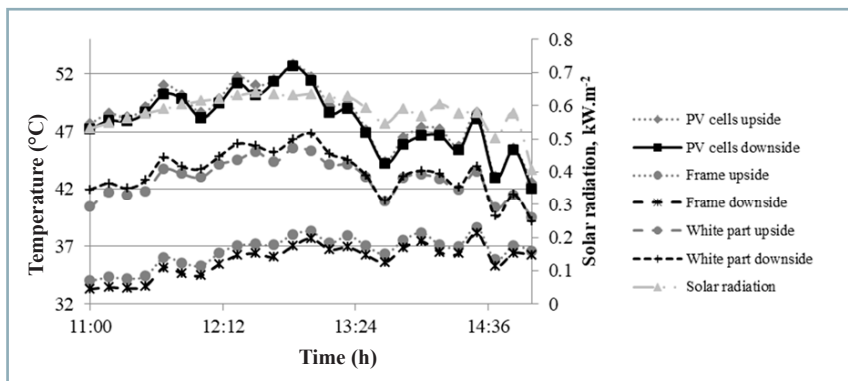


Fig. 7 Real temperature and solar radiation dependencies for different parts of polycrystalline PV module

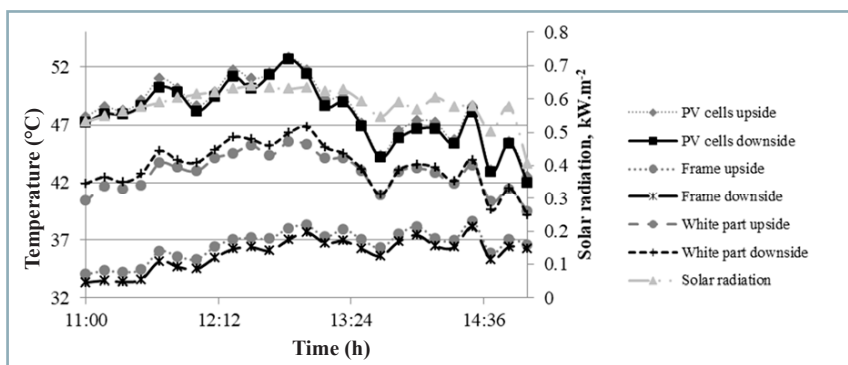


Fig. 8 Real temperature and solar radiation dependencies for different parts of monocrystalline PV module

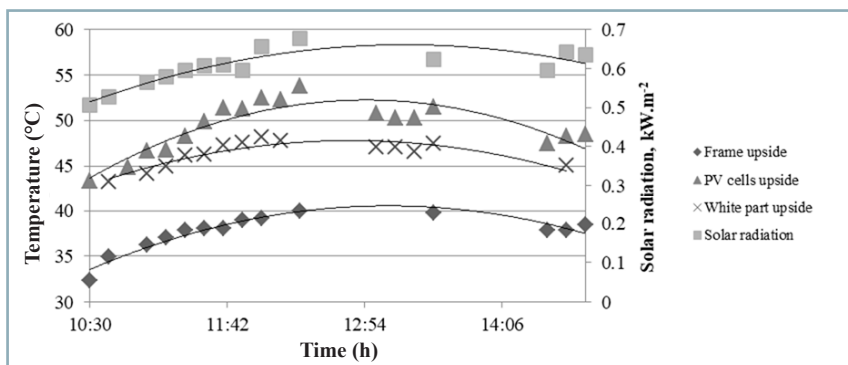


Fig. 9 Temperature dependencies of polycrystalline PV module different parts and solar radiation after application of fitting procedure and regression analysis

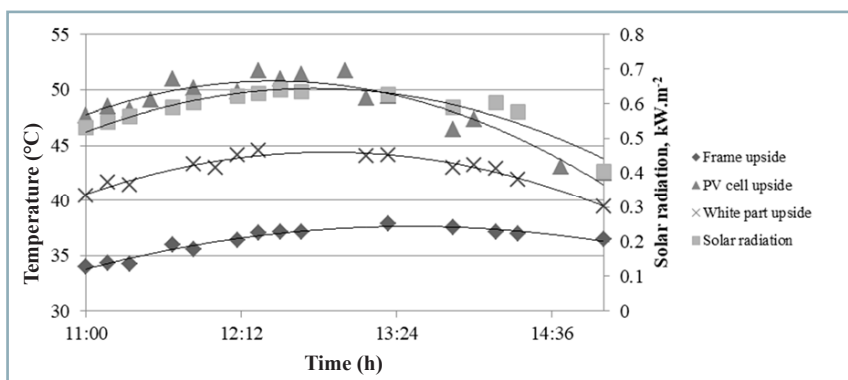


Fig. 10 Temperature dependencies of and solar radiation after application of fitting procedure and regression analysis

the constant wind velocity with value $1 \text{ m}\cdot\text{s}^{-1}$. Values of constants by Servant (1985) in Eq. (3) are $\alpha = 0.0138 (-)$, $\beta = 0.031 (-)$, and $\gamma = 0.042 (-)$.

$$T_c = T_a + \frac{G_T}{G_{NOCT}} (T_{C,NOCT} - T_{a,NOCT}) \left(1 - \frac{\eta_c}{\tau\alpha} \right) \quad (4)$$

The temperature model provided by Davis et al. (2001) can be described by Eq. (4); parameters and quantities are the same as in Eq. (3) except for physical quantities with lower subscript designation *NOCT* for the nominal operating cell temperature. The nominal operating cell temperature is defined as a temperature of a device under the conditions of the nominal terrestrial environment, where the solar radiation flux is $800 \text{ W}\cdot\text{m}^{-2}$. Ambient temperature is $20 \text{ }^\circ\text{C}$, average wind speed is $1 \text{ m}\cdot\text{s}^{-1}$, electrical load is at zero (i.e. open circuit) and free-standing mounting frame is oriented regularly, to solar noon. Parameter α indicates the solar absorptance of PV layer and τ is transmittance of glazing. Both equations predict temperature of PV module with the linear trend. Eq. 1 is the polynomial function of the second degree and is more suitable for this purpose, because the culmination of sun intensity has polynomial trend as well.

Conclusion

On the basis of the presented results obtained in PV module temperature measurements and measurements of solar radiation intensity, it is evident that the reaction of PV module temperature is dynamic in working conditions. This fact is clear for periods during which the changes in solar radiation intensity due to cloudiness were observed. Another result in relation to the Central Europe is that temperature changes in different parts of PV modules can be characterised by polynomial function of the second degree, which was determined by the regression analysis of experimental data and by application of an appropriate procedure. The correlation analysis confirmed the significant influence of solar radiation intensity on

temperature of polycrystalline PV module, as well as partial influence of ambient temperature on PV module temperature. The temperature of PV module depends on the material of PV module components.

Acknowledgement

This work was supported by the Slovak Ministry of Education, Science, Research, and Sport under project KEGA 017SPU-4/2017 – Multimedia textbook of physics for engineers, and was co-funded by the European Community under project no 26220220180 – Building the Research Centre AgroBioTech.

References

- AMSTRONG, S. – HURLEY, W. G. 2010. A thermal model for photovoltaic panels under varying atmospheric conditions. In *Applied Thermal Engineering*, vol. 30, pp. 1488–1495.
- BILČÍK, M. – BOŽIKOVÁ, M. 2018. Wind speed and the selected time temperature dependencies for photovoltaic module In *Physics – Applications and Innovations. SUA in Nitra*, 145 pp. ISBN 978-80-552-1915-8.
- ČORBA, Z. – KALIČ, V. – MILIČEVIĆ, D. 2009. Photovoltaics systems in agriculture. In *Journal on Processing and Energy in Agriculture*, vol. 13, no. 4, pp. 328–331.
- DAVIS, M. W. – DOUGHERTY, B. P. – FANNEY, A. H. 2001 Prediction of building integrated photovoltaic cell temperatures. In *Journal of Solar Energy Engineering*, vol. 123, no. 3, pp. 200–210.
- CHANDER, S. – PUROHIT, A. – SHARMA, A. – NEHRA, S. P. – DHAKA, M. S. 2015. A study on photovoltaic parameters of mono-crystalline silicon solar cell with cell temperature. In *Energy Reports*, vol. 1, pp. 104–109.
- JONES, A. D. – UNDERWOOD, C. P. 2001. A thermal model for photovoltaic systems. In *Solar Energy*, vol. 70, no. 4, pp. 349–359.
- LIBRA, M. – POULEK, V. – KOUŘÍM, P. 2017. Temperature changes of I-V characteristics on photovoltaic cells as consequence of the Fermi energy level shift. In *Research in Agricultural Engineering*, vol. 63, no. 1, pp. 10–15.
- KAFUI, A. D. – SERES, I. – FARKAS, I. 2018. Efficiency comparison of different photovoltaic modules. In *Acta Technologica Agriculturae*, vol. 22, no. 1, pp. 5–11.
- MALÍNEK, M. – BILČÍK, M. – BOŽIKOVÁ, M. – PETROVIĆ, A. – KOTOULEK, P. – HLAVÁČ, P. 2018. The selected time temperature and wind speed dependencies for photovoltaic module. In *Journal on Processing and Energy in Agriculture*, vol. 22, no. 2, pp. 82–84.
- MILIČEVIĆ, D. – POPADIĆ, B. – DUMNIĆ, B. – ČORBA, Z. – KALIČ, V. 2012. Possibility of solar potential utilization in Republic of Serbia – practical example. In *Journal on Processing and Energy in Agriculture*, vol. 16, no. 3, pp. 109–112.
- SERVANT, J. M. 1985. Calculation of the cell temperature for photovoltaic modules from climatic data. In Bilgen, E., Hollands, K.G.T., editors. In *Proceedings of the 9th biennial congress of ISES – Intersol 85*, Montreal, Canada, extended abstracts, 370 pp.
- SCHOTT, T. 1985. Operation temperatures of PV modules. In *Proceedings of the sixth EC photovoltaic solar energy conference*. London, pp. 392–396.



Acta Technologica Agriculturae 4
Nitra, Slovaca Universitas Agriculturae Nitriae, 2019, pp. 128–133

MATHEMATICAL MODELLING OF SOLAR THERMAL COLLECTORS AND STORAGES

János TÓTH, István FARKAS*

Szent István University, Gödöllő, Hungary

Block-oriented modelling is a powerful tool in system design. The models developed this way can be used to study various systems, such as solar thermal systems. In the work presented, main goal is to compare different mathematical models of solar thermal devices. The difference in accuracy of such models in respect to the possibilities of a hardware-in-the-loop simulation will be discussed. Two models of solar thermal collectors will be compared and used in a system containing two different heat storages in order to study the behaviour of these models. The tests were carried out in a Simulink based block-oriented environment called SimSolar.

Keywords: block-oriented simulation; comparison; modelling; solar energy

The development of solar systems has been highly speeded up in the recent years. For this purpose, a lot of experiments were made and a lot of prototype systems were built. Nevertheless, it is expensive to build a physical system to perform experiments. With the aid of the computer assisted modelling methods such costs can be reduced, but these algorithms were created for a specific task and they do not provide very much flexibility.

Model-based design is a possible way to resolve this issue (Paterno, 2000). This design method utilizes mathematical models and the simulation of them to reduce the costs and to speed up the test phase. This approach is useful to analyse and develop an existing solution as well (Bilčík et al., 2018). There are working software packages for solar applications that use this method, for example the TRNSYS software (Kyn and Urban, 2013; TRNSYS, 2009) or the Polysun software (Lacoste et al., 2010). Reputation of these programs shows the potential in this field and a need for a reliable solution for educational intent. These commercial program-packages are proven-to-work, but they cannot be used for development purposes due to their prices.

Extension of the model-based design is the hardware-in-the-loop (HIL) simulation, in which real-time data are used for the model; this is achieved by using embedded systems and sensors. The „hardware“ part can be either FPGA devices or more common embedded systems, such as Arduino or Raspberry Pi (Velasquez et al., 2017). There are two main approaches to make a HIL simulation – one in which the simulation runs on a host machine and the embedded system acts like an input (a complex simulation can be built without the hardware limitations of the embedded system in such manner). The other method includes the entire simulation running on the embedded system; the system becomes portable, but it requires more advanced hardware in such case (Ilyas et al., 2018).

The presented simulations were performed using a custom-made Simulink library called SimSolar (Tóth and Farkas, 2017) software, which is a block-oriented modelling environment.

In this paper, the mathematical models of solar thermal collectors and the connected heat storages are presented. Aforementioned models are studied in a block-oriented simulation environment to show the differences in accuracy and to study the behaviour of such models in a system.

Material and methods

Used mathematical models of the solar thermal collectors and heat storages and the metrics of the comparison are presented in this section.

Models of solar collectors

Collector is a device converting the radiant energy of the Sun into heat in a solar thermal system. This component primarily determines the efficiency of the system, because the gathering of the energy occurs here. The two mathematical models of the collector, which describe the same device, are presented in this section.

Hottel-Vhillier (H-V) model

The Hottel-Vhillier model (Farkas, 1999) was applied to a collector as shown in Fig. 1.

Using the above introduced notations, the mathematical model is as follows:

$$T_{co}(\tau) = T_w(\tau) + \frac{I(\tau)}{\kappa_{aw}} \left(T_c(\tau) - T_w(\tau) - \frac{I(\tau)}{\kappa_{aw}} \right) \cdot \exp \left(\frac{-\kappa_{mw} \cdot W \cdot l}{c \cdot \frac{dm}{d\tau}} \right) \quad (1)$$

Contact address: István Farkas, Szent István University, Department of Physics and Process Control, Páter Károly u. 1, Gödöllő, H-2100 Hungary, e-mail: Farkas.Istvan@gek.szie.hu

where:

- τ – time (s)
- T_{co} – collector outlet temperature (°C)
- T_w – ambient temperature (°C)
- I – solar radiation ($W \cdot m^{-2}$)
- κ_{aw} – heat transfer coefficient between the absorber and the environment ($W \cdot m^{-2} \cdot K^{-1}$)
- T_{ci} – collector inlet temperature (°C)
- κ_{mw} – heat transfer coefficient between the working fluid and the environment ($W \cdot m^{-2} \cdot K^{-1}$)
- w – width of the collector (m)
- l – length of the collector (m)
- c – specific heat of the working fluid ($J \cdot kg^{-1} \cdot K^{-1}$)
- m – mass of the working fluid (kg)

The overall heat transfer parameters κ_{aw} and κ_{mw} are needed to be identified in order to get proper simulation results.

Differential Equation (DE) model

The Differential Equation model (Farkas, 1999) of collector (Fig. 2) represents a more complex approach in comparison to the H-V model.

The governing equations of the model can be described as:

$$\rho \cdot c \cdot V \frac{dT_{co}}{d\tau} = I(\tau) \cdot w \cdot l \cdot \eta_{opt} - \kappa \cdot w \cdot l$$

$$(T_{avg}(\tau) - T_w(\tau)) + \frac{dm}{d\tau} \cdot c(T_{ci}(\tau) - T_{co}(\tau))$$
(2)

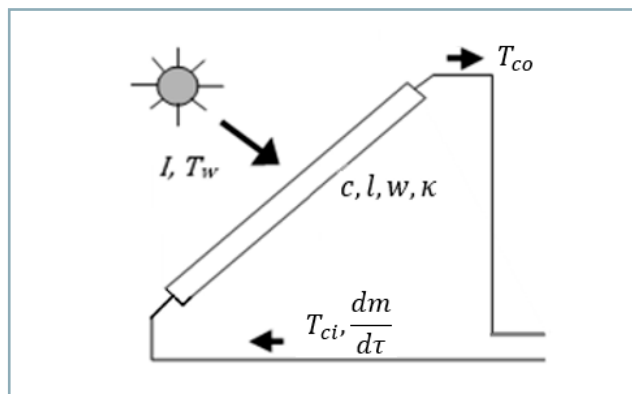


Fig. 1 Scheme of the collector

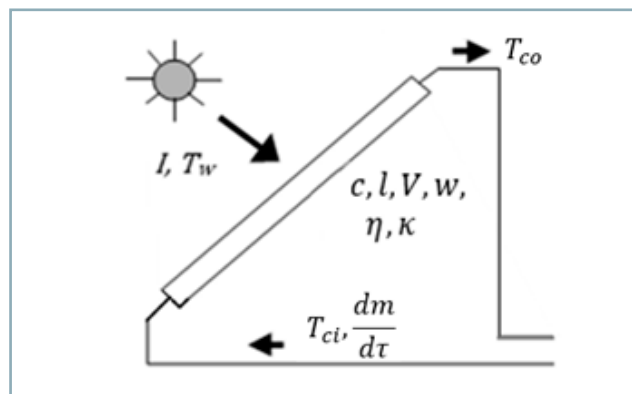


Fig. 2 Scheme of the collector

where the average temperature of the collector:

$$T_{avg}(\tau) = \frac{T_{ci}(\tau) + T_{co}(\tau)}{2}$$
(3)

where:

- ρ – density of the working fluid ($kg \cdot m^{-3}$)
- c – specific heat of the working fluid ($J \cdot kg^{-1} \cdot K^{-1}$)
- V – volume of the working fluid (m^3)
- T_{co} – collector outlet temperature (°C)
- τ – time (s)
- I – solar radiation ($W \cdot m^{-2}$)
- w – width of the collector (m)
- l – length of the collector (m)
- η_{opt} – optical efficiency (m^{-3})
- κ – overall heat transfer coefficient of the collector ($W \cdot m^{-2} \cdot K^{-1}$)
- T_{avg} – average temperature (°C)
- T_w – ambient temperature (°C)
- m – mass of the working fluid (kg)
- T_{ci} – collector inlet temperature (°C)

The parameters η_{opt} and κ cannot be measured easily, so they are needed to be identified via measurements.

Models of heat storages

Heat storage plays an important role in a solar thermal system, because the time of the energy collection frequently differs from the time of the consumption of this energy, this thermal energy needs to be stored. The heat storage uses fluid to store the heat energy; this fluid was water in case of the simulations. Two different types of heat storage devices were selected, because these two are the most commonly used in small-scale household solar thermal systems. The two mathematical models of the storage are discussed in this section.

Mixed heat storage

Considering the mixed heat storage, the outlet of the collector and the inlet of the storage meet in a common space, this is where the transfer of the energy occurs; therefore, the temperatures of the storage outlet and the collector inlet are the same.

This model of the storage can be seen in the literature (Duffie and Beckman, 2013) as shown in Fig. 3.

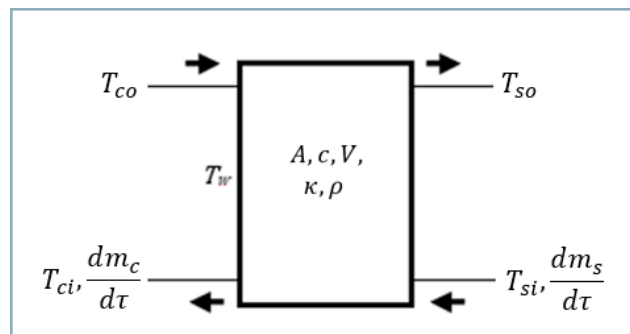


Fig. 3 Scheme of the storage

The construction yields that $T_{so} \equiv T_{ci}$, this temperature will be denoted as T_s . The mathematical model is as follows:

$$c_s \cdot V_s \cdot \rho_s \cdot \frac{dT_s}{d\tau} = c_c \frac{dm_c}{d\tau} (T_s(\tau) - T_w(\tau)) - c_s \frac{dm_s}{d\tau} (T_s(\tau) - T_{si}(\tau)) - \kappa_s \cdot A_s (T_s(\tau) - T_w(\tau)) \quad (4)$$

where:

- c_s – specific heat of the working fluid in the storage ($J \cdot kg^{-1} \cdot K^{-1}$)
- V_s – volume of the storage (m^3)
- ρ_s – density of the working fluid in the storage ($kg \cdot m^{-3}$)
- T_s – storage temperature ($^{\circ}C$)
- T_w – ambient temperature ($^{\circ}C$)
- τ – time (s)
- c_c – specific heat of the working fluid in the collector ($J \cdot kg^{-1} \cdot K^{-1}$)
- m_c – mass of the working fluid in the collector (kg)
- m_s – mass of the working fluid in the storage (kg)
- T_{si} – storage inlet temperature ($^{\circ}C$)
- κ_s – overall heat transfer coefficient of the storage ($W \cdot m^{-2} \cdot K^{-1}$)
- A_s – surface of the storage (m^2)

Heat storage with heat exchanger

In this type of heat storage, the fluid of collector-loop passes through the fluid of the storage in a heat exchanger pipe. There is no physical contact between the two fluids, but there is less useful surface for the heat transfer in contrast to the mixed heat storage.

This type of heat storage is a more complex device; this is also reflected in the mathematical model. The model was applied to a storage shown in Fig. 4.

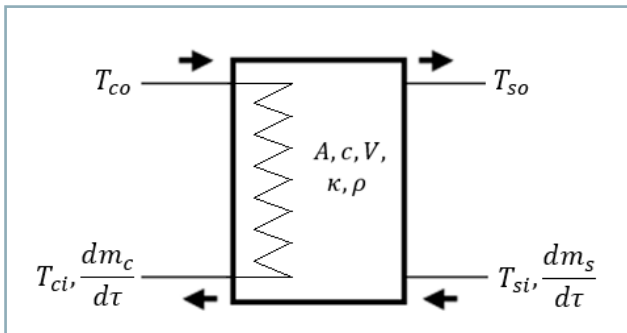


Fig. 4 Scheme of the storage

The mathematical model of the heat storage (Farkas, 1999) is as follows:

$$T_{ci}(\tau) = (T_{co}(\tau) - T_{so}(\tau)) \cdot \exp\left(\frac{-\kappa_s \cdot A_s}{c_s \cdot \frac{dm_s}{d\tau}}\right) + T_{so}(\tau) \quad (5a)$$

$$c_s \cdot V_s \cdot \rho_s \cdot \frac{dT_{so}}{d\tau} = c_s \frac{dm_s}{d\tau} (T_{si}(\tau) - T_{so}(\tau)) + c_c \frac{dm_c}{d\tau} (T_{co}(\tau) - T_{ci}(\tau)) \quad (5b)$$

where:

- τ – time (s)
- T_{ci} – collector inlet temperature ($^{\circ}C$)
- T_{co} – collector outlet temperature ($^{\circ}C$)
- T_{so} – storage outlet temperature ($^{\circ}C$)
- κ_s – overall heat transfer coefficient of the storage ($W \cdot m^{-2} \cdot K^{-1}$)
- A_s – surface of the storage (m^2)
- c_s – specific heat of the working fluid in the storage ($J \cdot kg^{-1} \cdot K^{-1}$)
- m_s – mass of the working fluid in the storage (kg)
- V_s – volume of the storage (m^3)
- ρ_s – density of the working fluid in the storage ($kg \cdot m^{-3}$)
- T_{si} – storage inlet temperature ($^{\circ}C$)
- c_c – specific heat of the working fluid in the collector ($J \cdot kg^{-1} \cdot K^{-1}$)
- m_c – mass of the working fluid in the collector (kg)

Metrics of comparison

For the comparison of the validation of the models, the following metrics were used.

The error (ε) between the measured/studied (T) and the calculated/computed (T') temperature is defined as follows:

$$\varepsilon(\tau) = \int_{\tau_0}^{\tau} (T(t) - T'(t))^2 dt \quad (6)$$

which is similar to the least-squares method. This metric is capable of rating the T' function on the basis of every point of its domain.

The maximal difference (Δ) indicating the maximal deviation is:

$$\Delta = \max(|(T(\tau) - T'(\tau))|) \quad (7)$$

This metric rates the T' function on the basis of one point of its domain.

Results and discussion

Simulation results are discussed in this section, showing the setups of the simulations, resulting figures and the numerical values of the used metrics.

Comparison of the collector models

Simulation setup consists of the two collector models and the measured data. The models have been provided with the same input data and the output temperatures of the models have been compared to the measured outlet temperature. The block-oriented representation of this system can be seen in Fig. 5.

Technical parameters of the H-V collector were:

- collector width: 0.5 m;
- collector length: 1 m;
- specific heat of the working fluid (water): $4,200 J \cdot kg^{-1} \cdot K^{-1}$.

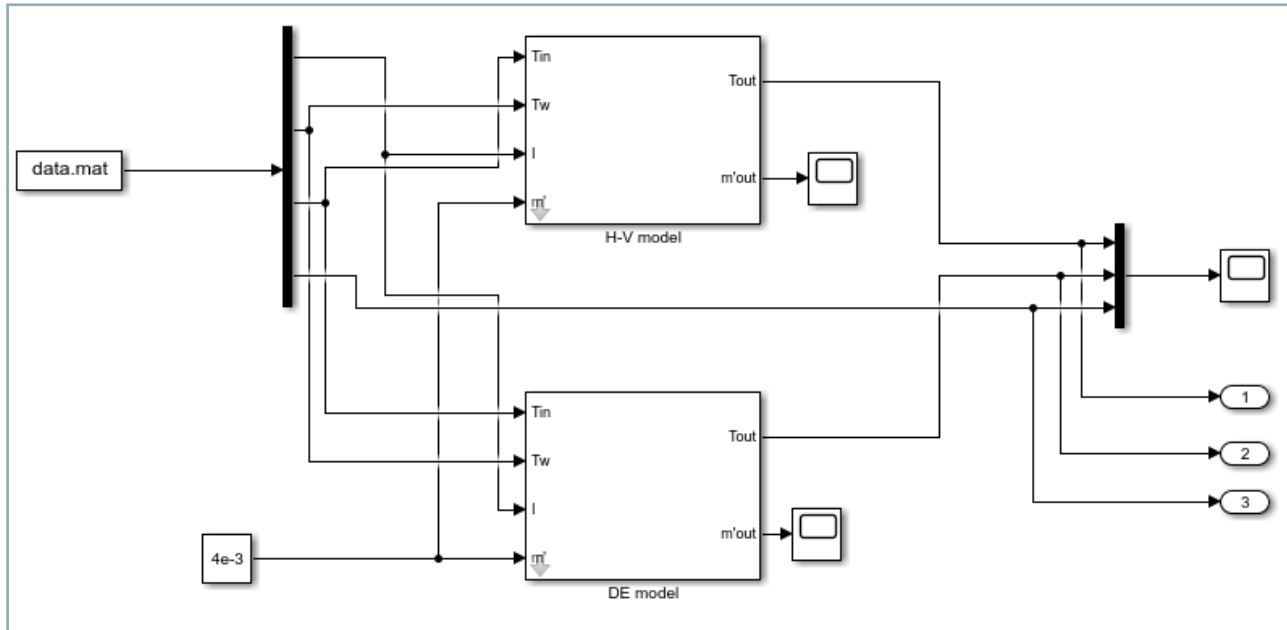


Fig. 5 Block-oriented model for collector comparison

The κ_{aw} and κ_{mw} parameters had to be identified for the collector by means of a measured data set:

- heat transfer coefficient between the absorber and environment: $38.9 \text{ W}\cdot\text{m}^{-2}\cdot\text{K}^{-1}$;
- heat transfer coefficient between the working fluid and environment: $37.6 \text{ W}\cdot\text{m}^{-2}\cdot\text{K}^{-1}$.

Technical parameters of the DE collector were:

- collector width: 0.5 m;
- collector length: 1 m;
- collector volume: 0.0037 m^3 ;
- specific heat of the working fluid (water): $4,200 \text{ J}\cdot\text{kg}^{-1}\cdot\text{K}^{-1}$;
- density of the working fluid (water): $1,000 \text{ kg}\cdot\text{m}^{-3}$;
- initial temperature: $20 \text{ }^\circ\text{C}$.

The η_0 and κ parameters had to be identified for the collector by means of the same data used for the H-V model. Their numerical values are:

- heat transfer coefficient: $33.6 \text{ W}\cdot\text{m}^{-2}\cdot\text{K}^{-1}$;
- optical efficiency: 0.89.

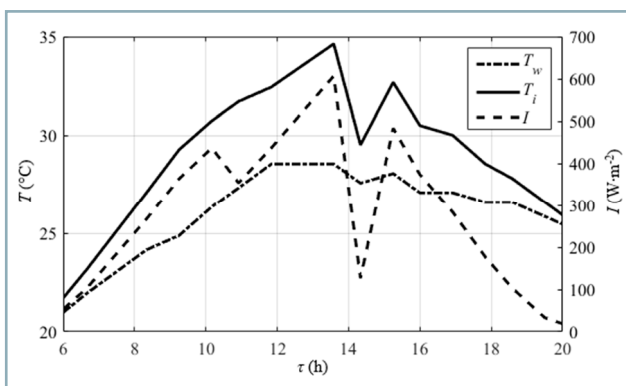


Fig. 6 Inlet, ambient temperature and global radiation

In the present stage of the work, the simulation was carried out by means of measured data including global radiation, inlet and ambient temperature, as shown in Fig. 6.

Collector pump had a constant mass flow of $0.004 \text{ kg}\cdot\text{s}^{-1}$.

Start time of the simulation was 6 AM and the duration of the simulation was 14 h.

Fig. 7 shows the resulting outlet temperatures observed during simulations and Table 1 shows the metrics of the comparison. The H-V model is less accurate than the DE model, but it takes lower amount of parameters into account. The similarity of simulation results was anticipated, since the solution of the DE model has a form similar to the H-V model. The accuracy difference between the two models is in the acceptable rate for further studies. The H-V model is more capable of running on an embedded system, such as a Raspberry Pi, due to its simplicity.

Table 1 Results of the comparison

	H-V model	DE model
$\varepsilon(\tau=72000)$	39,846.63	28,818.62
Δ	2.5246	1.9957

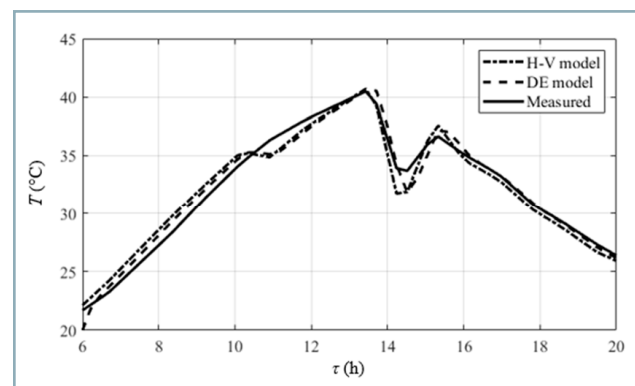


Fig. 7 Outlet temperature of the collectors

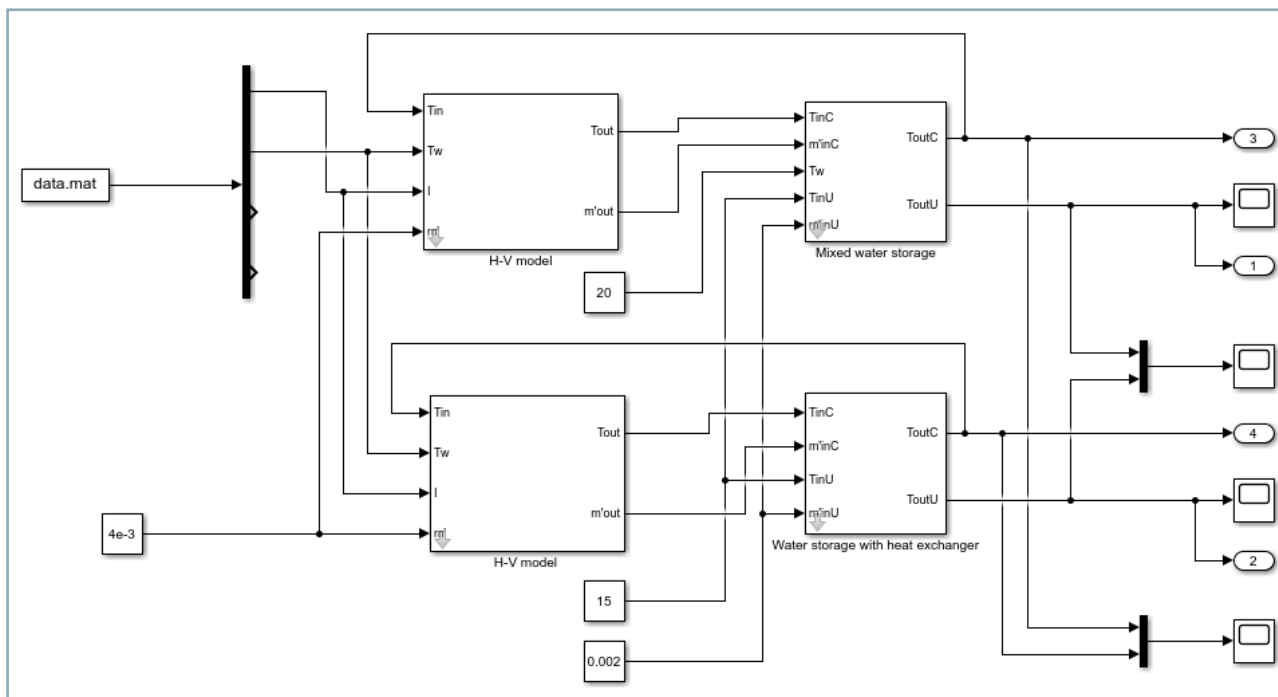


Fig. 8 Block-oriented model for heat storage comparison using H-V model

Table 2 Results of the simulations

	H-Vci	H-Vso	DEci	DEso
$\epsilon(\tau=72000)$	531989.81	531989.81	524906.58	524906.58
Δ	4.86	4.86	4.89	4.89

Simulation of the storage models

Goal of this simulation is to study the previously compared collector models in a system. Each collector model was attached to the two storage models and the outlet temperatures of the storages were compared. The block-oriented model of the simulation with the H-V model is shown in Fig. 8. Considering the DE model, simulation setup was identical with exception of the collector model.

Simulation input data were the same as in the comparison of the collector models (Fig. 6).

Technical parameters of both storages were:

- storage surface: 0.375 m²;
- storage volume: 0.15 m³;
- specific heat of the working fluid (water): 4,200 J·kg⁻¹·K⁻¹;
- density of the working fluid (water): 1,000 kg·m⁻³;
- heat transfer coefficient: 1,200 W·m⁻²·K⁻¹.

The storage models are white-box models, so there was no need for identification.

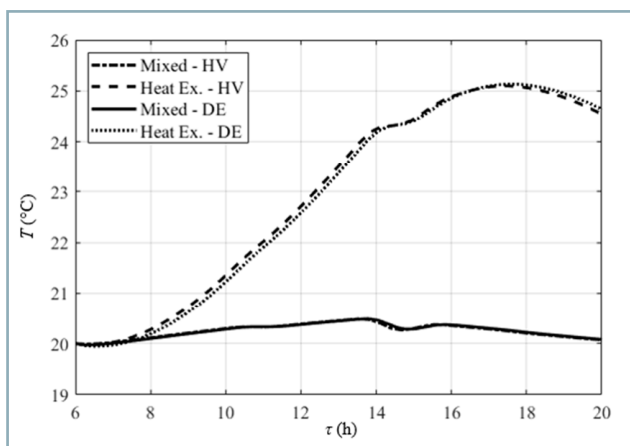


Fig. 9 Collector inlet temperatures of the storages

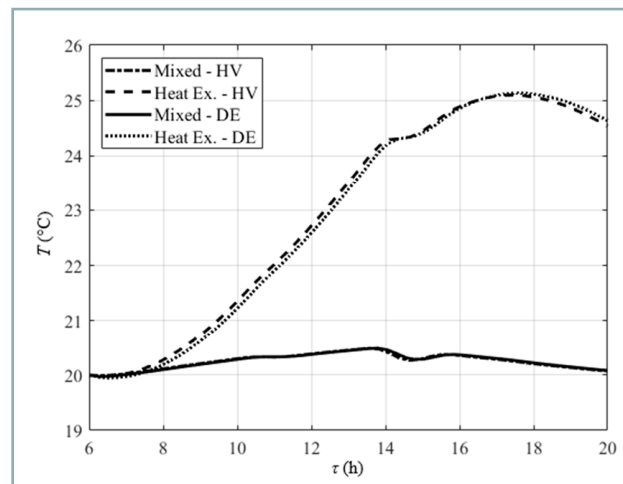


Fig. 10 Storage outlet temperatures of the storages

Collector pump had a constant mass flow of $0.004 \text{ kg}\cdot\text{s}^{-1}$ and the pump of the storages had a constant mass flow of $0.002 \text{ kg}\cdot\text{s}^{-1}$.

The ambient temperature was set to $20 \text{ }^\circ\text{C}$, the user input temperature was $15 \text{ }^\circ\text{C}$ and the initial storage temperature was $20 \text{ }^\circ\text{C}$.

The time of the start of the simulation was 6 AM, the duration of the simulation was 14 h.

Fig. 9 and Fig. 10 show the resulting temperatures observed during the simulation and Table 2 shows the numerical values of the used metrics. The difference in results is basically a slight shift in time, which is in the acceptable range. This simulation shows that the difference in the output between the H-V and the DE models is nearly vanishing if they are used in a system, indicating that the H-V model is feasible for carrying out further studies, the HIL simulation in a physical system.

Conclusion

This paper compares two mathematical models of a solar thermal collector – the H-V model and the DE model. The DE model takes into account higher amount of parameters than the H-V model, yet it is more complex. Model parameters were identified on the basis of measurements. Simulation was performed on the basis of the developed SimSolar block-oriented software. Comparison results showed that the greatest difference in accuracy of the models was $2.52 \text{ }^\circ\text{C}$, which is in the acceptable range for carrying out the simulations using either of the collector models. Furthermore, solar collector models were tested in a system using different models of heat storages. This test showed that the accuracy difference was even lower, almost negligible ($0.03 \text{ }^\circ\text{C}$) if heat exchangers were used in the system.

On the basis of the results, it can be concluded that the H-V model is more suitable for usage in a hardware-in-the-loop simulation for its simplicity. This type of simulation can be achieved using an embedded system, such as Raspberry Pi. Further development can be achieved by the HIL simulation using physical devices.

Acknowledgements

This work was supported by the Mechanical Engineering Doctoral School, Szent István University, Gödöllő, Hungary.

References

- BILČÍK, M. – BOŽIKOVÁ, M. – PETROVIĆ, A. – MALÍNEK, M. – CVIKLOVIČ, V. – OLEJÁR, M. – ARDONOVÁ, V. 2018. Analysis of selected photovoltaic panels operating parameters as a function of partial shading and intensity of reflected radiation. In *Acta Technologica Agriculturae*, vol. 21, no. 1, pp. 14–17.
- DUFFIE, J. A. – BECKMAN, W. A. 2013. *Solar Engineering of Thermal Processes*. New York: John Wiley & Sons, Inc., pp. 386–387. ISBN 978-0-470-87366-3.
- FARKAS, I. 1999. *Computer Simulation*. Gödöllő: University of Agriculture, p. 45.
- ILYAS, A. – AYYUB, M. – KHAN, M. R. – JAIN, A. – HUSAIN, M. 2018. Realisation of incremental conductance the MPPT algorithm for a solar photovoltaic system. In *International Journal of Ambient Energy*, vol. 39, no. 8, pp. 873–884.
- KYN, M. – URBAN, M. 2013. TRNSYS software model of solar system with long-term storage. In *Advanced Materials Research*, vol. 649, pp. 303–306.
- LACOSTE, B. – WOLF, A. – WITZIG, A. – MARKLIN, A. 2010. Polysun: PV, wind and power-heat cogeneration in one design tool. In *Proceedings of the 5th European PV-Hybrid and Mini-Grid Conference, 2010, April 29–30, Tarragona, Spain*, Ostbayerisches Technologie-Transfer-Institut e.V., pp. 1–8. ISBN 978-3-941785-15-1.
- PATERNO, F. 2000. *Model-based design and evaluation of interactive applications*. London: Springer-Verlag London. ISBN 978-1-85233-155-9.
- TÓTH, J. – FARKAS, I. 2017. Developing a Simulink library for solar energy applications. In *R&D in Mechanical Engineering Letters*, vol. 16, pp. 89–95.
- TRNSYS Manual. 2009. vol 1. <http://web.mit.edu/parmstr/Public/Documentation/01-GettingStarted.pdf>
- VELASQUEZ, D. R. – COLLAZOS, V. T. – MINES, J. M. 2017. A low-cost hardware-in-the-loop real time simulation of control systems. In *Proceedings of the 2017 IEEE 24th International Congress on Electronics, Electrical Engineering and Computing, INTERCON 2017, 2017, August 15–18, Cusco, Peru*, Curran Associates, Inc. ISBN 978-150906362-8.



Acta Technologica Agriculturae 4
Nitra, Slovaca Universitas Agriculturae Nitriae, 2019, pp. 134–139

THE POSSIBILITIES OF USING ECOLOGICAL LIQUIDS IN TRIBOLOGICAL GLIDING SYSTEMS WITH A SELECTED SURFACE CREATED BY THE RADIAL WELDING TECHNOLOGY

František TÓTH^{1*}, Adam FÜRSTENZELLER¹, Juraj RUSNÁK¹, Miroslav BOŠANSKÝ², Milan KADNÁR¹

¹Slovak University of Agriculture in Nitra, Slovak Republic

²Slovak University of Technology in Bratislava, Institute of Transport Technology and Designing, Slovak Republic

Presented paper deals with the issue of lubricating tribological systems formed by a double pair operating under mixed conditions of mixed friction before and after experimental tests, which were conducted in accordance with the selected methodology using Tribotestor M'06 test machine. The lubricating media included ecological oils Plantohyd 46 S by Fuchs and EAL Hydraulic 46 manufactured by the Mobil company. Applied ecological oils can be used in agricultural mobile machines as a replacement for conventional lubricants. The tests were conducted on designated material double pairs. The shaft was made of steel 16MnCr5. The second observed friction element in terms of glide angle test was a steel plate made of S235JR, gliding surface of which was produced utilizing flame powder coating technology. The results were statistically processed and are presented in the form of graphs, tables and figures.

Keywords: glide angle; flame powder welding; ecological oil; mixed friction; Tribotestor M'06

Agricultural engineering requires a constant improvement of operating life and reliability of machinery along with the possibility of using ecological oils. One option is to introduce new surface treatment technologies. This opens up a space for development and application of new unconventional surface treatment technologies with non-traditional additives and their specific properties (Bujna et al., 2016; Tillmann et al., 2017). Such technologies include radial welding technology.

Our current direction in this research field lies in analysis of the selected tribological properties of the material double pair, where one of the surfaces is modified by the radial welding technology. Biodegradable oil was selected as a lubricating medium for the gliding tribological system. Selection of biodegradable oils was performed on the basis of the experiments carried out under both laboratory and real conditions (Majdan et al., 2010; Kosiba et al., 2013; Stojilković and Kolb, 2016; Birkavs and Smigins, 2018; Kučera and Aleš, 2017).

Experimental device consists of three main parts: the test part includes propulsion units for the rotational movement of the samples, vertical load force and measuring head; the second part includes a pneumatic circuit and all electronic devices; the last part is a control and evaluation unit in the form of a desktop computer allowing the triggering, controlling, managing, data collecting and evaluation of the test itself (Bijelića et al., 2017).

Experiment presented was carried out via the seizing test.

Material and methods

Tribotestor M'06 (Fig. 1) was used for conducting the tribological experimental tests. This universal testing device enables the following types of tests to be carried out: limit load test (seizing test), limit speed test (speed seizing test), load capacity test (PV diagram determination), and durability test (longevity).



Fig. 1 Measuring device Tribotestor M'06

Contact address: František Tóth, Slovak University of Agriculture in Nitra, Faculty of Engineering, Department of Machine Design, Tr. Andreja Hlinku 2, 949 76 Nitra, Slovak Republic, e-mail: frantisek.toth@uniag.sk

The gliding system comprises four components (Stachowiak and Batchelor, 2014). The gliding double pair consists of a shaft and a gliding plate. The third element is a lubricating medium (ecological oil in this case). The fourth component is the surrounding environment. Atmosphere influence on the experiment was ignored because of relatively short duration of the experimental test. The first friction element was test shaft housing with 28 mm outer diameter and a length of 25 mm, made of 16MnCr5 steel and pressed onto the cylindrical part of the support shaft (Bhushan, 2001). The support shaft was attached to a drive unit by means of a conical coupling via a tightening force through the internal thread in the conus. The second friction element was a steel plate made of S235JR in accordance with the STN EN 10027-1, with dimensions of 20 × 20 × 5 mm as the supporting material onto which the test glide surface was applied. It was made of NP 40, which is a NiBCrSi-based powder alloy (Chotěborský et al., 2013; Kučera and Chotěborský, 2013). The NP40 powder was applied to the surface of the plate via the flame powder welding technology. Welding process was carried out at the Department of Quality and Engineering Technologies of the Faculty of Engineering, Slovak University of Agriculture in Nitra. In general, the aforementioned powder is intended to weld the surfaces of steel components exposed to abrasive,

corrosive and thermal stresses. Such layers can be machined by turning and grinding. For experiment presented, a gliding material was designed on the basis of results obtained by Tóth et al. (2014) and Kopiláková et al. (2017). The chemical composition and mechanical properties are shown in Table 1. Lubrication of the gliding elements and ecological oil test were performed by means of dipping; the oil was applied at the beginning of the experiment (Mang and Dresel, 2017).

Both gliding elements were weighed before and after the experiments utilizing the Voyager Pro VP 613CN precision scales and their roughness was measured by the Mitutoyo SJ-201 roughness meter. The monitored parameter was R_{ar} ; its value represents the average arithmetic value of the absolute profile deviations at n selected points of the profile at the base length. Using a Spectro analytical ferrograph (model T2FM), ferrograms were plotted for both double pairs. Their evaluation was performed utilizing the Carl Zeiss Axio Scope series microscope with a 1,000 times magnification.

Tested ecological product was Plantohyd 46 S by Fuchs; this product is an environmentally friendly, rapidly biodegradable, non-polluting hydraulic fluid based on synthetic esters of the HEES type according to the VDMA 24 568 standard.

Plantohyd 46 S is compatible with materials commonly used in

hydraulic systems. The base fluid and the additives used are toxicologically harmless. Fluid does not contain heavy metals and chlorine compounds; it is biodegradable up to more than 90% according to CEC-L-33-A-93.

This product can be used at temperatures ranging from -30 °C to max. 90 °C. If the system temperature peaks at max. 95 °C, it is still acceptable in respect to the limit viscosity.

Plantohyd 46 S is versatile oil for use in all hydraulic and circulating systems requiring the use of ISO VG 46 oil. This product is suitable for mobile and stationary hydraulic systems. It is mainly used in devices operating in environments with a risk of leakage of hydraulic fluids that can endanger the ground, groundwater or surface water. If an oil leak occurs, this product will be mainly caught in the upper layers of soil, where it is rapidly biodegraded. Specific applications are mainly in construction, water management, agriculture and forestry.

The second used ecological liquid was the lubricant manufactured by Exxon Mobil under the trade designation EAL Hydraulic 46.

Mobil EAL Hydraulic 46 is hydraulic oil designed to meet the requirements of environmentally friendly hydraulic fluids. It is based on synthetic esters that are easily biodegradable. The additive complex provides environmental protection against wear and tear, high pressure, corrosion and ensures thermal stability. The resistance to oxidation helps prevent oil thickening and sediment formation even at high temperatures. This product can be used at temperature range from -17 °C to max. 93 °C.

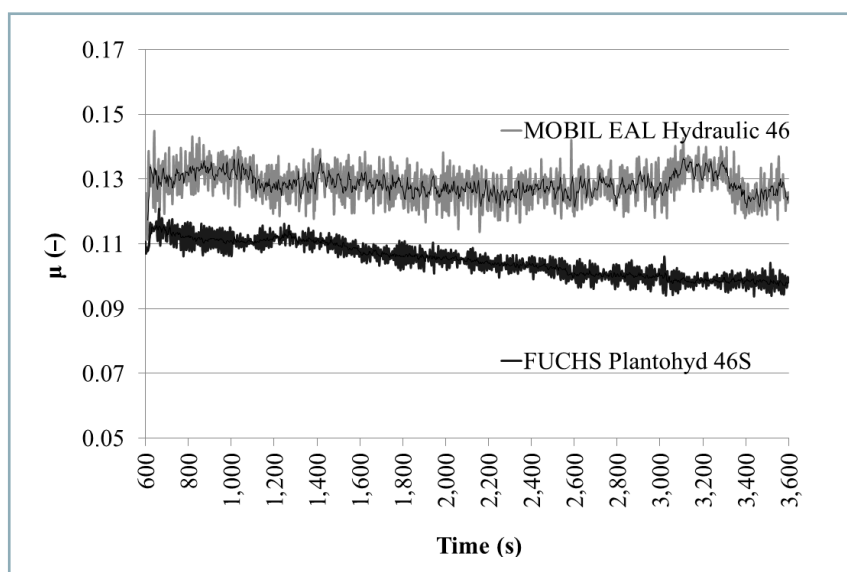
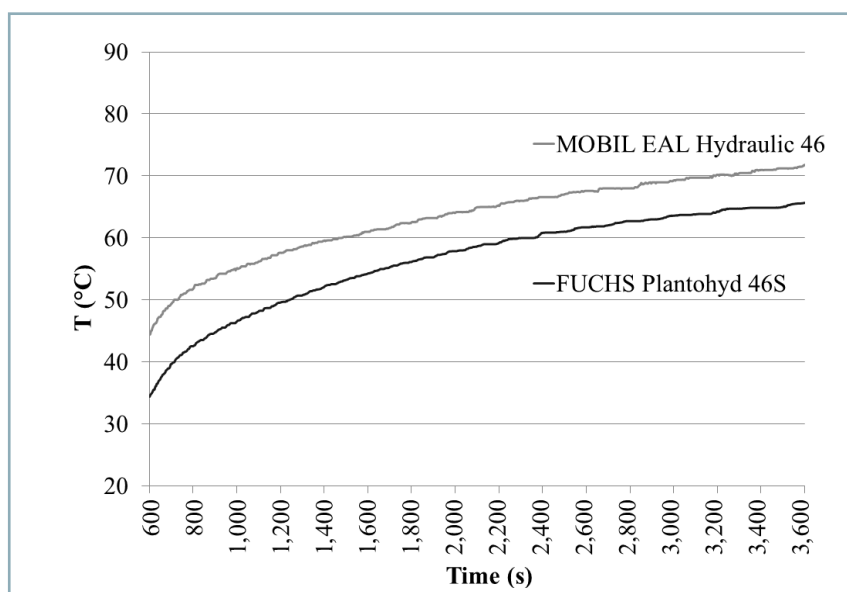
Mobil EAL Hydraulic 46 oil provides performance over a wide temperature range; its wear resistance, lubricating capabilities and lubricating film strength ensure adequate performance in hydraulic and circulating systems operating in mild and demanding operating conditions. Easy biodegradability and virtually non-toxic nature of this product allows usage in locations where leakage can have a negative impact on the environment. It is used in industry, forestry, water transport, and especially in mobile machinery.

Table 1 Chemical composition and mechanical properties of the NP 40 test plate

Material	NP 40	
Chemical composition (%)	Ni	rest
	Si	3.5–4.5
	B	1.5–2.5
	Cr	1.5–2.5
	Cu	max. 0.3
	Fe	max. 0.5
	C	max. 0.1
Physical properties	bulk density	4.8 g·cm ⁻³
Granulometric composition (%)	fraction > 0.100 mm	max. 10
	fraction 0.100 mm	max. 90
	fraction 0.063 mm	
	fraction <0.063 mm	

Table 2 Physical and chemical properties of used ecological lubricants

	Fuchs Plantohyd 46 S	Mobil EAL Hydraulic 46
Class ISO-VG	46	46
Viscosity index	192	149
Viscosity at 40 °C (mm ² ·s ⁻¹)	47.5	43.3
Viscosity at 100 °C (mm ² ·s ⁻¹)	9.6	7.7
Density at 15 °C (kg·m ⁻³)	922	930
Pour point (°C)	-39	-33
Flash point (°C)	290	298

**Fig. 2** Course of friction factors for ecological oils as a function of time**Fig. 3** Course of temperature for ecological oils as a function of time

During the experimental tests, the shaft speed was 180 rpm in the clockwise direction. The test time was set to 3,600 seconds, with a 600 seconds start-up time and an hourly individual test. The load force was selected in the range from 500 to 3,000 N. The start-up load was represented by an increment in the load force by increasing its value by 500 N every 120 seconds.

Results and discussion

Recorded results of laboratory measurements utilizing the Tribotestor M 06 experimental apparatus were statistically processed, and the dependences of friction and temperature coefficients on time, weight loss, roughness changes, and the elements contained in the lubricant medium were evaluated after test completion.

By statistical adjustment of the values recorded during the course of experimental tests, an overview of the development of the friction coefficients of two investigated ecological lubricants as a function of time was obtained. Fig. 2 illustrates the aforementioned stresses at a constant load force; the start-up time was not taken into consideration. It is obvious that the dependence of the friction factors on time is different for both investigated oils. Fuchs Plantohyd 46 S ecological oil shows a more balanced, decreasing curve from the initial value of 0.11 to 0.098 at the end of tests. Considering the Mobil EAL Hydraulic 46 ecological oil, there is a clear imbalance in the individual experimental tests, which is reflected in the larger scattering of the friction coefficient curve. The initial value of the friction coefficient is 0.13 during the experimental test and it merely slightly decreases to the final value of 0.125. Both ecological oils are sensitive to the change in load what can actually be observed after reaching the final load value.

Temperature-dependent time course shown in Fig. 3 has the same character for both ecological oils. Mobil EAL Hydraulic 46 ecological oil showed a higher initial temperature of 44 °C, as well as a higher final temperature of 71.5 °C. The initial value of the Fuchs Plantohyd 46 S

Table 3 Values of average weight loss

Weight loss (g)							
Lubricants	Number of experimental test	Plate			Shaft		
		before experiment	after experiment	difference	before experiment	after experiment	difference
Fuchs Plantohyd 46S	1	20.924	20.929	-0.005	405.249	405.245	0.004
	2	19.652	19.655	-0.003	398.810	398.798	0.012
	3	22.305	22.309	-0.004	392.630	392.616	0.014
	4	21.676	21.679	-0.003	399.053	399.044	0.009
	5	22.836	22.841	-0.005	405.817	405.804	0.013
	6	19.952	19.949	0.003	395.862	395.854	0.008
	7	18.766	18.768	-0.002	398.593	398.590	0.003
	8	20.661	20.665	-0.004	402.736	402.730	0.006
Average				-0.003			0.009
Lubricants	Number of experimental test	Plate			Shaft		
		before experiment	after experiment	difference	before experiment	after experiment	difference
Mobil EAL Hydraulic 46	1	20.356	20.354	0.002	404.927	404.921	0.006
	2	19.770	19.768	0.002	407.332	407.321	0.011
	3	19.298	19.296	0.002	397.844	397.839	0.005
	4	19.039	19.040	-0.001	401.636	401.627	0.009
	5	20.752	20.751	0.001	410.088	410.080	0.008
	6	19.567	19.568	-0.001	399.780	399.770	0.010
	7	20.156	20.155	0.001	399.075	399.067	0.008
	8	19.958	19.957	0.001	411.446	411.437	0.009
Average				0.001			0.008

ecological oil temperature was approx. 34 °C and increased during the experiment to a final value of 65.5 °C. None of samples reached the maximum temperature allowed by the manufacturer during the experimental tests.

Voyager precision scales for VP 613CN illustrated the weight loss of the two gliding elements. Considering the material pair NP 40 – 16MnCr5, a specific phenomenon has arisen, when in the absolute value, the wear of the plate equals zero and potential plate weight increase results from either sticking, or welding of mechanical parts present in the lubricating environment due to the shaft adhesion wear. A similar phenomenon was observed in the previous experimental measurements performed at the workplace. The weight losses on the shafts for both used ecological oils were almost identical.

The roughness of the plate and the shaft were determined using dredger Mitutoyo SJ-201 roughness meter. The average change in roughness R_a represents the change in surface roughness of the gliding element over the duration of experimental test. Considering the interaction of both ecological oils with the material pair 16MnCr5 – NP 40, the shaft got smoother during the test, which was reflected by a decrease in the R_a value of the 16MnCr5 and an increase in the R_a value of the NP 40 composite plate. This phenomenon

occurs due to either sticking, or welding of shaft mechanical parts to the composite plate. This phenomenon was confirmed by the weight loss analysis. The average drop in the roughness value of R_a of the shaft was 0.371 μm in case of the Plantohyd 46 S oil and 0.347 μm in case of the EAL Hydraulic 46 oil. The increase in the average roughness value of R_a of the plates was almost equal to 0.271 μm (Plantohyd 46 S) in comparison to 0.276 μm (EAL Hydraulic 46).

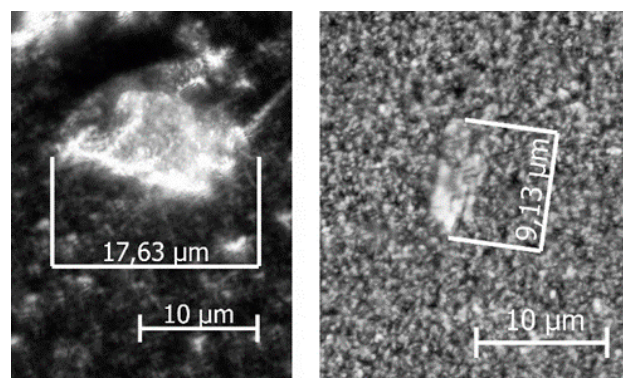


Fig. 4 Evaluation of ferrography of the ecological oil Fuchs Plantohyd 46 S (1,000 times magnification)

Table 4 Average changes in R_a roughness values

Lubricants	Number of experimental test	' R_a ' change (μm)					
		Plate			Shaft		
		before experiment	after experiment	change	before experiment	after experiment	change
Fuchs Plantohyd 46S	1	0.355	0.660	0.305	0.815	0.620	-0.195
	2	0.340	0.520	0.180	1.025	0.685	-0.340
	3	0.190	0.545	0.355	0.960	0.600	-0.360
	4	0.220	0.490	0.270	0.935	0.565	-0.370
	5	0.175	0.490	0.315	1.220	0.760	-0.460
	6	0.300	0.285	-0.015	1.190	0.835	-0.355
	7	0.350	0.660	0.310	1.070	0.675	-0.395
	8	0.260	0.710	0.450	1.175	0.680	-0.495
Average				0.271			-0.371
Lubricants	Number of experimental test	Plate			Shaft		
Mobil EAL Hydraulic 46	1	0.350	0.650	0.300	0.920	0.550	-0.370
	2	0.300	0.490	0.190	0.850	0.450	-0.400
	3	0.480	0.980	0.500	0.990	0.600	-0.390
	4	0.260	0.360	0.100	0.760	0.570	-0.190
	5	0.580	0.870	0.290	0.850	0.395	-0.455
	6	0.330	0.580	0.250	0.790	0.450	-0.340
	7	0.410	0.780	0.370	0.690	0.510	-0.180
	8	0.390	0.595	0.205	1.080	0.630	-0.450
Average				0.276			-0.347

The ferrography of the ecological oil Plantohyd 46 S is given in Fig. 4; left figure shows well visible iron particles found at the start of the ferrography. On the basis of their size and comparison with the sample of non-ferrous particles, this wear was characterized at the upper limit of adhesive wear with $17.63 \mu\text{m}$ in size. Right figure (Fig. 4) shows a non-ferrous, non-ferrite particle with a size of $9.13 \mu\text{m}$.

Fig. 5 presents the ferrography analysis of the ecological oil EAL Hydraulic 46. Left figure depicts a $19.35 \mu\text{m}$ iron particle that defines the borderline adhesive wear. The

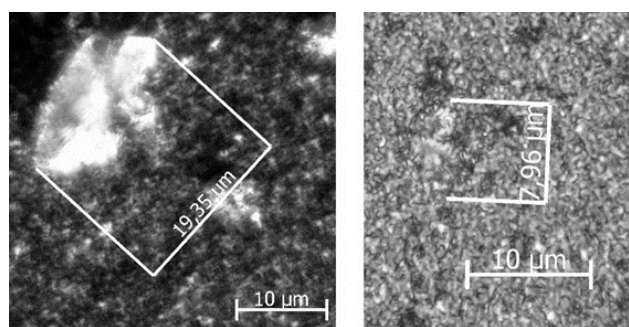


Fig. 5 Evaluation of ferrography of the ecological oil Mobil EAL Hydraulic 46 (1,000 times magnification)

particle in question is likely chrome captured in the top of the ferrography. Right figure (Fig. 5) illustrates the lower part of the ferrography, showing the non-ferrous particle resulting from adhesive wear with approximately $8 \mu\text{m}$ in size.

As far as both ecological oils are concerned, particles have a lamellar shape indicating their multiple passages through the contact surface of the friction elements.

Conclusion

Presented scientific paper analyses the effect of selected ecological oils on the tribological system consisting of a gliding double pair during an experiment conducted on the basis of the proposed methodology. Comparison of the dependence development of the friction coefficients of ecological oils on time proved that Fuchs Plantohyd 46 S shows more appropriate and balanced course. The ecological oil temperature dependence showed a very similar profile with a lower oil temperature of Fuchs Plantohyd 46 S. Neither of investigated oils reached the maximum temperature limiting its use during the experiment. Specific phenomenon in weight loss arose – in the absolute value, the wear of the plate equals zero and potential plate weight increase results from the sticking or welding of mechanical parts present in

the lubricating environment due to the shaft adhesion wear. The wear of the shafts was approximately the same for both investigated oils. The results obtained reflect the conditions of the experiment itself when the gliding pair works in a lubricating bath without the possibility of oil filtration. Another indicator taken into account was the change in roughness of investigated surfaces. The roughness was evaluated through the R_a characteristic, which was measured before and after the experiment on the contact surfaces of the gliding elements. Considering both ecological oils, the shaft got smoother during the test, which was reflected by a decrease in the R_a value and an increase in the R_q value in relation to the NP40 composite plate. In this respect, the Mobil EAL Hydraulic 46 ecological oil showed better results. Previous values were also confirmed by the ferrography of the gliding pairs in question. Thereby it was proved that these ecological oils are fully usable under real operating conditions (when oil cooling and filtration are ensured) and utilization of the NP 40 composite material does not represent an obstacle (Kučera and Tkáč, 2010; Kučera et al., 2016; Kosiba et al., 2016).

Acknowledgements

The contribution has been prepared within the solving of scientific grant project VEGA 1/0227/15 Study of tribological characteristics of the new high hard coatings on materials suitable for gearings.

References

- BHUSHAN, B. 2001. Modern Handbook of Tribology. Boca Raton : CRC Press, 1760 pp. ISBN 0-8493-8403-6.
- BIJELIĆA, I. – MOR, N. – ŽIVKOVIĆ, M. – TUBIN, V. – STOŽINIĆ, T. 2017. The influence of the contact pressure on the value of the coefficient of friction. In Tribology in Industry, vol. 39, no. 2, pp. 255–259.
- BIRKAVS, A. – SMIGINS, R. 2018. Experimental research on compatibility of mineral and biobased hydraulic oils. In Agronomy Research, vol. 16, no. S1, pp. 968–976.
- BUJNA, M. – PRÍSTAVKA, M. – DOSTÁL, P. – KORENKO, M. – KADNÁR M. 2016. Influence of roughness on quality molybdenum deposit layer by thermal spraying. In Acta Universitatis Agriculturae et Silviculturae Mendelianae Brunensis, vol. 64, no. 1, pp. 9–14.
- CHOTĚBORSKÝ, R. – KUČERA, M. – HERÁK, D. 2013. Effect of the welding parameters on the hardfacing abrasive wear. In Scientia Agriculturae Bohemica, vol. 44, no. 4, pp. 232–236.
- KOPIĽÁKOVÁ, B. – TURZA, J. – HUJO, Ľ. – KOSIBA, J. 2017. Evaluation of hydraulic resistance in various liquids and temperature. In Tribology in Industry, vol. 39, no. 1, pp. 129–135.
- KOSIBA, J. – ČORNÁK, Š. – GLOS, J. – JABLONICKÝ, J. – VOZÁROVÁ, V. – PETROVIČ, A. – CSILLAG, J. 2016. Monitoring oil degradation during operating tests. In Agronomy Research, vol. 14, no. 5, pp. 1626–1634.
- KOSIBA, J. – HUJO, Ľ. – TULÍK, J. – RAŠO, M. 2013. Study of the impact of synthetic fluid on the lifetime of hydraulic pump. In Advanced Materials Research, vol. 801, pp. 7–12.
- KUČERA, M. – ALEŠ, Z. 2017. Morphology analysis of friction particles generated in tractor transmission oils. In Acta Technologica Agriculturae, vol. 20, no. 3, pp. 57–62.
- KUČERA, M. – CHOTĚBORSKÝ, R. 2013. Analysis of the process of abrasive wear under experimental conditions. In Scientia Agriculturae Bohemica, vol. 44, no. 2, pp. 102–106.
- KUČERA, M. – ALEŠ, Z. – PAVLŮ, J. – HNILICOVÁ, M. 2016. Applying of automatic laser particle counter as technique to morphology assessment and distribution of wear particles during lifetime of transmission oils. In Key Engineering Materials, vol. 669, pp. 417–425.
- KUČERA, M. – TKÁČ, Z. 2010. Analysis of biodegradable oil on synthetic basis in a variable displacement axial piston pump of swash plate. In Acta Facultatis Technicae, vol. 15, no. 1, pp. 81–88.
- MAJDAN, R. – TKÁČ, Z. – TULÍK, J. – KOSIBA, J. – ZIGIŇ, P. – BUREŠ, L. 2010. Evaluation of ecological hydraulic fluid tests based on the flow efficiency of the hydrogenator. In Acta Technologica Agriculturae, vol. 13, no. 3, pp. 61–64.
- MANG, T. – DRESEL, W. 2017. Lubricants and Lubrication. Weinheim : WILEY-VCH Verlag GmbH & Co. KGaA, 1262 pp. ISBN 3-540-41909-8.
- STACHOWIAK, G. – BATCHELOR, A. 2014. Engineering Tribology. Oxford : Butterworth-Heinemann, 884 pp. ISBN 0-7506-7836-4.
- STOJILKOVIĆ, M. – KOLB, M. 2016. Tribological properties of biodegradable universal tractor transmission oil. In Tribology in Industry, vol. 38, no. 2, pp. 229–234.
- STN EN 10027-1. 2018. Designation systems for steels. Part 1: Steel names.
- TILLMANN, W. – HAGEN, L. – KOKALJ, D. 2017. Spray characteristics and tribo-mechanical properties of high-velocity arc-sprayed WC-W2C iron-based coatings. In Journal of Thermal Spray Technology, vol. 26, no. 7, pp. 1685–1700.
- TÓTH, F. – RUSNÁK, J. – BELOEV, H. I. – KADNÁR, M. – PÁLEŠ, D. 2014. The study of geometrical changes of a given sliding couple caused by the influence of operation. Ruse : Angel Kanchev University of Ruse, 82 pp. ISBN 978-954-712-628-2.



Acta Technologica Agriculturae 4
Nitra, Slovaca Universitas Agriculturae Nitriae, 2019, pp. 140–145

FEASIBILITY STUDY OF IMPROVING THE TRANSPORT PERFORMANCE BY MEANS OF SCREW CONVEYORS WITH ROTARY CASINGS

Roman ROHATYNSKYI, Ivan GEVKO, Andrii DIACHUN, Oleg LYASHUK*,
Olena SKYBA, Andrii MELNYCHUK

Ternopil Ivan Puluj National Technical University, Ukraine

Paper presents feasibility study for verification of the hypothesis of improving the productivity of reload operations using screw conveyors with rotary casings. For this purpose, an experimental installation was developed and experimental studies were conducted. Research results fully confirmed the hypothesis. On the basis of a feasibility study of casing rotation in screw conveyors, the conveyor performance increased by 24%, with the conveyor capacity thereby increased by 4.5%. Due to the application of rational parameters of the screw conveyor with a rotary casing, overall economic factor was improved by more than 10%. To achieve the economic efficiency of reload operations using screw conveyors with rotary casings, the rotational frequency of the casing should range from 460 to 620 rpm.

Keywords: screw conveyor; rotary casing; productivity; feasibility study

Screw conveyors are widely used in agriculture as conveyors, mixers, feeders, separators, etc. An increase in performance of screw conveyors often causes considerable unjustified energy consumption that makes the process inefficient. Due to this reason, modern screw conveyors with transporting casings should be designed. Such devices will ensure the shift of the material in order to provide the necessary friction of a screw with the material and casing. Therefore, the efficiency of transport operations will be increased.

Fundamentals of the designing and the investigation of screw conveyers have been presented by Owen and Cleary (2010) or Rogatynskiy et al. (2017), etc. Furthermore, it has been determined that flow uniformity depends on the design of a screw operating element and a hopper, as well as shape of particles and force of their friction at the walls (Hou et al., 2014). Results of this investigation contribute to the insight into the use of a screw conveyer for specific materials.

Multiple authors (Pezo et al., 2015; Hui and Wanfu, 2013; Rogatynskiy et al., 2017) have dealt with the operation mode of an inclined screw conveyer with a screw operating element and constant parameters incorporated in it. Kinematics of grain loading has been investigated on the basis of motion equations in a screw conveyer. Analysis of loading movement at constant high-speed mode has been analysed as well.

Numerous researchers (Lyashuk et al., 2015; Fernandez et al., 2011; Sun et al., 2017; Zareiforoush et al., 2010) provide findings on flow patterns of bulk materials depending on constructional and kinematic characteristics of screw operating tools, bunker type and solid particles, as well as frictional forces. Findings of aforementioned researches

show the improvement of characteristics of screw conveyors during transportation of bulk materials. Authors Baranovsky et al. (2018), Hevko et al. (2015) and Hevko et al. (2018a) dedicated their investigations to the solving of aforementioned issues, namely the development of energy-saving designs of screw conveyors and selection of their most efficient parameters and working modes.

Furthermore, researchers Loveikin and Rogatynska (2011) and Lyashuk et al. (2015) have investigated contact interaction of grain-working surfaces and described methods for improvement of operation life of screw conveyors. Their works pay special attention to the selection of parameters of working bodies and processes of materials transportation, proving the relevance of the issue of increasing the productivity and efficiency of transport and technological processes. Objective of work presented is to carry out a feasibility study of improving the transport performance by means of screw conveyors during the rotation of their casings.

Material and methods

In order to increase the productivity of material transportation by screw mechanisms and to reduce energy consumption, modern progressive constructions should be designed (Rogatynska et al., 2015; Klendii, 2007; Lyashuk et al., 2016), screw conveyors with rotary casings in particular. According to the conducted patent search, analysis of scientific literary sources, and synthesis (Hou et al., 2014; Mondal, 2018; Owen and Cleary, 2010; Tripathi et al., 2015), a number of designs of screw conveyors with

Contact address: Oleg Lyashuk, Ternopil Ivan Puluj National Technical University, Ukraine, e-mail: oleglashuk@ukr.net

rotary casings have been developed and patented. An experimental installation was developed; it is shown in Fig. 1. Screw working body and casing are driven separately by individual motors (screw working body – by an electric motor with a power of 2.2 kW; casing – by an electric motor with a power of 1.5 kW). A number of experimental studies were carried out using this device.

Experimental installation can operate in two modes: accelerated transportation of materials, and mixing bulk materials. In the first case, the casing rotates in the direction opposite to the direction of screw rotation, in the second case – in the direction of screw rotation. The bulk material enters the casing on the screw via the bunker.

The screw and casing rotate by means of electric motors controlled by a PC applying frequency converters. According to the developed methodology of conducting experimental studies, all necessary data are provided in tabular or graphical form.

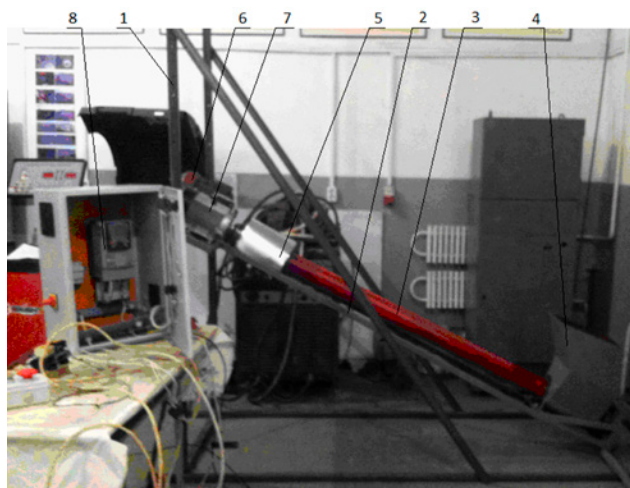


Fig. 1 General view of the experimental installation:
1 – support for adjusting the height of the material feed;
2 – frame; 3 – rotary casing with a screw inside; 4 – bunker;
5 – unloading nozzle; 6 – screw drive; 7 – casing drive;
8 – point for control of the rotational frequency of the casing and screw drives

Screw conveyor performance at various coefficients of filling the casing and rotational frequencies of the screw and casing is determined in automated mode. Power characteristics can be determined at a smooth and steep start, reversal and simulation of various loads in an automated mode using a frequency converter and a PC.

To determine the effect of the rotary casing use on screw conveyor properties, the performance of the proposed conveyor is determined. Screw rotational frequency n , casing rotational frequency n_c , and conveyor inclination

angle γ were taken into account during the casing rotation in a direction opposite to the screw rotation direction.

The conveyor performance was measured by means of electronic scales. Each of unchanged factors was experimentally studied at least 3 times. Subsequently, the average value of the results was determined and used for further statistical processing of experimental data. The response function, i.e. the performance $Q = f(n, n_c, \gamma)$ determined experimentally, is represented as a mathematical model of a complete quadratic polynomial. Screw rotational frequency n encoded by the index x_1 , casing rotational frequency n_c encoded by the index x_2 , and conveyor inclination angle γ encoded by the index x_3 were adopted as input experiment variables. Characteristics of factors and corresponding level values of the transported materials are given in Table 1.

On the basis of the experiment results in the coded values, a general information on the performance regression equation $Q_{(x_1, x_2, x_3)} = f(n, n_c, \gamma)$ dependent on the changes in the screw rotational frequency n , the casing rotational frequency n_c and the inclination angle of the conveyor γ are as follows:

– during the corn transportation:

$$Q_{(x_1, x_2, x_3)} = 8.88 + 3.373x_1 + 0.487x_2 - 0.29x_3 + 0.181x_1x_2 - 0.109x_1x_3 - 0.006x_2x_3 + 0.139x_1^2 - 0.451x_2^2 - 0.226x_3^2 \quad (1)$$

– during the wheat transportation:

$$Q_{(x_1, x_2, x_3)} = 9.34 + 3.55x_1 + 0.513x_2 - 0.306x_3 + 0.191x_1x_2 - 0.114x_1x_3 - 0.006x_2x_3 + 0.152x_1^2 - 0.473x_2^2 - 0.238x_3^2 \quad (2)$$

– during the barley transportation:

$$Q_{(x_1, x_2, x_3)} = 7.127 + 2.708x_1 + 0.392x_2 - 0.232x_3 + 0.144x_1x_2 - 0.086x_1x_3 - 0.0037x_2x_3 + 0.11x_1^2 - 0.36x_2^2 - 0.18x_3^2 \quad (3)$$

Accordingly, by importing natural values, transformation and simplification, the following expressions were deduced from Eqs. 1, 2, 3:

– during the corn transportation:

$$Q_{(n, n_c, \gamma)} = -1.22 + 1.31 \cdot 10^{-2} n + 5.69 \cdot 10^{-3} n_c + 9.28 \cdot 10^{-2} \gamma + 3.23 \cdot 10^{-6} n n_c - 4.95 \cdot 10^{-5} n \gamma - 2.04 \cdot 10^{-6} n_c \gamma + 3.48 \cdot 10^{-6} n^2 - 5.79 \cdot 10^{-6} n_c^2 - 1.87 \cdot 10^{-3} \gamma^2 \quad (4)$$

– during the wheat transportation:

$$Q_{(n, n_c, \gamma)} = -1.242 + 1.36 \cdot 10^{-2} n + 5.969 \cdot 10^{-3} n_c + 9.741 \cdot 10^{-2} \gamma + 3.41 \cdot 10^{-6} n n_c - 5.182 \cdot 10^{-5} n \gamma - 2.029 \cdot 10^{-6} n_c \gamma + 3.8 \cdot 10^{-6} n^2 - 6.03 \cdot 10^{-6} n_c^2 - 1.967 \cdot 10^{-3} \gamma^2 \quad (5)$$

Table 1 Characteristics of factors and their levels values

Coded designation of the factor	Factor designation	Values of factors levels
x_1	Screw rotational frequency n (rpm)	300–500–700
x_2	Casing rotational frequency n_c (rpm)	200–480–760
x_3	Inclination angle of the conveyor γ (deg)	14–25–36

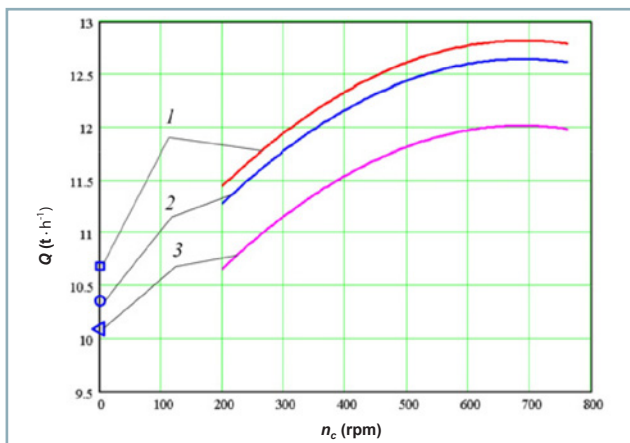


Fig. 2 Dependency graphs of the screw conveyor performance on the conveyor casing rotational frequency during the corn transportation screw diameter $D = 96$ mm; screw rotational frequency $n = 700$ rpm: 1) $\gamma = 14$ deg; 2) $\gamma = 25$ deg; 3) $\gamma = 36$ deg

– during the barley transportation:

$$Q_{(n, n_c, \gamma)} = -0.974 + 1.053 \cdot 10^{-2} n + 4.55 \cdot 10^{-3} n_c + 7.342 \cdot 10^{-2} \gamma + 2.571 \cdot 10^{-6} n n_c - 3.909 \cdot 10^{-5} n \gamma - 1.218 \cdot 10^{-6} n_c \gamma + 2.75 \cdot 10^{-6} n^2 - 4.592 \cdot 10^{-6} n_c^2 - 1.488 \cdot 10^{-3} \gamma^2 \quad (6)$$

Results and discussion

On the basis of experimental research results, graphic reproduction of intermediate common regression models in form of quadratic surfaces of the response and their two-dimensional cross sections (Figs. 2–5) of Q , performance was developed as a function, applying two variables $x_{i(1,2)}$ at a constant unchangeable level of the corresponding third factor $x_{i(3)} = \text{const}$. According to the analysis of the aforementioned regression equations, the main factors influencing the performance improvement are factors $x_1, x_2, (n, n_c)$ and combinations of these factors. An increase in the value of factor $x_3 (\gamma)$ led to a decrease in the performance.

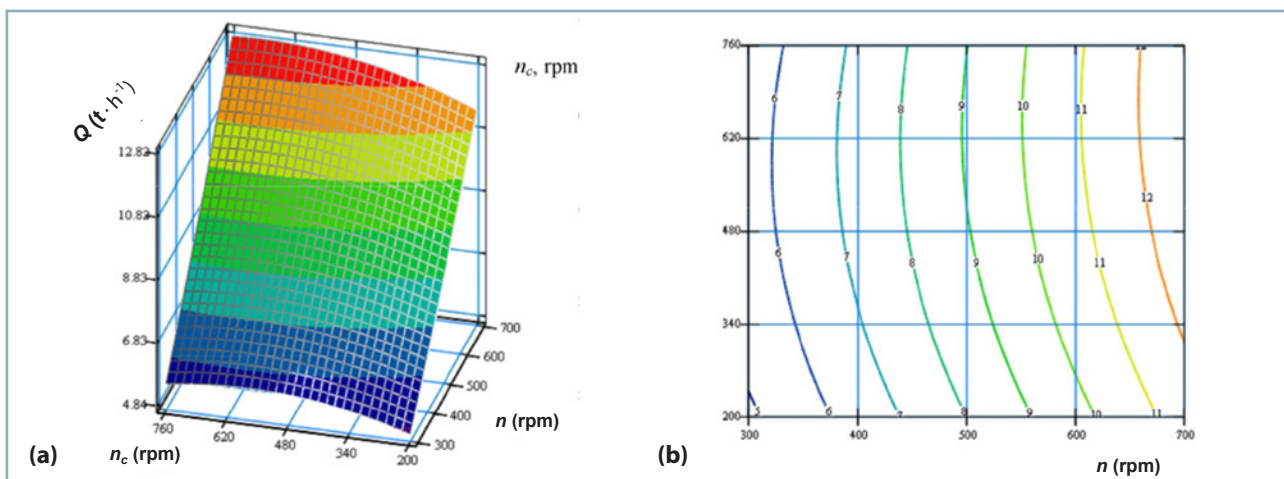


Fig. 3 Response surface (a) and two-dimensional cross section of the response surface (b) of conveyor performance dependence $Q_{(n, n_c)}$ during the corn transportation at the screw rotational frequency and the casing rotational frequency $\gamma = 14$ deg, $D = 96$ mm

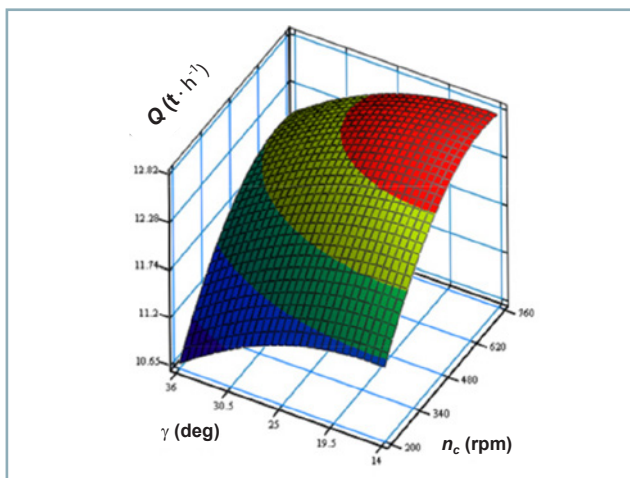


Fig. 4 Response surface of the conveyor performance dependence $Q_{(n_c, \gamma)}$ during the corn transportation at the casing rotational frequency and the conveyor inclination angle $n = 700$ rpm, $D = 96$ mm

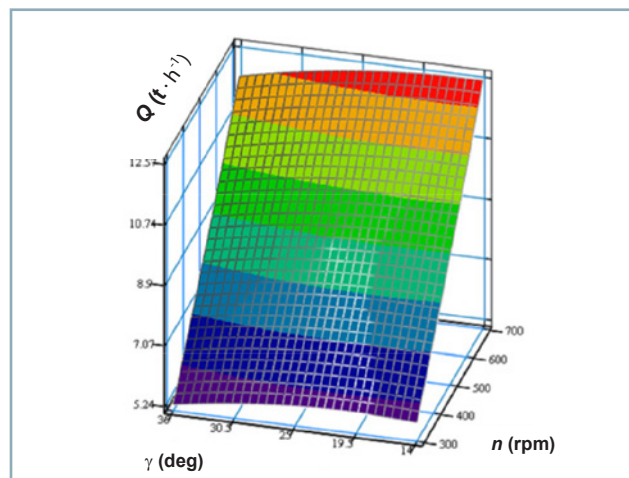


Fig. 5 Response surface of the conveyor performance dependence $Q_{(n, \gamma)}$ during the corn transportation at the screw rotational frequency and the conveyor inclination angle $n_c = 480$ rpm, $D = 96$ mm

According to the research results (Hevko et al., 2018b; Rogatynska et al., 2015; Sun et al., 2017), an increase in the casing rotational frequency n_c led to an increase in the screw conveyor performance Q by 18–24% in contrast to its operation mode utilizing a fixed casing. Furthermore, an increase in the casing rotational frequency n_c exceeding 620 rpm is irrational, since it does not change the conveyor performance. The casing rotational frequency in range from 460 to 620 rpm is rational, since it results in the greatest performance increase of the screw conveyor at different screw rotational frequencies n .

Moreover, the minimal casing rotational frequency to start the screw conveyor after its forced stop was determined. The bulk material moves upward along the axis of the screw working body under the following conditions: the greater the screw working body turn pitch, the more horizontal the axis inclination angle of the screw working body; and the greater the friction coefficient between the material and screw working body surface is, the greater the casing rotational frequency should be.

Moreover, the smaller the radius of the inner surface of the casing and the friction coefficient between the material and the casing surface are, the greater the casing rotational frequency should be:

$$n_c = \frac{30}{\pi} \sqrt{\frac{g \left(\sin \gamma \operatorname{tg} \left(\operatorname{arctg} \frac{T}{2\pi R} + \operatorname{arctg} f_1 \right) \left(1 + \frac{1}{f_2} \right) + \cos \gamma \right)}{R_1}} \quad (7)$$

where:

- T – screw turn pitch in the outer radius
- g – free fall acceleration
- R_1 – casing inner surface radius

Table 2 Measurement results of power and torque (the screw shaft under study) at the corresponding casing rotational frequency

Screw rotational frequency n (rpm)	Power (screw shaft) (%)	Torque (screw shaft) (%)
Casing rotational frequency n_c – 312 (rpm)		
280	5	11.4
420	8	12.8
560	11	13.2
700	14	13.7
Casing rotational frequency n_c – 468 (rpm)		
280	6	13.5
420	9	14.8
560	12	14.4
700	15	14.5
Casing rotational frequency n_c – 624 (rpm)		
280	6	14.3
420	10	17.0
560	14	17.1
700	17	17.8

- f_1 – friction coefficient between the bulk material and screw surface
- f_2 – friction coefficient between the bulk material and casing surface
- R – screw external radius

The experimental power and torque data in percentages are shown in Tables 2 and 3. The data were recorded via PC during a series of experiments using Altivar series frequency converters.

The data of power and torque (the screw shaft under study) during the material reload without rotation of the casing are presented in Table 4.

On the basis of experimental results and information on the power driving the screw, regression equation will be as follows:

– during the corn transportation:

$$N_{(n, n_c, \gamma)} = 0.0625 + 2.02 \cdot 10^{-4} n - 1.51 \cdot 10^{-4} n_c + 6.57 \cdot 10^{-4} \gamma + 1.80 \cdot 10^{-7} n n_c + 2.44 \cdot 10^{-6} n \gamma + 7.28 \cdot 10^{-7} n_c \gamma + 1.38 \cdot 10^{-7} n^2 + 2.14 \cdot 10^{-7} n_c^2 - 1.9 \cdot 10^{-5} \gamma^2 \quad (8)$$

– during the wheat transportation:

$$N_{(n, n_c, \gamma)} = 0.0625 + 2.02 \cdot 10^{-4} n - 1.51 \cdot 10^{-4} n_c + 6.57 \cdot 10^{-4} \gamma + 1.80 \cdot 10^{-7} n n_c + 2.56 \cdot 10^{-6} n \gamma + 7.63 \cdot 10^{-7} n_c \gamma + 1.42 \cdot 10^{-7} n^2 + 2.23 \cdot 10^{-7} n_c^2 - 2.04 \cdot 10^{-5} \gamma^2 \quad (9)$$

– during the barley transportation:

$$N_{(n, n_c, \gamma)} = 0.0480 + 1.58 \cdot 10^{-4} n - 1.15 \cdot 10^{-4} n_c + 4.38 \cdot 10^{-4} \gamma + 1.38 \cdot 10^{-7} n n_c + 1.96 \cdot 10^{-6} n \gamma + 5.89 \cdot 10^{-7} n_c \gamma + 1.07 \cdot 10^{-7} n^2 + 1.70 \cdot 10^{-7} n_c^2 - 1.57 \cdot 10^{-5} \gamma^2 \quad (10)$$

Table 3 Measurement results of power and torque (the casing under study) at the appropriate screw rotational frequency

Casing rotational frequency n_c (rpm)	Power (casing) (%)	Torque (casing) (%)
Screw rotational frequency n – 700 (rpm)		
312	9	20.8
468	10	22.6
624	11	23.2
780	10	22.7

Table 4 Measurement results of power and torque (the screw shaft under study) after stopping the casing

Screw rotational frequency n (rpm)	Power (screw shaft) (%)	Torque (screw shaft) (%)
Casing rotational frequency n_c – 0 (rpm)		
312	8	19.5
468	12	19.1
624	16	19.1
780	20	19.2

On the basis of experimental results and information on the power driving the casing, regression equation will be as follows:

– during the corn transportation:

$$N_{c(n, n_c, \gamma)} = -0.0326 + 7.14 \cdot 10^{-5} n + 3.17 \cdot 10^{-5} n_c + 9.09 \cdot 10^{-4} \gamma + 2.06 \cdot 10^{-7} n_c^2 \quad (11)$$

– during the wheat transportation:

$$N_{c(n, n_c, \gamma)} = -0.0376 + 7.86 \cdot 10^{-5} n + 3.45 \cdot 10^{-5} n_c + 1 \cdot 10^{-3} \gamma + 2.17 \cdot 10^{-7} n_c^2 \quad (12)$$

– during the barley transportation:

$$N_{c(n, n_c, \gamma)} = -0.0262 + 5.74 \cdot 10^{-5} n + 2.45 \cdot 10^{-5} n_c + 7.31 \cdot 10^{-4} \gamma + 1.66 \cdot 10^{-7} n_c^2 \quad (13)$$

On the basis of experimental results and information on the specific energy consumption, regression equation will be as follows:

– during the corn transportation:

$$W_{(n, n_c, \gamma)} = 0.0132 - 9.31 \cdot 10^{-6} n - 6.4 \cdot 10^{-7} n_c + 1.34 \cdot 10^{-4} \gamma - 1.72 \cdot 10^{-8} n n_c + 8.12 \cdot 10^{-8} n \gamma - 7.28 \cdot 10^{-8} n_c \gamma + 1.35 \cdot 10^{-8} n^2 + 3.14 \cdot 10^{-8} n_c^2 + 2.18 \cdot 10^{-6} \gamma^2 \quad (14)$$

– during the wheat transportation:

$$W_{(n, n_c, \gamma)} = 1.065 \cdot 10^{-2} + 1.37 \cdot 10^{-6} n + 3.09 \cdot 10^{-6} n_c + 5.17 \cdot 10^{-5} \gamma - 2.59 \cdot 10^{-8} n n_c - 1.06 \cdot 10^{-7} n \gamma + 4.76 \cdot 10^{-8} n_c \gamma + 7.91 \cdot 10^{-9} n^2 + 2.84 \cdot 10^{-8} n_c^2 + 2.94 \cdot 10^{-6} \gamma^2 \quad (15)$$

– during the barley transportation:

$$W_{(n, n_c, \gamma)} = 0.0115 + 1.57 \cdot 10^{-6} n + 2.29 \cdot 10^{-6} n_c + 5.22 \cdot 10^{-5} \gamma - 2.64 \cdot 10^{-8} n n_c - 1.06 \cdot 10^{-7} n \gamma + 4.78 \cdot 10^{-8} n_c \gamma + 8.06 \cdot 10^{-9} n^2 + 3.02 \cdot 10^{-8} n_c^2 + 3.15 \cdot 10^{-6} \gamma^2 \quad (16)$$

When the casing rotates at the rotational frequency of 468 rpm, the screw performance at a rotational frequency 700 rpm increases by 20%. At the same time, the power driving the screw falls from 20% to 15% (2.2 kW motor), and the power driving the casing falls to 10% (1.5 kW motor).

Subsequently, the total power rise is: $\Delta P_{30} = (10\% \cdot 1.5 / 2.2) - (20\% - 15\%) = 1.82\%$.

Therefore, when the performance increases by 20% (the casing rotates at the rotational frequency 468 rpm and the screw at frequency 700 rpm), there is a rise in power of 1.82%.

Providing the conveyor performance without screw rotation is 100%, the power driving the screw is 20%. When the conveyor performance with the screw rotation increases by 20%, the total power of the conveyor is $20\% + 1.82\% = 21.82\%$. In comparison to the power rise, performance improvement is: $\Delta E_{30} = (100\% + 20\%) / 100\% - (20\% + 1.82\%) / 20\% = 0.109$.

Taking into account the performance improvement and electricity consumption, the productivity of casing rotating

at frequency 468 rpm in a screw conveyor, in which the screw rotates at frequency 700 rpm, is 10.9%.

Accordingly, the annual electricity savings due to the performance improvement of the screw conveyor with a rotary casing with the specified parameters are determined by the following formula:

$$E = P_1 \cdot V_e \cdot \Delta E \cdot N_h \cdot N_t \cdot N_{wd} \cdot K_e \quad (17)$$

where:

P_1 – price for 1 kW·h⁻¹ of electricity (II class – 1.96 UAH from 1.12.2017 for industrial enterprises and consumers equal to them with the connected power of 750 kVA and more)

V_e – electricity consumption volume due to equipment operation (kWh) (2.2)

N_h – number of hours per tour (8)

N_t – number of tours (1)

N_{wd} – number of working days per year (240)

K_e – coefficient of equipment use (0.92)

$$E_{30} = 1.96 \cdot 2.2 \cdot 0.109 \cdot 8 \cdot 1 \cdot 240 \cdot 0.92 = 830.22 \text{ UAH}$$

In addition to this, during feasibility studies of the performance of rotary casings of screw conveyors, the following factors should be taken into account when the operator is involved in the reload process. Providing the performance increases, the amount of working time of the operator involved in the production process of reloading the appropriate amount of materials will be reduced, i.e. the operator's working time should be reduced by a percentage of the reload operation improvement. Subsequently, the savings on the wages of the operator in terms of the single social contribution (0.22 in accordance with the Law of Ukraine of December 21, 2016, No. 1801-VIII "On the State Budget of Ukraine for 2017") will be:

$$E_s = S_m \cdot K_c \cdot 12 \cdot P_n / 100\% \quad (18)$$

where:

S_m – average monthly salary (8,791 UAH per month in December 2018 according to <https://www.work.ua/ua/stat/>)

K_c – coefficient with consideration of the single social contribution (1.22)

P_n – percentage of the number of redundant workers due to performance improvement (%)

$$E_{s30} = (8,791 \cdot 1.22 \cdot 12 \cdot 20\%) / 100\% = 25,740.05 \text{ UAH}$$

Considering all these factors, the total savings resulting from the usage of screw conveyors with rotary casings will be 26,570.27 UAH. Demurrage of drivers and vehicles when loading should be recalculated with taking into account the loading operation improvement, amortization deductions of a vehicle, and saving of drivers' wages. On the other hand, some higher depreciation charges should be considered when using a modernized screw conveyor, because it is constructively more complicated and its manufacture cost is slightly higher.

When the casing rotates at the rotational frequency 4624 rpm, the performance of screw rotating at frequency 700 rpm is increased by 24%. At the same time, the power driving the screw falls from 20% to 17% (2.2 kW motor), and the power driving the casing falls to 11% (1.5 kW motor).

Therefore, the total power growth is: $\Delta P_{40} = (11\% \cdot 1.5 / 2.2) - (20\% - 17\%) = 4.5\%$.

Consequently, when the performance improvement is 24% (the casing rotates at the rotational frequency 624 rpm and a screw at the rotational frequency 700 rpm), the power increase is 4.5%.

If the conveyor performance without screw rotation is assumed 100%, then the power driving the screw is 20%. When the conveyor performance improvement at screw rotation is 24%, the total capacity of the conveyor will be $20\% + 4.5\% = 24.5\%$. Subsequently, according to the recalculation, performance improvement will be, in comparison with the power growth: $\Delta E_{40} = (100\% + 24\%) / 100\% - (20\% + 4.5\%) / 20\% = 0.015$.

Considering both the performance improvement and electricity consumption, the efficiency of casing rotation at the rotational frequency of 624 rpm in a screw conveyor, in which the screw rotates at frequency of 700 rpm, will be 1.5%. Accordingly, the annual savings on electricity thanks to the screw conveyor performance improvement with a rotary casing at the specified parameters will be: $E_{40} = 1.96 \cdot 2.2 \cdot 0.015 \cdot 8 \cdot 1 \cdot 240 \cdot 0.92 = 114.25$ UAH.

Savings on the wages of the operator involved in servicing the conveyor will be: $E_s = (8,791 \cdot 1.22 \cdot 12 \cdot 24\%) / 100\% = 30,888,06$ UAH.

All in all, the final savings resulting from the usage of a screw conveyor with a rotary casing will be 31,002.31 UAH.

On the basis of presented calculations, the performance improvement of a screw conveyor with a rotary casing is considered economically feasible. Generally, the casing rotation in a screw conveyor allows (if certain structural and technological aspects are met) obtaining of a significant economic effect and increase of the efficiency of transport operations (by 24%) without excessive overconsumption of electricity. The overall economic costs can be reduced up to 10% if the optimal parameters of the screw conveyor with a rotary casing are utilized. In addition to this, material perturbation due to casing rotation leads to further reductions in terms of power consumption.

Conclusion

The most effective parameters of the screw conveyor with a rotary casing include casing rotation frequency of 468 rpm and screw rotation frequency of 700 rpm. Thanks to these parameters, device performance increased by 20% and power driving the screw decreased from 20% to 15% (2.2 kW motor), and power driving the casing is decreased by 10% (1.5 kW motor). Observed total capacity growth was 1.82%. A further increase in the casing rotational frequency led to an increase in the transportation process productivity by 24%, representing a positive phenomenon.

If optimal parameters of the screw conveyor with a rotary casing are applied, overall economic costs can be reduced by more than 10%. Material perturbation occurring due to casing rotation can lead to reduction in overall power consumption.

References

- BARANOVSKY, V. M. – HEVKO, R. B. – DZYURA, V. O. – KLENDII, O. M. – KLENDII, M. B. – ROMANOVSKY, R. M. 2018. Justification of rational parameters of a pneumoconveyor screw feeder. In INMATEH: Agricultural Engineering, vol. 54, no. 1, pp. 15–24.
- FERNANDEZ, J. W. – CLEARY, P. W. – MCBRIDE, W. 2011. Effect of screw design on hopper draw down by a horizontal screw feeder. In Seventh International Conference on CFD in the Minerals and Process Industries CSIRO, Melbourne, Australia, 9–11 December, pp. 1–6.
- HEVKO, R. B. – ZALUTSKYI, S. Z. – TKACHENKO, I. G. – KLENDII, O. M. 2015. Development and investigation of reciprocating screw with flexible helical surface. In INMATEH: Agricultural Engineering, vol. 46, no. 2, pp. 133–138.
- HEVKO, B. M. – HEVKO, R. B. – KLENDII, O. M. – BURIK, M. V. – DZYADYKEVYCH, Y. V. – ROZUM, R. I. 2018a. Improvement of machine safety devices. In Acta Polytechnica, Journal of Advanced Engineering, vol. 58, no. 1, pp. 17–25.
- HEVKO, R. B. – LIUBIN, M. V. – TOKARCHUK, O. A. – LYASHUK, O. L. – POHRISHCHUK, B. V. – KLENDII, O. M. 2018b. Determination of the parameters of transporting and mixing feed mixtures along the curvilinear paths of tubular conveyors. In INMATEH: Agricultural Engineering, vol. 55, no. 2, pp. 97–104.
- HOU, Q. – DONG, K. – YU, A. 2014. Dem study of the flow of cohesive particles in a screw feeder. In Powder Technology, vol. 256, pp. 529–539.
- HUI, L. – WANFU, L. 2013. The experimental research of screw conveyor feeding system. In New Trends in Mechanical Engineering and Materials. Book Series: Applied Mechanics and Materials, vol. 251, pp. 101–103.
- KLENDII, M. B. 2007. Substantiation of the parameters of a reloading branchpipe of a screw conveyor. Ternopil I. Puluj National Technical University, 137 pp.
- LYASHUK, O. L. – ROGATYNSKA, O. R. – SERILKO, D. L. 2015. Modelling of the vertical screw conveyor loading. In INMATEH: Agricultural Engineering, vol. 45, no.1, pp. 87–94.
- LOVEIKIN, V. – ROGATYNSKA, L. 2011. A model of loose material transportation by means of high-speed conveyers with elastic operating devices. In Bulletin of Ternopil I. Puluj National Technical University, vol. 16, pp. 66–70.
- LYASHUK, O. – SOKIL, M. – KLENDII, V. – SKYBA, O. – DMYTRENKO, V. 2016. The study on nonlinear model of dynamics of a system 'extruder elastic auger working body'. In Acta Technologica Agriculturae, vol. 19, no. 4, pp. 102–107.
- MONDAL, D. 2018. Study on filling factor of short length screw conveyor with flood-feeding condition. Materials Today: Proceedings, vol. 5, pp. 1286–1291.
- TRIPATHI, N. – SHARMA, A. – MALLICK, S. S. – WYPYCH P. W. 2015. Energy loss at bends in the pneumatic conveying of fly ash. In Particology, vol. 21, pp. 65–73.
- OWEN, P.J. – CLEARY, P.W. 2010. Screw conveyor performance: comparison of discrete element modelling with laboratory experiments. In Progress in Computational Fluid Dynamics, vol. 10, no. 5–6, pp. 327–333.
- PEZO, L. – JOVANOVIĆ, A. – PEZO, M. – COLOVIC, R. 2015. Modified screw conveyor-mixers – discrete element modeling approach. In Advanced Powder Technology, vol. 26, pp. 1391–1399.
- ROGATYNSKA, O. – LYASHUK, O. – PELESHOK, T. – LIUBACHIVSKYI, R. 2015. Investigation of the process of loose material transportation by means of inclined screw conveyers. In Bulletin of Ternopil I. Puluj National Technical University, vol. 79, pp. 137–143.
- ROGATYNSKIY, R. – HEVKO, I. – GYPKA, A. – GARMATYK, O. – MARTSENKO, S. 2017. Feasibility study of the method choice of manufacturing screw cleaning elements with the development and use of software. In Acta Technologica Agriculturae, vol. 20, no. 2, pp. 36–41.
- SUN, X. X. – MENG, W. J. – YUAN, Y. 2017. Design method of a vertical screw conveyor based on Taylor-Couette-Poiseuille stable helical vortex. In Advances in Mechanical Engineering, vol. 9, no.7, pp. 123–132.
- ZAREIFOROUGH, H. – KOMARIZADEH, M. H. – ALIZADEH, M. R. 2010. Effect of crop-screw parameters on rough rice grain damage in handling with a horizontal screw conveyor. In Journal of Food Agriculture and Environment, vol. 8, no. 3–4, pp. 494–499.



Acta Technologica Agriculturae 4
Nitra, Slovaca Universitas Agriculturae Nitriae, 2019, pp. 146–151

INVESTIGATIONS OF THE DYNAMICS OF A FOUR-ELEMENT MACHINE-AND-TRACTOR AGGREGATE

Volodymyr BULGAKOV¹, Semjons IVANOV^{2*}, Valerii ADAMCHUK³, Roman ANTOSHCHENKOV⁴

¹National University of Life and Environmental Sciences of Ukraine, Kiev, Ukraine

²Latvia University of Life Sciences and Technologies, Jelgava, Latvia

³Institute for Agricultural Engineering and Electrification, Hlevakha, Ukraine

⁴Kharkiv Petro Vasilenko National Technical University of Agriculture, Ukraine

The paper presents a dynamic model of four-element machine-and-tractor designed on the basis of a combined soil-cultivating-sowing aggregate and a tractor with an articulated frame. The pseudo velocity of the first tractor half-frame was considered a generalised coordinate. The control impact upon the tractor was obtained by means of the bending angle of the tractor half-frames. The trajectories and movement speeds of the aggregate elements were calculated as a function of time for the driving mode along a straight-line path and the tractor movement according to the harmonic control law. By means of the measuring system, trajectories of the aggregate elements were obtained. It was established that the movement trajectories of the aggregate elements represent a complex assessment parameter of the mathematical model adequacy of the aggregate plane-parallel movement. There was found a regularity of the aggregate turning radius and the bending angle of the tractor half-frames.

Keywords: dynamics; movement; mathematical mode; measuring system

Increased crop production efficiency can be achieved by using combined tillage-sowing aggregates, which can perform two or more technological operations in one field pass. Such aggregates are usually multi-element machines consisting of three elements – a tractor, a seed tank and a sowing machine – moving in succession one after the other (Belojev et al., 2015; Ivanovs et al., 2018). The most frequent layout schemes of such aggregates are: 1 tractor – tank for seed material – sowing machine; 2 tractor – sowing machine – tank. Differences in the dynamics of the aggregates with either of the two schemes are insufficiently studied.

Conventional ways of constructing dynamic and mathematical models for such systems are based on a manual technology (Blundell and Harty, 2004; Werner, 2012; Fleischmann and Berns, 2013). Recently, systems of a computer output of the dynamics equations have been paid much attention. A quite efficient one is the special system of computer algebra SCCA KiDiM, the theoretical foundations of which were described by Franke et al. (2012). The studies of the dynamics of the multi-element machine-and-tractor aggregate (MTA) are traditionally based on the formation of holonomic equations and nonholonomic systems (Blundell and Harty, 2004). Taking into account the regularities of rolling torque of the aggregate wheels, including even their elasticity properties, it belongs to the class of nonholonomic mechanical systems. In order to investigate the dynamics of multi-element machines, the D'Alembert-Lagrange principle (Bulgakov et al., 2016) or the Lagrange equations of the 2nd kind can be applied. Usually, research of the mobile machine

movement is studied together with a semi-trailer by means of the Lagrange equations of the 2nd kind (Chieh, 1995; Siew et al., 2009; Bulgakov et al., 2018). A mathematical model of the single machine movement has been repeatedly investigated (Blundell and Harty, 2004; Karkee and Seward, 2010). Liljedahl et al. (1996) investigated the dynamics and stability of a mobile machine. Aforementioned works examine the mathematical model of the multi-element aggregate movement as integral; therefore, with a change in the structure or internal connections, it is necessary to reconstruct it again, resulting in more labour and time necessary for the research. Therefore, in order to correctly solve the problems of the dynamics of nonholonomic multi-element systems, it is necessary to establish the basic equations of dynamics and substantiate the equations of relations similarly to Franke et al. (2012). Numerous studies on the dynamics of agricultural aggregates as multi-element (multi-mass) mechanical systems do not try to deal with the scientific issue by an arbitrary combination of system elements. Investigation of the dynamics of these systems requires a methodology development for the formation of dynamics equations taking into account the changes in the structures and methods of machine aggregation. Methodology for establishing the equations of the dynamics of MTA cannot be used in study of aggregates with interchangeable structures, since it does not allow changing the mathematical model depending on the aggregation scheme of the multi-element aggregate elements. Known measuring systems of the MTA dynamics are either universal or utilized in automated control systems of the technological

Contact address: Semjons Ivanovs, Latvia University of Life Sciences and Technologies, Jelgava, Latvia, e-mail: semjons@apollo.lv

processes. A disadvantage of such systems lies in possibility to control only the intermediate values of the aggregate performance parameters with their help. Other systems utilize a small number of sensors and therefore can measure only a limited number of aggregate performance parameters (Yahya et al., 2004). The trajectories of a tractor or car movement are determined using the GPS receivers installed on machines (Yahya, 2000).

Investigation presented aims to study theoretically the dynamics of a multi-element MTA and to compare it with experimental data through mathematical simulation of a dynamic model based on the HTZ-17224 tractor and a combined soil-cultivating-sowing aggregate APP-6.

Material and methods

In order to conduct the investigation, methods of higher mathematics and theoretical mechanics were used for the solution of systems of nonlinear differential equations; bringing the dynamic equations to the Cauchy form was carried out by the Kratu method; numerical integration of such equations was carried out by Runge-Kutta methods with automated step selection, as well as the methods of programming and experimental field

research. Processing of the results of both theoretical and experimental investigations was carried out by numerical methods using a PC. To compile an analytical mathematical model of a multi-element MTA, a design scheme (Fig. 1) will be used. The tractor with an articulated frame aggregates a tank for seed material and a sowing machine. When creating a dynamic model, it is necessary to take into account only the main elements of the multi-element MTA that affect its dynamics.

To construct an equivalent dynamic model, the following notation will be used (Fig. 1): C_{ij} – wheel centres (i – row number, j – number in the row); A_k – frame frontal points ($k = 1, 2, 3, 4$, for a four-element aggregate); O_k – mass centres of tractor, seed tank and sowing machine; B_k – rear axle midpoint of the tractor, seed tank and sowing machine; P_k – instantaneous speed centres (ISC) of the aggregate frame elements; Ψ – bending angle of the tractor half-frames; Φ_k – angles between the lines, fixed bodies, wheel axles, and directions to the mass centres of the corresponding ISC; θ_k – angles from the lines of indicated axles to the directions of the frontal joints of the ISC; δ_1, δ_2 – angles from the axle lines to the directions of the rear joints from the ISC; γ_k – angles, longitudinal axles of the vehicles with axis x of the

fixed coordinate system; F_{Bk} – forces acting upon the aggregate elements. This system of differential equations consists of equations of kinematic links and an equation of dynamics. The equations of kinematic links describe links between the projections of the linear and angular velocities, and accelerations. For a four-element MTA, the equations of kinematic links are as follows:

$$\delta_1 = \arcsin \frac{\sin \psi}{\sqrt{\sin^2 \psi + \left(\frac{A_2 B_2}{B_1 A_2} + \cos \psi\right)^2}}$$

$$\delta_n = \arctan(\lambda_n \cdot \tan \theta_n)$$

$$\theta_1 = \arcsin \frac{\sin \psi}{\sqrt{\sin^2 \psi + \left(\frac{B_1 A_2}{A_2 B_2} + \cos \psi\right)^2}}$$

$$\theta_n = \gamma_{n-1} - \gamma_n - \delta_{n-1}$$

$$\varphi_i = \arctan(\mu_i \tan \theta_i)$$

$$\omega_i = s \dot{A}_i \frac{\sin \theta_i}{A_i B_i} \quad (1)$$

$$s \dot{A}_n = s A_n + s \dot{A}_{n-1} \sqrt{(\cos \theta_{n-1})^2 + (\lambda_{n-1} \sin \theta_{n-1})^2}$$

$$s \dot{B}_i = s B_i + s \dot{A}_i \cos \theta_i$$

$$s \dot{O}_n = s O_n + s \dot{A}_i \sqrt{(\cos \theta_i)^2 + (\mu_i \sin \theta_i)^2}$$

$$\dot{\gamma}_i = \gamma_i + \omega_i$$

$$x \dot{A}_i = x A_i + s \dot{A}_i \cos(\theta_i + \gamma_i)$$

$$y \dot{A}_i = y A_i + s \dot{A}_i \sin(\theta_i + \gamma_i)$$

$$x \dot{B}_i = x B_i + s \dot{B}_i \cos \gamma_i$$

$$y \dot{B}_i = y B_i + s \dot{B}_i \sin \gamma_i$$

where:

- s – pseudo-coordinates of the points of aggregate elements
- x, y – coordinates of the points of aggregate elements
- $i = 1 \dots, 4$ – number of the aggregate element, designating the first half-frame of the tractor, the second half-frame of the tractor, the seed tank, and the sowing machine, respectively
- $n = 2 \dots, 4$ – number of the aggregate element similarly denoting the second half-frame of the tractor, the seed tank, and the sowing machine

Pseudo-velocity of point A – $s \dot{A}_1$ is taken as the generalised coordinate. The mathematical model has one degree of freedom, pseudo-velocity of point A , and 29 coordinate equations

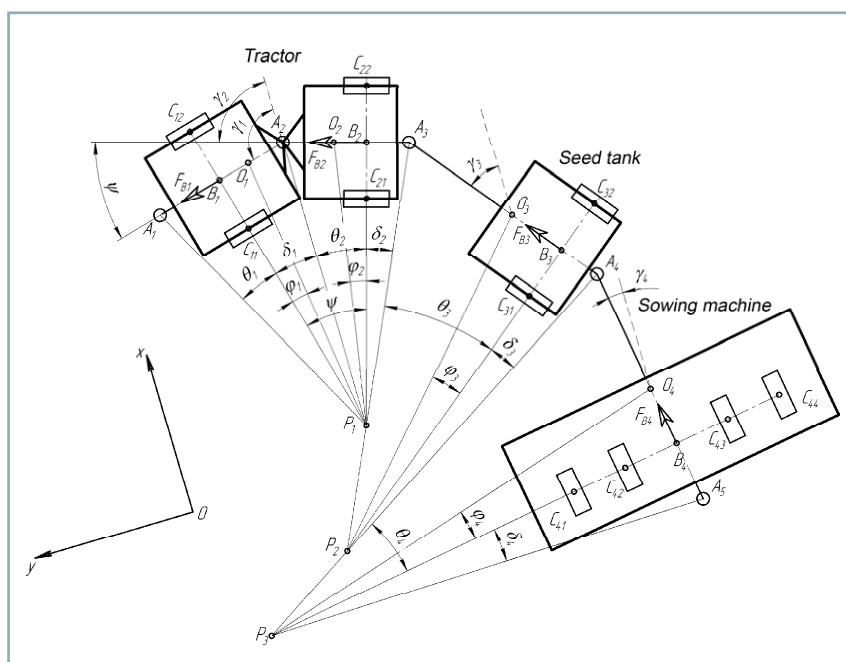


Fig. 1 Design scheme of a multi-element MTA

with dependent variations (Eq. 1). The dynamic equation is as follows:

$$s\dot{A}_1 = M_f [1][1]^{-1} \cdot F_f [1] \tag{2}$$

where:

factors $M_f [1][1]^{-1}$ and $F_f [1]$ of Eq. 2 are:

$$M_f [1][1]^{-1} = m_1 (\cos^2 \theta_1 + 0.12755 \sin^2 \theta_1) + m_2 \left(\frac{dsO_2}{dsA_1} \right)^2 + m_3 \left(\frac{dsO_3}{dsA_1} \right)^2 + m_4 \left(\frac{dsO_4}{dsA_1} \right)^2 + J_1 \left(\frac{d\omega_1}{dsA_1} \right)^2 + J_2 \left(\frac{d\omega_2}{dsA_1} \right)^2 + J_3 \left(\frac{d\omega_3}{dsA_1} \right)^2 + J_4 \left(\frac{d\omega_4}{dsA_1} \right)^2 \tag{3}$$

$$F_f [1] = -m_1 \frac{dsO_1}{dsA_1} \cdot s\ddot{O}_1 - m_2 \frac{dsO_2}{dsA_1} \cdot s\ddot{O}_2 - m_3 \frac{dsO_3}{dsA_1} \cdot s\ddot{O}_3 - m_4 \frac{dsO_4}{dsA_1} \cdot s\ddot{O}_4 - J_3 \frac{d\omega_1}{dsA_1} \cdot \dot{\omega}_3 + J_4 \frac{d\omega_4}{dsA_1} \cdot \dot{\omega}_4 - \frac{dsB_1}{dsA_1} \cdot F_{B_1} + \frac{dsB_2}{dsA_1} \cdot F_{B_2} + \frac{dsB_3}{dsA_1} \cdot F_{B_3} - \frac{dsB_4}{dsA_1} \cdot F_{B_4} \tag{4}$$

For the purpose of experiments, a measuring system was developed in order to determine the dynamic and traction-energy indicators of mobile machines. The primary element of this system is the computation module, since processing and storing of data obtained from sensors and measuring devices take place in this unit. A hard disk or a USB flash drive was used as a data storage device. The computation module includes a touch screen display for showing the recorded parameters and controlling the measuring system, making it usable without a PC. Block diagram of the measuring system for determination of dynamic and traction-energy indicators of the performance of mobile machines is presented in Fig. 2.

The system can process data by eight inertial measuring devices (IMD) [6]. These devices are used to determine the accelerations, angular velocities, field directions and the Euler angles. Furthermore, wheel dynamics sensors [14] also contain inertial measuring devices. They are installed in the wheel turning centre and transmit data via a 2.4 GHz radio channel. Such sensors allow the measuring of the slipping of tractor wheels by the following equation:

$$\delta = \frac{2\pi \cdot \omega \cdot r_D - v_D}{v_D} \cdot 100\% \tag{5}$$

where:

ω – wheel current turning speed determined by the sensor

r_D – real radius

v_D – actual driving speed measured by the GPS receiver

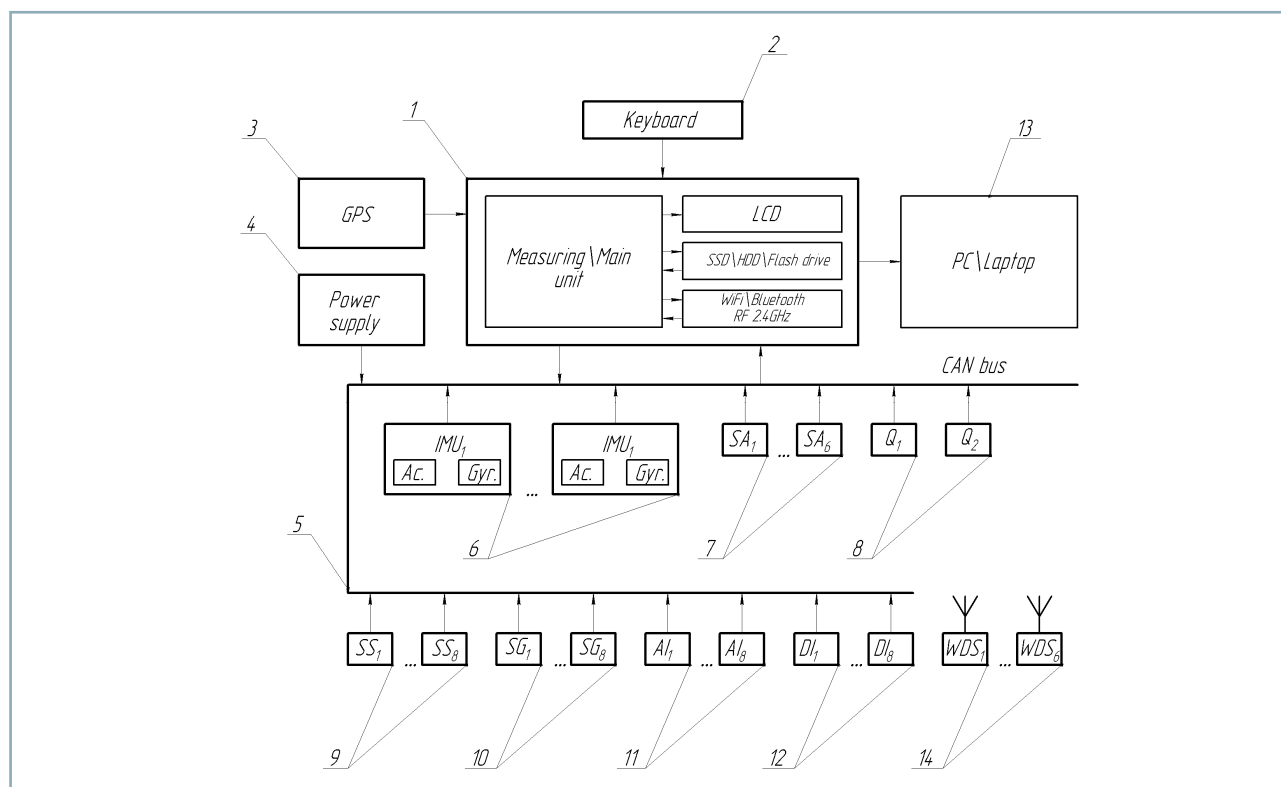


Fig. 2 Block diagram of the measuring system for determination of dynamic and traction-energy indicators of the performance of mobile machines

- 1 – computation module; 2 – control panel; 3 – GPS receiver; 4 – power supply; 5 – CAN data bus; 6 – inertial measuring device; 7 – turning angle sensor; 8 – fuel flow meter; 9 – revolution speed sensor; 10 – electronic dynamometer; 11 – analogue inputs; 12 – discrete inputs; 13 – PC; 14 – wheel dynamics sensor

This method of determining the turning speed of the tractor wheels allows a dynamic exploration of the slip for each of the wheels at a particular moment of time (the instantaneous value). The method of measuring the wheel turning speed helps to prevent the need for utilization of expensive precision encoders, as well as for changes in the tractor transmission design in order to install the turning speed sensors based on the Hall effect.

Results and discussion

Solving of the system of differential equations (Eqs. 1–4) was performed in a special system of the computer algebra SCCA KiDiM. The HTZ-17224 tractor and the APP-6 – a combined soil-cultivating-sowing aggregate – were selected as objects of theoretical studies. Control of the tractor is exerted by the bending angle of the tractor half-frame ψ . The theoretical research results are presented in Figs. 3–5.

The aggregate rectilinear movement scheme (Fig. 3) was obtained under the condition that the bending angle of the tractor half-frames was equal to zero $\psi = 0^\circ$. The actual movement trajectory of the aggregate elements varies according to the harmonic law (Denham et al., 2007). Tractor with an articulated frame changes the trajectory of movement by the bending angle of semi-frames given by the law $\psi = 0.2 \sin(0.5t)$. When moving along a sinusoidal path, the bending angles of the first and the second tractor half-frames coincide (Fig. 4), the range of their oscillations is $\Delta\gamma_1 = \gamma_2 = 0.77$ rad, and the period is $T = 12.5$ s. The oscillation range of the angles (γ) of the seed tank and sowing machine is $\Delta\gamma_3 = 0.67$ rad and $\Delta\gamma_4 = 0.45$ rad with a period $T = 12.5$ s, which indicates a smaller deviation of these elements from the rectilinear line movement path.

The movement velocities of the mass centres of aggregate elements when moving along a sinusoidal path are shown in Fig. 5. A decrease in these velocities was observed at the movement beginning at $t \leq 7.5$ s. The seed tank mass centre showed the lowest velocity at the beginning of the movement $s\dot{O}_3 = 2.75 \text{ m}\cdot\text{s}^{-1}$, with an oscillation range of $0.12 \text{ m}\cdot\text{s}^{-1}$ and a period $T = 12.5$ s. The velocity oscillation range of the mass centres of the first and second aggregate half-frames was $0.08 \text{ m}\cdot\text{s}^{-1}$; this oscillation range was $0.02 \text{ m}\cdot\text{s}^{-1}$ for the sowing machine. In order to evaluate the obtained theoretical model, a comparison of the trajectory of the mass centres of aggregate elements was experimentally carried out (Fig. 6).

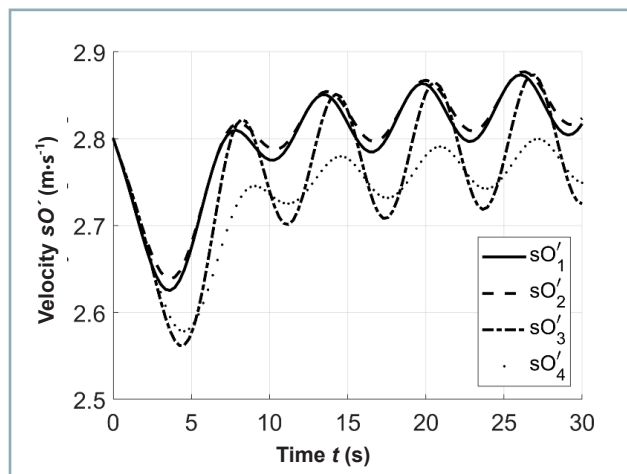


Fig. 4 Dependence of the turning angles of aggregate elements on time

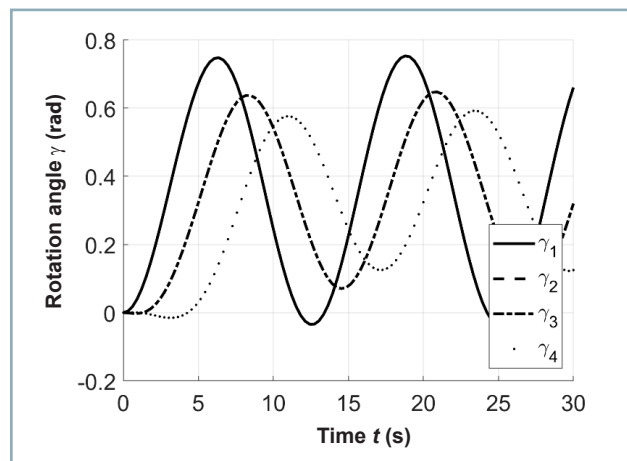


Fig. 5 Dependence of the velocities of the mass centres of aggregate elements on time when moving along a sinusoidal path

At a fixed bending angle of the tractor half-frames $\psi = 10^\circ$, the aggregate turning radius is $r_p = 16.25$ m. Obtained as a result of experimental and theoretical research, the discrepancy between the values of the trajectories of the tractor, seed tank and sowing machine does not exceed 4%. The trajectories of the aggregate elements represent a complex parameter for the assessment of the mathematical model adequacy of an aggregate plane-parallel movement.

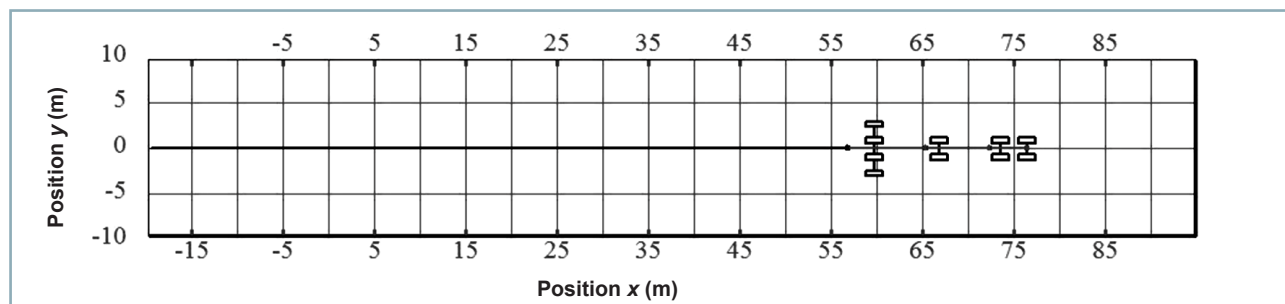


Fig. 3 Scheme of the aggregate rectilinear movement

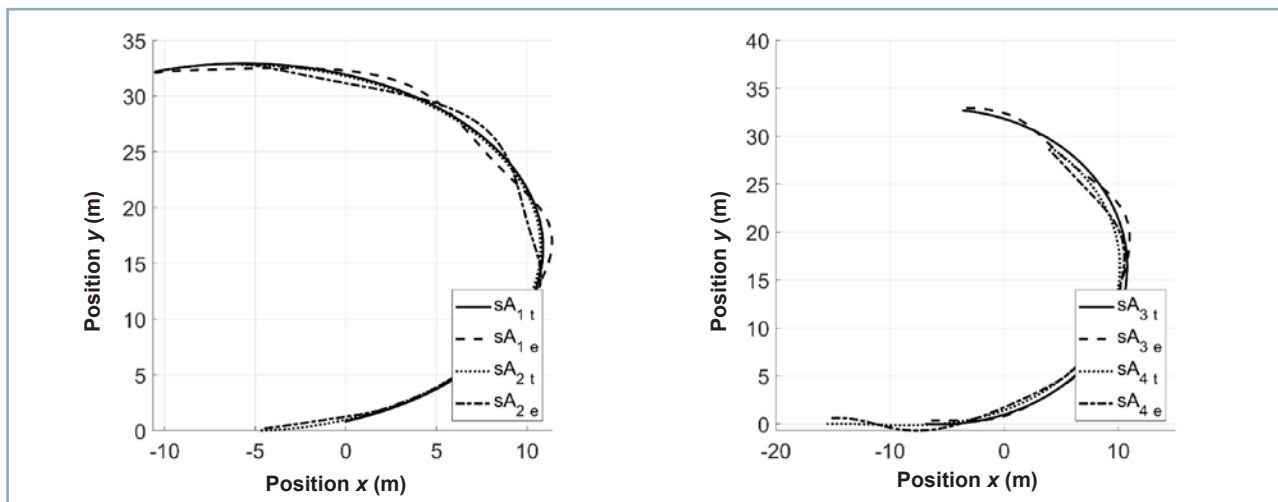


Fig. 6 Comparison of the movement trajectories of aggregate elements HTZ-17021 + APP-6, obtained from theoretical and experimental studies (the trajectories of the first and second tractor half-frames at experimental sA_{1e} , sA_{2e} , sA_{3e} , sA_{4e} ; seed tank and sowing machine at theoretical sA_{1e} , sA_{2e} , sA_{3e} , sA_{4e})

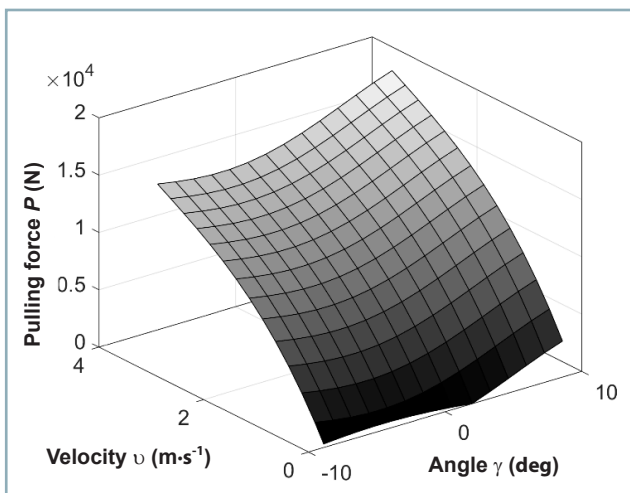


Fig. 7 Draft resistance dependence of the sowing machine APP-6 on the turning angle and its movement speed

By means of the GNU Octave software, draft resistance dependence of the APP-6 sowing machine on the movement speed and the turning angle was determined as follows:

$$P(\gamma, v) = -486.8 + 279.2 \cdot \gamma + 8,100 \cdot v + 46.03 \cdot \gamma^2 - 3.2 \cdot 10^{-14} \cdot \gamma \cdot v - 1,018 \cdot v \quad (\text{N}) \quad (6)$$

where:

- γ – sowing machine turning angle around axis z (°)
- v – sowing machine movement speed (m·s⁻¹)

The determination coefficient for polynomial (Eq. 6) is $R^2 = 0.9532$, which indicates the dependence and its correctness. The sowing machine draft resistance value for its movement speeds from 0 to 3.25 m·s⁻¹, and the turning angle around axis z within the limits $-10^\circ \leq \gamma \leq 10^\circ$ is shown in Fig. 7.

The sensors of the tractor wheel dynamics allow detection of their slipping. For a wheeled tractor, the slip should not exceed 15% if energy-intensive measures were carried out. Let us compare the theoretical v_T and the actual

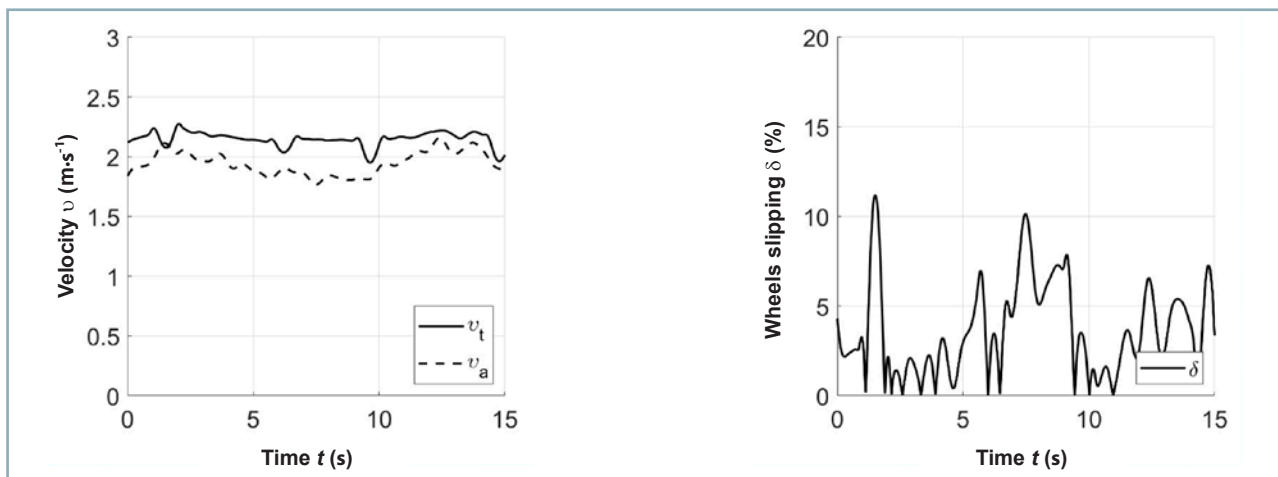


Fig. 8 Dependences of the aggregate actual speed (a) and the slipping of the tractor propulsors (b) on time

speed v_D of the aggregate while sowing the grain crops (Fig. 8a) and calculate the slip of the tractor propulsors δ (Fig. 8b). The average aggregate actual speed value is $\delta_D = 2 \text{ m}\cdot\text{s}^{-1}$. The average slipping value $\delta = 5\%$; the maximum slipping value is $\delta_{\max} = 11.5\%$, which meets the agrotechnical requirements.

On the basis of the obtained dynamic parameters of the HTZ-17021 tractor and the APP-6 sowing machine, it is clear that it works under satisfactory conditions with slipping $\delta = 5\%$; and with its maximum value $\delta_{\max} = 11.5\%$, the turning radius $r_p = 16.25 \text{ m}$ at the end of the pass, which is less than its kinematic length $l_k = 18 \text{ m}$.

The solution of the system of equations, which describes the dynamics of a multi-element MTA, made it possible to obtain dependences of the rotation angles of aggregate elements on time. This solution takes into account the tractor half-frame breakage angle ψ . The turning angles of the aggregate elements presented in Fig. 4 vary in accordance with the harmonic law. The same results were obtained by Fleischmann and Berns (2013).

It should be pointed out that the Lagrange equations were used earlier to study the dynamics of multi-element MTA (Beloiev et al., 2015). Application of this method does not allow investigation of the aggregate dynamics, which may change the scheme of aggregation. When considering changes in the aggregate design, it is necessary to create also the movement equations anew. Proposed method of forming the equations of the dynamics of a multi-element MTA (Eqs. 1–5) allows automatic rearrangement of the movement equations according to the aggregate scheme. There was no such a method for studying the dynamics of multi-unit aggregates before; therefore, the results of this study are important and topical.

Conclusion

In terms of compilation of mathematical models of a plane-parallel movement of MTA in a tractor aggregate with an articulated frame, it is necessary to take into account the pseudo-velocity of the first tractor half-frame as a generalised coordinate. In this case, the dynamic model has one degree of freedom, and the mathematical model consists of one dynamics equation and 29 coordinate equations with dependent variations.

While the MTA is moving across the field, there is a deviation in its elements from the rectilinear path approximated by a sinusoid. Obtained model solution made it possible to establish the relationship of the dynamics and MTA energy. Proposed mathematical model may be used to study the dynamics not only of agricultural multi-element aggregates but also trailers used in the automotive and forestry industries.

Aforementioned method for determining the rotation speed of tractor wheels allows exploration of slip dynamics for each wheel individually at the current time (the instantaneous value). The results of the experimental investigations have proved the efficiency of used measuring system for the purposes of field and laboratory tests of tractors and MTAs.

The average value of slipping of the tractor propulsors $\delta = 5\%$; the maximum value of the slipping $\delta_{\max} = 11.5\%$ does not exceed the maximum value of agrotechnical requirements. At a fixed bending angle of the tractor half-

frames $\psi = 10^\circ$, the aggregate turning radius $r_p = 16.25 \text{ m}$. As a result of the presented research, the discrepancy between the values of the movement trajectories of the tractor, seed tank and sowing machine did not exceed 4%.

Results and discussion

BELOEV, H. – BORISOV, B. – ADAMCHUK, V. – PETRYCHENKO, I. 2015. Theory of movement of the combined seeding unit. In *Agriculture and Agricultural Science Procedia*, vol. 7, pp. 21–26.

BLUNDELL, M. – HARTY, D. 2004. *The Multibody System Approach to Vehicle Dynamics*. Elsevier, 518 pp.

BULGAKOV, V. – ADAMCHUK, V. – GOROBAY, A. – OLT, J. 2016. Theory of the oscillations of a toothed disc opener during its movement across irregularities of the soil surface. In *Agronomy Research*, vol. 14, no. 3, pp. 711–724.

BULGAKOV, V. – KUVACHOV, V. – NOZDROVICKÝ, L. – FINDURA, P. – SMOLINSKYI, S. – IHNATIEV, Y. 2018. The study of movement of the wide span tractor-based field machine unit with power method of its control. In *Acta Technologica Agriculturae*, vol. 21, no. 4, pp. 160–165.

CHIEH, C. 1995. Dynamic modeling of articulated vehicles for automated highway systems. In *Proceedings of the American Control Conference*, Seattle, USA, pp. 653–657.

FRANKE, M. – ZAICZEK, T. – ROBENACK, K. 2012. Simulation of nonholonomic mechanical systems using algorithmic differentiation. In *IFAC Proceedings Volumes*, vol. 45, no. 2, pp. 228–233.

DENHAM, J. – ASMUSSEN, H. – MILLNER, J. – RADNETTER, S. 2007. Networked real-time kinematic corrections for high accuracy machine guidance – dynamic accuracy trials. In *International Global Navigation Satellite Systems Society IGNSS Symposium 2007*. The University of New South Wales, Sydney, Australia.

FLEISCHMANN, T. – BERNS, K. 2013. Trajectory planning and lateral control for agricultural guidance applications. In *8th International Conference on Information Technology and Applications*, pp. 128–133.

IVANOV, S. – BULGAKOV, V. – NADYKTO, V. – KUVACHOV, V. 2018. Theoretical investigation of turning ability of two-machine sowing aggregate. In *Engineering for Rural Development*, vol. 17, pp. 314–322.

KARKEE, M. – STEWARD, B. 2010. Study of the open and closed loop characteristics of a tractor and a single axle towed implement system. In *Journal of Terramechanics*, vol. 47, pp. 379–393.

LILJEDAHL, J. B. – TURNQUIST, P. K. – SMITH, D. W. – HOKI, M. 1996. *Tractors and Their Power Units*. 4th ed., New York, USA, 459 pp. ISBN-13:978-1-4684-6634-8.

SIEW, K. – KATUPITIYA, J. – EATON, R. – POTA, H. 2009. Simulation of an articulated tractor-implement-trailer model under the influence of lateral disturbances. In *IEEE/ASME International Conference on Advanced Intelligent Mechatronics (AIM 2009)*, Singapore, pp. 951–956.

WERNER, R. 2012. Dynamic modeling and path tracking control for a farm tractor towing an implement with steerable wheels and steerable drawbar. In *Commercial Vehicle Technology Symposium*, 13 – 15 March 2012, Kaiserslautern, Germany, pp. 241–250.

YAHYA, A. 2000. Tractor with Built-in DGPS for Mapping Power and Energy Demand of Agricultural Field Operations in Malaysia. In *UPM Research Report 1997–2000*, vol. 2, 131 pp.

YAHYA, A. – ZOHADIE, M. – KHEIRALLA, A. F. – GEW, S. K. – WEE, E. B. 2004. Precision system for mapping terrain trafficability, tractor-implement performance and tillage quality. In *Proceedings of the 7th International Conference on Precision Agriculture and Other Precision Resources Management*. 25 – 28 July 2004, Minneapolis, USA, pp. 23–41.

